TERAHERTZ WAVEGUIDING ON METAMATERIALS

Christopher Rhys Williams

A thesis submitted for the degree of Doctor of Philosophy

University of Bath

Department of Physics

August 2009

Acknowledgements

I would like to begin by sincerely thanking my supervisor Dr. Steve Andrews, not only for his part in giving me the opportunity to undertake this research, but also for providing invaluable help and guidance throughout the completion of this work. In this respect I must also thank Prof. Stefan Maier, both for the initial opportunity and help with numerical finite difference time-domain simulations. I would also like to thank the following people for their contributions. Dr. Mukul Misra fabricated the near-field receivers and helped to complete some of the experimental measurements described in chapter 3 and helped fabricate the coaxial structures described in chapter 5. Dr. Antonio Fernández-Domínguez carried out some of the numerical simulations discussed in chapters 4 and 6, as acknowledged at the appropriate places in the text. Sol Carretero-Palacios contributed the modal expansion results used in chapter 5. Prof. Jonathan Knight provided the hollow-core photonic crystal fibres used in chapter 3. Dr. Byron Alderman oversaw the sputtering and dicing of the coaxial and random structures discussed in chapters 4 and 5. Away from work, I would like to take the opportunity to thank my family and friends, not only for their support, but also for all of the enjoyable times during the period of these studies. Finally, I would like to dedicate this thesis to my parents, without whose love and support this would not have been possible.

Abstract

Terahertz time-domain spectroscopy (TTDS) is a powerful spectroscopic technique, combining pulsed broadband operation with high sensitivity coherent detection at room temperature. This thesis describes studies of terahertz surface plasmon polariton (SPP) guidance on a range of metamaterial structures using TTDS. Metamaterials are artificial media constructed from sub-wavelength dimension conducting elements which have an electromagnetic response that can be engineered by creating geometrical plasma-like resonances. In this work, high-confinement terahertz waveguiding is achieved by binding SPPs to cavity resonances which spoof the behaviour of intrinsic surface plasmon resonances found at much higher frequencies. The main aim of these studies is to investigate their properties with regard to potential applications in waveguiding and sensing. The first two chapters of this thesis describe the background to the subject. In chapter 3, the construction of a novel, flexible geometry, fibre-coupled TTDS system using hollow-core photonic crystal fibre (HC-PCF) is described. The extension of the system to include a near-field probe for evanescent field characterisation is also discussed. In chapter 4, we present the first direct observation of terahertz SPP propagation on plasmonic metamaterials consisting of copper sheets patterned with two-dimensional arrays of square copper-lined holes. Wavelength-scale field confinement is experimentally observed over an octave in frequency close to the band edge, representing a two order of magnitude increase in confinement compared to a flat metal sheet. In chapter 5, metamaterials consisting of two-dimensional arrays of coaxial apertures are shown to support two spoof plasmon modes below the band edge, enabling wavelength-scale field confinement to be experimentally realised at two distinct frequencies. In chapter 6, we present the first experimental results for terahertz SPP propagation on helical and discretely grooved cylindrical metamaterials termed metawires. In each case the results are compared with numerical simulations.

Publications

The work presented in this thesis is included in the following journal publications,

C. R. Williams, S. R. Andrews, S. A. Maier, A. I. Fernández-Domínguez, L. Martín-Moreno and F. J. García-Vidal. *Highly confined guiding of terahertz surface plasmon-polaritons on structured metal surfaces.* Nat. Photonics **2**, 175-179 (2008).

A. I. Fernández-Domínguez, C. R. Williams, F. J. García-Vidal, L. Martín-Moreno, S. R. Andrews and S. A. Maier. *Terahertz surface plasmon polaritons on a helically grooved wire.* Appl. Phys. Lett. **93**, 141109 (2008).

C. R. Williams, M. Misra, S. R. Andrews, S. A. Maier, S. Carretero Palacios, S. G. Rodrigo, F. J. García-Vidal and L. Martín-Moreno. *Dual band terahertz waveguiding on a planar metal surface patterned with annular holes.* Appl. Phys. Lett. Manuscript submitted (2009).

Contents

List of abbreviations

2DEG	Two-dimensional electron gas
AOM	Acousto-optic modulator
CW	Continuous wave
DNA	Deoxyribonucleic acid
EOS	Electrooptic sampling
EOT	Extraordinary transmission
FDTD	Finite-difference time-domain
FIT	Finite-integration technique
FTS	Fourier transform spectroscopy
FWHM	Full-width half-maxima
GVD	Group velocity dispersion
HC-PCF	Hollow-core photonic crystal fibre
HVPR	Horizontal to vertical polarisation ratio
LED	Light emitting diode
LMA-PCF	Large mode area photonic crystal fibre
MEA	Modal expansion approximation
NIM	Negative index material
PCF	Photonic crystal fibre
PEC	Perfect electrical conductor
PPWG	Parallel plate waveguide
RMS	Root-mean-square
SEM	Scanning electron microscope
SMF	Single mode fibre
SPM	Self phase modulation
SPP	Surface plasmon polariton
SRR	Split ring resonator
TE	Transverse electric
TEM	Transverse electromagnetic
TM	Transverse magnetic
TTDS	Terahertz time-domain spectroscopy

UV	Ultraviolet

1. Introduction to the terahertz field

The terahertz region of the electromagnetic spectrum can be defined as occupying the frequency range 0.1-10 THz (λ=3–0.03 mm, $h\upsilon$=0.41-41.4 meV) and is bounded by the microwave and mid-infrared domains. Although often referred to as the 'terahertz gap', in the last twenty years a wide range of sources, detectors and techniques have been developed, several of which can now be used beyond ~50 THz.

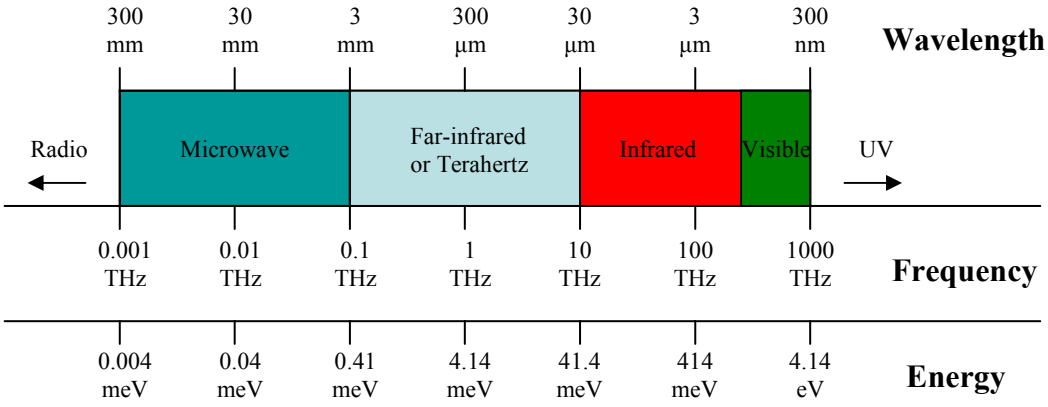

Figure 1.1. Schematic diagram showing the positioning of the terahertz band within the electromagnetic spectrum.

Scientific interest in the band has largely been driven by the existence of elementary excitations, bandgaps and relaxation processes occurring at terahertz frequencies in condensed matter. In addition, a wide range of rotational and low-frequency vibrational modes in gases, liquids and soft matter fall within the terahertz regime. The terahertz part of the spectrum is also important in astronomy [1] and is being increasingly explored for its applications in the pharmaceutical industry [2] and biomedical science [3]. The last decade has also seen the increasing commercialisation of terahertz technology in pharmaceutical quality control and security. In the latter case, its usefulness stems from the fact that materials such as clothing and packaging that are commonly used to conceal

weapons, explosives and illicit drugs are often terahertz transparent, whereas the objects themselves display a very different dielectric response [4].

Terahertz sources and systems generally fall into two categories, narrowband and broadband. A large number of narrowband terahertz sources exist, including optically pumped gas lasers (average powers <150 mW in discrete lines) and backward wave oscillators (<10 mW in the region below 2 THz with limited tunability) both of which are commercially available. Other sources include solid state devices such as Gunn diodes with Schottky-diode multiplier chains (<100 μW above 1 THz with limited tunability) and optical techniques based on photomixing (~1 μW at 1 THz, tunable) or parametric generation (<1 μW power, tunable up to 3 THz) [5]. More recently, terahertz quantum cascade lasers [6] which exploit intersubband transitions in quantum well structures have been demonstrated. These devices are currently limited by their lack of tunability, inability to operate much below 2 THz and low operating temperatures, but can be used to provide >1 mW output power in the region above 2 THz. For applications where spectral resolution is not critical, detection may be achieved using broadband detectors such as helium-cooled bolometers. However, in terahertz applications such as astronomy, that require very high spectral resolution and sensitivity, narrowband heterodyning techniques are more common. In this case, a local oscillator source is mixed with a terahertz signal in a non-linear solid-state device to produce a down-shifted difference frequency component that can be amplified and detected. For example, Schottky-diode detectors and mixer arrays are used in the ThruVision camera system for passive security screening [7].

In spectroscopic applications, Fourier transform spectroscopy (FTS) and Terahertz time-domain spectroscopy (TTDS) are the most widespread techniques, both of which are broadband. In FTS, the far-infrared emission from a mercury arc-lamp, with bandwidth extending from the visible to far-infrared, is typically used to illuminate a sample and transmitted or reflected radiation is analysed interferometrically using an incoherent detector such as a helium-cooled bolometer. In its simplest form FTS records only intensity, although placing the sample in one arm of the interferometer can provide phase information. Despite broad spectral coverage, source powers fall off rapidly at low frequency and the

dynamic range in the terahertz regime is relatively poor. Another problem with FTS is that by working in the frequency domain, spectral artefacts due to reflections can be difficult to remove. Broadband terahertz spectroscopy may also be implemented using free electron lasers in large central facilities. These are widely tuneable and can operate in short-pulse or quasi-CW modes, providing average output powers greater than 10 W.

TTDS offers many advantages over the other terahertz spectroscopic techniques discussed so far, combining pulsed broadband operation with high sensitivity coherent detection at room temperature. Its development in the 1980's led to a renaissance in far-infrared science. In its simplest form, two optical beams derived from the same femtosecond source (pump and probe) are used to excite terahertz emission and time-gate a detector (chapter 3). By varying the time delay between the pump and probe beam, the terahertz electric field can be directly measured (if the system response is known) with sub-ps time resolution. Detection is coherent in that both amplitude and phase information are obtained. TTDS is generally implemented using photoconductive antennas or electro-optic sources and detectors (chapter 3) and average source powers lie in the few μW range. Despite these low powers, very high dynamic range ($>10^{10}$ in power) is possible due to the coherent detection process which is insensitive to thermal background radiation. In terms of power, TTDS is typically over a million times more sensitive than FTS below 3 THz [8]. It is generally implemented in one of three modalities: pump-probe; emission or transmission/reflection. The first two techniques study dynamical processes and are a unique application of TTDS.

In pump-probe studies, a third high intensity optical beam (derived from the same source as the pump and probe) is used to excite carriers in a sample which is probed at subsequent delay using the weak terahertz beam. Following dephasing, the time dependence of the dielectric function can then be measured. This technique has been used to investigate free-carrier dynamics in semiconductors [9], exciton formation and decay in quantum wells [10] and Cooper-pair breaking in high-temperature superconductors [11].

In emission spectroscopy, the terahertz source is replaced by a sample, optically excited by the pump beam. In this case, pump pulses can be used to create a third order nonlinear polarisation between optically excited quantum states and on time scales short compared with dephasing, enable studies of quantum coherence. In semiconductors, charge oscillations in biased coupled quantum wells [12], Bloch oscillations in superlattices [13] and ballistic carrier dynamics [14] have been studied using this technique. Emission spectroscopy has also enabled studies of coherent terahertz emission from phonons [15], plasmons in two-dimensional electron gases (2DEGs) [16] and cyclotron motion [17]. More recently, terahertz emission microscopy has been developed as a tool for imaging electric fields [18].

In transmission/reflection studies, a sample is placed in the terahertz beam and the frequency-dependent complex dielectric function is derived directly from the measured amplitude reflection or transmission coefficients. This technique has been used extensively to characterise a wide range of materials including semiconductors, superconductors, liquids, gases and dielectrics [19]. Some applications are also of interest outside of the laboratory. For example, in the identification of concealed explosives [20], differentiation of polymorphism and crystallinity in pharmaceutics [21] and label-free identification of the hybridisation state of DNA [22,23]. Although this form of TTDS provides no dynamical information and similar experiments can be performed using dispersive FTS, the dynamic range is far higher and artefacts associated with reflections can be straightforwardly eliminated. The insensitivity of TTDS to thermal background radiation also has a unique advantage in the investigation of high-temperature plasmas such as flames [24].

Transmission/reflection studies can also be used to perform terahertz imaging. Unlike CW imaging techniques, the pulsed nature of TTDS facilitates the extraction of depth information [25] and the short coherence length leads to improved image quality compared to narrowband techniques [26]. Amongst the most important demonstrations to date, TTDS imaging has been shown to be potentially useful in defining skin cancer tumour margins [27], probing uniformity in pharmaceutical products [28] and identifying defects in space shuttle insulation [29]. TTDS imaging can also be used to image the slow evolution of physical

processes with time, such as the diffusion of gases [30]. In all of the imaging applications discussed so far, the spatial resolution is limited by diffraction. Imaging in the near-field, before radiation diffracts, enables sub-wavelength resolution to be attained. To date, a range of TTDS near-field techniques have been explored (chapter 3) and used to investigate phenomena such as the time-resolved transmission of terahertz radiation through metallic sub-wavelength hole arrays [31] and mapping of electromagnetic resonances in metamaterials with resolution down to ~$\lambda/40$ [32].

This thesis describes studies of terahertz surface plasmon polariton (SPP) guidance on a range of metamaterial structures using TTDS. In chapter 2, an introduction to the field of metamaterials and plasmonics is presented. In chapter 3, the construction of a novel fibre-coupled TTDS system is described. The extension of our system to incorporate a near-field probing arm is also described. In chapter 4, we present the first direct observations of terahertz SPPs on metamaterials consisting of 'blind' two-dimensional air-filled hole arrays. This is followed in chapter 5 by the realisation of dual-frequency confinement using an alternative planar metamaterial structure consisting of coaxial hole arrays and finally in chapter 6 by the first experimental investigations of SPP guidance on helically and discretely grooved cylindrical metamaterials, termed metawires.

References

[1] P. H. Siegel. *THz instruments for space.* IEEE Trans. Antennas Propag. **55**(11), 2957-2965 (2007).

[2] J. A. Zeitler, P. F. Taday, D. A. Newnham, M. Pepper, K. C. Gordon and T. Rades. *Terahertz pulsed spectroscopy and imaging in the pharmaceutical setting – a review.* J. Pharm. Pharmacol. **59**, 209-223 (2007).

[3] E. Pickwell and V. P. Wallace. *Biomedical applications of terahertz technology*. J. Phys. D: Appl. Phys. **39**, R301-R310 (2006).

[4] J. F. Federici, B. Schulkin, F. Huang, D. Gary, R. Barat, F. Oliveira and D. Zimdars. *THz imaging and sensing for security applications – explosives, weapons and drugs.* Semicond. Sci. Technol. **20**, S266-S280 (2005).

[5] A. Dobroiu, C. Otani and K. Kawase. *Terahertz-wave sources and imaging applications.* Meas. Sci. Technol. **17**, R161-R174 (2006).

[6] B. S. Williams. *Terahertz quantum-cascade lasers.* Nat. Photonics **1**, 517-525 (2007).

[7] http://thruvision.com. T4000.

[8] P. Y. Han, M. Tani, M. Usami, S. Kono, R. Kersting and X-C. Zhang. *A direct comparison between terahertz time-domain spectroscopy and far-infrared Fourier transform spectroscopy.* J. Appl. Phys. **89**(4), 2357-2359 (2001).

[9] M. C. Beard, G. M. Turner and C. A. Schmuttenmaer. *Transient photoconductivity in GaAs as measured by time-resolved terahertz spectroscopy.* Phys. Rev. B **62**(23), 15764-15777 (2000).

[10] R. A. Kaindl, M. A. Carnahan, D. Hägele, R. Lövenich and D. S. Chemla. *Ultrafast terahertz probes of transient conducting and insulating phases in an electron-hole gas.* Nature **423**, 734-738 (2003).

[11] R. D. Averitt, G. Rodriguez, J. L. W. Siders, S. A. Trugman and A. J. Taylor. *Conductivity artifacts in optical-pump THz-probe measurements of* $YBa_2Cu_3O_7$. J. Opt. Soc. Am. B **17**(2), 327-331 (2000).

[12] H. G. Roskos, M. C. Nuss, J. Shah, K. Leo, D. A. B. Miller, A. M. Fox, S. Schmitt-Rink and K. Köhler. *Coherent submillimeter-wave emission from charge oscillations in a double-well potential.* Phys. Rev. Lett. **68**(14), 2216-2220 (1992).

[13] C. Waschke, H. G. Roskos, R. Schwedler, K. Leo, H. Kurz and K. Köhler. *Coherent submillimeter-wave emission from Bloch oscillations in a semiconductor superlattice.* Phys. Rev. Lett. **70**(21), 3319-3322 (1993).

[14] B. B. Hu, E. A. de Souza, W. H. Knox, J. E. Cunningham, M. C. Nuss, A. V. Kuznetsov and S. L. Chuang. *Identifying the distinct phases of carrier transport in semiconductors with 10 fs resolution.* Phys. Rev. Lett. **74**(9), 1689-1692 (1995).

[15] T. Dekorsy, H. Auer, C. Waschke, H. J. Bakker, H. G. Roskos, H. Kurz, V. Wagner and P. Grosse. *Emission of submillimeter electromagnetic waves by coherent phonons.* Phys. Rev. Lett. **74**(5), 738-741 (1995).

[16] A. Armitage, S. R. Andrews, J. A. Cluff, P. G. Huggard, E. H. Linfield and D. A. Ritchie. *Ultrafast optical excitation of coherent two-dimensional plasmons.* Phys. Rev. B **69**, 125309 (2004).

[17] D. Some and A. V. Nurmikko. *Coherent transient cyclotron emission from photoexcited GaAs.* Phys. Rev. B **50**(8), 5783-5786 (1994).

[18] H. Murakami and M. Tonouchi. *Laser terahertz emission microscopy.* C. R. Physique **9**, 169-183 (2008).

[19] D. Grischkowsky, S. Keiding, M. van Exter and Ch. Fattinger. *Far-infrared time-domain spectroscopy with terahertz beams of dielectrics and semiconductors.* J. Opt Soc. Am. B **7**(10), 2006-2015 (1990).

[20] K. Yamamoto, M. Yamaguchi, F. Miyamaru, M. Tani, M. Hangyo, T. Ikeda, A. Matsushita, K. Koide, M. Tatsuno and Y. Minami. *Noninvasive inspection of C-4 explosives in mails by terahertz time-domain spectroscopy.* Jpn. J. Appl. Phys. **43**(3B), L414-L417 (2004).

[21] C. J. Strachan, P. F. Taday, D. A. Newnham, K. C. Gordon, J. A. Zeitler, M. Pepper and T. Rades. *Using terahertz pulsed spectroscopy to quantify pharmaceutical polymorphism and crystallinity.* J. Pharm. Sci. **94**(4), 837-846 (2005).

[22] M. Brucherseifer, M. Nagel, P. Haring Bolivar, H. Kurz, A. Bosserhoff and R. Büttner. *Label-free probing of the binding state of DNA by time-domain terahertz sensing.* Appl. Phys. Lett. **77**(24), 4049-4051 (2000).

[23] M. Nagel, P. Haring Bolivar, M. Brucherseifer, H. Kurz, A. Bosserhoff and R. Buttner. *Integrated THz technology for label-free genetic diagnostics*. Appl. Phys. Lett. **80**(1), 154-156 (2002).

[24] R. A. Cheville and D. Grischkowsky. *Far-infrared time-domain spectroscopy of flames.* Opt. Lett. **20**(15), 1646-1648 (1995).

[25] D. M. Mittleman, S. Hunsche, L. Boivin and M. C. Nuss. *T-ray tomography.* Opt. Lett. **22**, 904-906 (1997).

[26] W. L. Chan, J. Deibel and D. M. Mittleman. *Imaging with terahertz radiation.* Rep. Prog. Phys. **70**, 1325-1379 (2007).

[27] V. P. Wallace, A. J. Fitzgerald, S. Shankar, N. Flanagan, R. J. Pye, J. Cluff and D. D. Arnone. *Terahertz pulsed imaging of basal cell carcinoma ex vivo and in vivo.* Br. J. Dermatol. **151**, 424-432 (2004).

[28] J. A. Zeitler, Y. Shen, C. Baker, P. F. Taday, M. Pepper and T. Rades. *Analysis of coating structures and interfaces in solid oral dosage forms by three dimensional terahertz pulsed imaging.* J. Pharm. Sci. **96**(2), 330-340 (2006).

[29] H. Zhong, J. Xu, X. Xie, T. Yuan, R. Reightler, E. Madaras and X-C. Zhang. *Nondestructive defect identification with terahertz time-of-flight tomography.* IEEE Sens. J. **5**(2), 203-208 (2005).

[30] P. C. M. Planken and H. J. Bakker. *Towards time-resolved THz imaging.* Appl. Phys. A **78**, 465-469 (2004).

[31] A. Bitzer and M. Walther. *Terahertz near-field imaging of metallic subwavelength holes and hole arrays.* Appl. Phys. Lett. **92**, 231101 (2008).

[32] A. Bitzer, H. Merbold, A. Thoman, T. Feurer, H. Helm and M. Walther. *Terahertz near-field imaging of a planar metamaterial.* Opt. Express **17**(5), 3826-3834 (2009).

2. Metamaterials Introduction

2.1. Metamaterials and negative refractive index

Metamaterials are artificial media constructed from sub-wavelength dimension conducting elements embedded in a dielectric. They enable the engineering of electric and magnetic resonant responses that do not occur in nature. The wavelength of light normally sets a fundamental limit on the minimum resolvable feature size in any system, so that metamaterials may be described electromagnetically as homogenous media characterised by an effective refractive index $n_{eff,}$ or equivalently, by an effective dielectric function ε_{eff} and permeability $\mu_{eff.}$ The idea of replacing a material that is inhomogeneous on a sub-wavelength scale by a homogeneous effective medium is integral to the metamaterial concept. The ability to use metamaterials to create artificial electromagnetic responses has led to growing research interest and a range of potential applications. Examples include engineering confined surface modes in the terahertz and microwave domains that mimic the behaviour of surface plasmons in the visible for sensing and waveguiding applications, as well as engineering metamaterials with negative refractive index to investigate exotic electromagnetic phenomena such as perfect lensing and cloaking.

The electromagnetic response of metamaterials is principally controlled by creating geometrical plasma-type resonances, which neglecting losses, take the form,

$$\varepsilon_{\text{eff}} = 1 - \frac{\omega_{\text{p}}^2}{\omega^2} \tag{2.1}$$

$$\mu_{\text{eff}} \approx 1 - \frac{\omega_{\text{m}}^2}{\omega^2} \tag{2.2}$$

where ω_p and ω_m are the effective electrical and magnetic plasma frequencies. For example, low frequency electrical resonances can be engineered using thin wire arrays [1] and magnetic responses can be set up using discontinuous current loops

termed split ring resonators (SRRs) [2]. In the magnetic case, $\mu_{eff}<0$ generally resides within a bandgap, but metamaterials displaying a negative refractive index over narrow frequency bands can be constructed by combining electric and magnetic resonant elements [3]. In this case the presence of the electrical resonance leads to the formation of a passband in the SRR bandgap where ε_{eff} and μ_{eff} are simultaneously negative.

For transverse electromagnetic wave propagation through a medium with $\varepsilon_{eff}>0$ and $\mu_{eff}>0$, the vectors $\underline{E}$, $\underline{H}$ and $\underline{k}$ form a right-handed set. In this case the phase and group velocities are parallel and the refractive index is positive. However, if the medium has $\varepsilon_{eff}<0$ and $\mu_{eff}<0$, $\underline{E}$, $\underline{H}$ and $\underline{k}$ form a left-handed set and the wavevector $\underline{k}$, which is always in the direction of the phase velocity, is anti-parallel to the energy flux. In this scenario the negative root of the refractive index, $n_{eff} = \sqrt{\varepsilon_{eff}\,\mu_{eff}}$, must be chosen [4]. For this reason, such left-handed materials have become known as negative index materials (NIMs). Electromagnetic propagation in NIMs leads to a range of intriguing effects, such as a negative Doppler shift, reversed Cherenkov effect and negative refraction of light. From Snell's law it is evident that when light passes from one right-handed medium to another, the wave fronts are always refracted to the opposite side of the surface normal at each interface. However, when light propagates across an interface where the refractive index changes sign, the wave is refracted back to the same side of the surface normal, as confirmed experimentally by Shelby et al. [5]. This point is illustrated in figure 2.1.

As a result, a point source is imaged by a NIM slab (figure 2.1). This effect was further analysed by Pendry [6] who predicted that it was also possible to recreate the sources non-propagating fields at the image. In this case, the decaying evanescent fields are amplified by surface plasmons. The diffraction limit on the imaging of objects arises from the lack of these fields in a normal image. Collecting these components allows the limit to be beaten, creating a 'perfect lens'. A variation on the perfect lens concept is the so-called 'poor man's lens' where only ε_{eff} is negative. This works provided that all dimensions are much less than the wavelength of light so that the electrostatic and magnetostatic fields

decouple. In this case, for focussing of transverse magnetic (TM) waves the dependence on the magnetic permittivity is removed. This approach was used by Fang et al. [7] to demonstrate sub-diffraction limit (~λ/6) imaging through a thin silver slab.

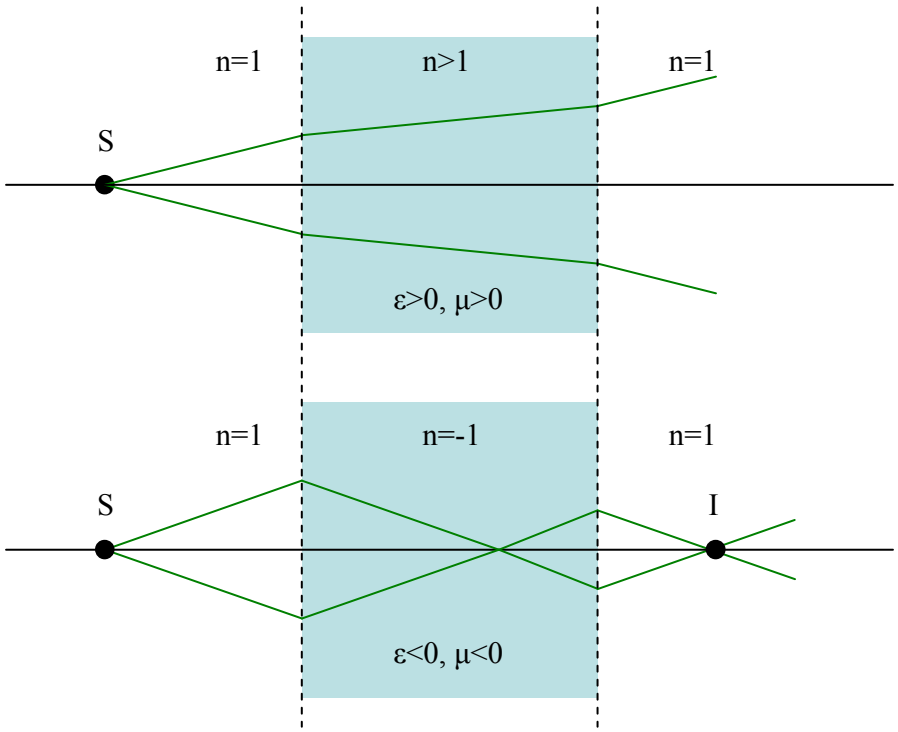

Figure 2.1. Schematic diagram showing normal (top) and anomalous (bottom) ray refraction. S is a point source and I is the focussed image.

Another intriguing potential use of metamaterials is electromagnetic cloaking [8], which relies on the scale invariance of Maxwell's equations. This indicates that if space is stretched so as to guide light around an object, Maxwell's equations need only be reformulated in terms of a transformed coordinate system with ε_{eff} and μ_{eff} scaled by an appropriate factor. In this case, significant dispersion is required to satisfy causality. This is because in order to curve around an object and return to its original path undisturbed, light must exhibit a phase velocity exceeding the velocity of light. Metamaterial cloaking was first demonstrated by Schurig et al. in 2006 [9]. In this experiment, a copper cylinder surrounded by layers of SRRs was effectively cloaked at 8.5 GHz.

Metamaterials can also be created with electrically or optically controllable responses for potential applications in switching. In 2008, Chen et al. [10] demonstrated the ability to tune the electrical resonant frequency of a silicon/metal SRR array by ~20%. In this case optically generated photocarriers were used to modulate the gap capacitance in a silicon-metal hybrid SRR. Significant transmission modulation through SRR arrays has also been demonstrated using optical and electrical gating of the gap capacitance [11,12] and more recently terahertz phase modulation has been demonstrated using biased SRRs [13]

Although much metamaterial work to date has been conducted at microwave and terahertz frequencies, there have also been many studies within the infrared and visible bands. Notable examples include the production of magnetic resonances in the mid- [14] and near-infrared [15] as well as the demonstration of a negative refractive index in the visible [16].

2.2. Plasmonic metamaterials, enhanced transmission and waveguiding

Work on the plasmonic properties of metamaterials was largely stimulated by the discovery of extraordinary optical transmission (EOT) through arrays of sub-wavelength holes in metal sheets by Ebbesen et al. in 1998 [17]. In this study, the transmission of visible light was found to show resonant maxima exceeding Bethe's theory by several orders of magnitude. In 2001, Martin-Moreno et al. [18] argued that the transmission process was driven via diffractively induced electromagnetic coupling between the incident light and surface plasmons interacting on the two faces of the array. In this process, light can be funnelled through the holes in the form of hybridised TM surface waves called surface plasmon polaritons (SPPs) before being re-radiated back into free-space. The effective area of the holes is therefore much larger than the geometrical area. Since Ebbesen's study in the visible, enhanced transmission has also been realised at frequencies far below the intrinsic plasma frequency, where metals behave like

perfect conductors [19,20]. In this case, rather than involving surface plasmons, the resonantly enhanced transmission process is mediated by geometrically controlled cavity resonances called spoof plasmons [21,22], which mimic the properties of the intrinsic surface plasmon resonances found at much higher frequencies. Therefore, in direct contrast with the visible domain, at low frequencies the hole shape (which influences the hole resonance) plays a crucial role in determining the transmission properties [20].

A new area in terahertz metamaterial research seeks to exploit spoof plasmons for high-confinement waveguiding and potential applications in sensing. The ideal terahertz waveguide is dispersionless so that short pulses can be guided without distortion, offers high confinement and low loss and can be efficiently coupled to sources and detectors. In reality all waveguides suffer a trade-off between these various properties. Terahertz waveguides studied to date can be grouped into dielectric- and metal-based categories.

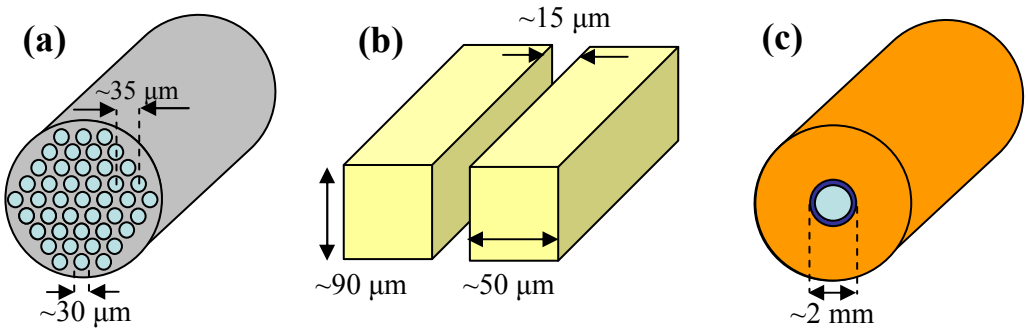

Figure 2.2. Schematic diagram of various waveguide geometries discussed in the text. (a) porous fibre proposed by Hassani et al. consisting of a hexagonal array of holes (light blue) in a sub-wavelength polymer fibre (grey) (b) dielectric slab guide discussed by Walther et al. consisting of two silicon slabs separated by a small air gap. (c) Polymer coated capillary guide discussed by Bowden et al. consisting of a silver coated air-filled (light blue) glass capillary (orange). A thin polystyrene layer (dark blue) coats the silver to reduce loss.

The main growth area in dielectric-based waveguiding is photonic crystal fibre development. To date, losses as low as ~0.002 cm^{-1} have been measured for narrow frequency bands (~0.1 THz) in Bragg guiding structures [23] although the presence of cladding resonances cause the loss to increase dramatically outside of

these narrow guidance bandwidths, resulting in energy leakage from the core. Another promising fibre architecture is a core-less design proposed by Hassani et al. [24], consisting of an array of sub-wavelength air holes embedded in a sub-wavelength polymer fibre (figure 2.2(a)). For large air-filling fractions, the majority of energy can be guided within air, minimising both loss and dispersion. Unfortunately, in this case the mode localisation decreases and bend-loss becomes a significant factor. For this structure it is predicted that careful tuning of the air-filling fraction could enable relatively broadband (~1 THz) waveguiding with losses below ~0.01 cm^{-1}. Terahertz radiation may also be guided between two dielectric slabs separated by a small air gap (figure 2.2(b)). Simulations predict that well-confined low-loss propagation (<0.001 cm^{-1}) can be achieved in such structures [25], although propagation is accompanied by non-negligible dispersion.

Waveguiding approaches using metals offer the advantage that intrinsic material losses can be negligible. Most successful metallic guides concentrate the majority of terahertz energy in air to minimise attenuation and reduce dispersion. Polystyrene coated metal capillaries (figure 2.2(c)) have been demonstrated to provide single frequency propagation losses as low as ~0.001 cm^{-1} at 2.5 THz [26] and broadband (0.1-3 THz), low-loss (<0.15 cm^{-1}) terahertz waveguiding has been demonstrated using parallel plate waveguides (PPWGs) [27]. In 2007, Wächter et al. [28] showed that reduction of the lateral dimension of the PPWG, in so-called 'over-sized' waveguides, can improve transverse confinement. In this case losses <0.05 cm^{-1} were demonstrated up to 1 THz with negligible dispersion.

Metal wires and sheets offer another terahertz waveguiding solution [29,30]. In both of these cases, terahertz radiation is coupled to the conduction electrons at the metal-air interface to form SPPs. The demonstrated losses (~0.023 cm^{-1} for wires and ~0.01 cm^{-1} for sheets) are low and dispersion is negligible. Unfortunately, the poor localisation of the modal fields (which extend many tens to hundreds of wavelengths into the bounding dielectric) increase the probability of modal decoupling via bend loss, scattering and interactions with nearby objects. Plasmonic metamaterials offer a route towards significantly improving this confinement [21,22], allowing strong field confinement to be translated into

the terahertz region via the excitation of spoof plasmons. In this case, the effective plasma frequency is controlled entirely by the geometry of the surface, rather than the properties of the metal.

2.3. Surface plasmon polaritons and spoof plasmons

2.3.1. Surface plasmon polaritons (SPPs)

Coupling between light and the collective oscillations of an electron plasma at any interface across which the real part of the dielectric constant changes sign, such as a metal–dielectric interface, can give rise to SPPs, provided that the condition $\varepsilon_m(\omega) \leq -\varepsilon_d$ is also satisfied (where $\varepsilon_m(\omega)$ is the metallic dielectric function and ε_d is the relative permittivity of the dielectric). These TM surface waves exhibit evanescent decay on either side of the supporting interface and are momentum mismatched with respect to light in free-space ($k_x > k_0$, see equation 2.3). Excitation therefore requires a scheme for phase matching. In practice, at terahertz frequencies, broadband coupling using p-polarised incident radiation can be achieved either via diffraction from a wavelength-scale aperture (chapter 4), or by end-fire coupling (chapters 5 and 6), where efficient SPP excitation occurs by maximising the spatial overlap between the incident electric field and the SPP.

Following excitation, the evolving SPP must propagate a finite distance before reaching its stable form. This is due to there being an effective interaction length over which free-space radiation and the SPP can exchange energy. In this physical picture, the wavevector mismatch $\Delta k = k_x - k_0$, satisfies the relation, $\Delta k < \pi / L_{int}$, where L_{int} defines the effective interaction length. For the metamaterials discussed in this thesis, L_{int} is typically a few mm or less near the band edge, but for planar metal sheets, L_{int} can be many tens of centimetres. In terms of experimental measurements, it is therefore essential that in order to measure the properties of the SPP accurately the sample length must be much larger than this interaction length.

For SPP propagation along an optically thick flat metal sheet of infinite lateral extent bounded by a dielectric, the SPP wavevector in the propagation direction, k_x, can be derived by looking for an evanescent solution of the wave equation [31] and is given by,

$$k_x = k_0 \sqrt{\frac{\varepsilon_m(\omega)\varepsilon_d}{\varepsilon_m(\omega)+\varepsilon_d}} \tag{2.3}$$

where $k_0=\omega/c$ is the free-space wavevector and the remaining term represents the effective refractive index of the mode. In order to evaluate equation 2.3 a Drude model can be used for $\varepsilon_m(\omega)$,

$$\varepsilon_m(\omega) = 1 - \frac{\omega_p^{\,2}}{\omega^2 + i\omega\omega_\tau} \tag{2.4}$$

where ω_p is the intrinsic bulk plasma frequency and ω_τ is the electron scattering frequency. This expression is valid at low frequencies, but above the phonon frequencies of the material (typically >5 THz), the residual polarisation of the lattice should be taken into account. In this case, the preceding 1 in equation (2.4) must be replaced by the lattice dielectric constant ε_∞, which generally takes a value of $1 \le \varepsilon_\infty \le 10$. In this work, a value of $\varepsilon_\infty=1$ is assumed throughout.

For most metals, ω_p lies in the UV and can be calculated using,

$$\omega_p = \sqrt{\frac{ne^2}{\varepsilon_0 m^*}} \tag{2.5}$$

where n is the free-electron density (~10^{23} cm^{-3} for a typical metal) and m^* is the effective electron mass (~1.5 m_e for copper [32]).

The Drude model can also be recast in terms of the electrical conductivity $\sigma(\omega)$,

$$\varepsilon_m(\omega) = 1 + \frac{i\sigma(\omega)}{\varepsilon_0 \omega} = 1 + \frac{i\sigma_0}{\varepsilon_0 \omega(1 - i\omega/\omega_\tau)} \tag{2.6}$$

where σ_0 is the dc conductivity.

At high frequencies (f>480 THz for copper [32]), the accuracy of the Drude model breaks down due to the onset of interband transitions. Despite this it can still be used to provide qualitative information about the properties of SPPs. Figure 2.3 shows the dispersion relation for SPP propagation on copper, calculated using the Drude parameters given in the figure caption. At high frequencies, the SPP dispersion curve diverges significantly from the light line. For a lossless metal it plateaus at the surface plasma frequency, $\omega_{sp} = \omega_p / \sqrt{1 + \varepsilon_d}$. In this region, the group velocity tends to zero and the SPP binds tightly to the supporting interface (f_{sp}~ 1200 THz for copper).

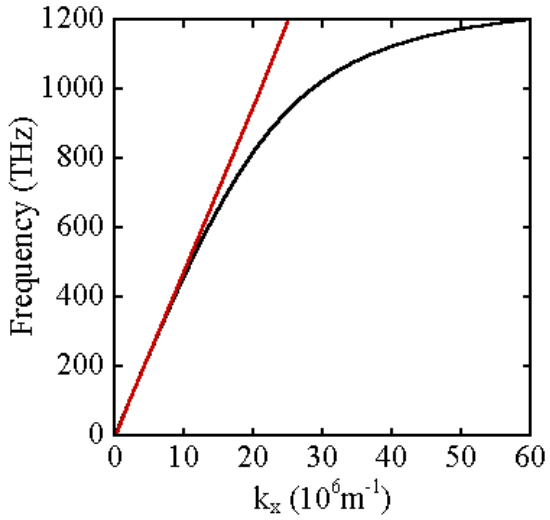

Figure 2.3. Dispersion curve for planar SPP propagation on copper (black curve) calculated using a Drude model with ω_τ = 1.38.10^{13} rad.s^{-1} and ω_p= 1.12.10^{16} rad.s^{-1} [33]. The light line is plotted in red.

The longer wavelength of the SPP with respect to light in free-space leads to the evanescent character of the SPP. In this case, conservation of momentum dictates

that the total wavevector in the dielectric region, $k_{0,}$ must be related to the in-plane (k_x) and out-of-plane (k_{zd}) SPP wavevector components by,

$$k_{zd} = \sqrt{\varepsilon_d k_0^{\,2} - k_x^{\,2}} \tag{2.7}$$

Hence, if $k_x > \sqrt{\varepsilon_d}\, k_{0,}$ k_{zd} must be purely imaginary, resulting in out-of-plane decay. Such evanescent fields cannot propagate away from the surface so that the energy of the SPP is localised there.

The frequency dependent confinement of the SPP on the dielectric side of the supporting interface is described by the 1/e field decay length,

$$L_{zd} = \frac{1}{\mathrm{Im}(k_{zd})} \tag{2.8}$$

The decay length into the metal (L_{zm}) can also be evaluated from equation 2.8 by replacing ε_d in equation 2.7 by $\varepsilon_m(\omega)$. Within the terahertz regime the SPP decay length into the metal is commonly approximated using the skin depth δ_m, which in terms of amplitude decay is given by,

$$\delta_m = \sqrt{\frac{2}{\sigma_0 \mu_0 \omega}} \tag{2.9}$$

This expression can be derived from equations 2.3 and 2.7 (formulated in terms of $\varepsilon_m(\omega)$) by assuming that the imaginary part of the metals dielectric function is much larger than the real part and using the substitution $Im(\varepsilon_m) \sim \sigma_0 / \omega\varepsilon_0$, which is valid provided that $\omega/\omega_\tau << 1$.

Figure 2.4 shows a plot of the SPP penetration depth evaluated from the SPP model and equation 2.9. It is clear that the skin depth formula gives a reasonable approximation of the SPP penetration depth over the frequency range 1-5 THz but breaks down outside of this range due to the break down of the assumptions

involved in deriving equation 2.9. Another reason for the disagreement is the unphysical value for the dc conductivity (σ_0=8.1.10^7 Ω^{-1}m^{-1}) implicit in the Drude parameters given by Ordal et al. [33].

Quantifying the SPP penetration depth into the metal is important, as it determines the Ohmic loss. Also, for free-standing metal sheets, in which two metal-dielectric surfaces are exposed, SPPs can be supported at each surface. In this case, for optically thick metal sheets (more than a couple of skin depths thick) there is no coupling between the modes and both SPPs may be independently described using equation 2.3. However, for the case of optically thin sheets, SPP fields extend through the metal. In this case degeneracy of the modes is lifted and the dispersion curve splits into two distinct branches, corresponding to a high frequency anti-symmetric mode and low frequency symmetric mode. In all of the work discussed in this thesis the metals are optically thick.

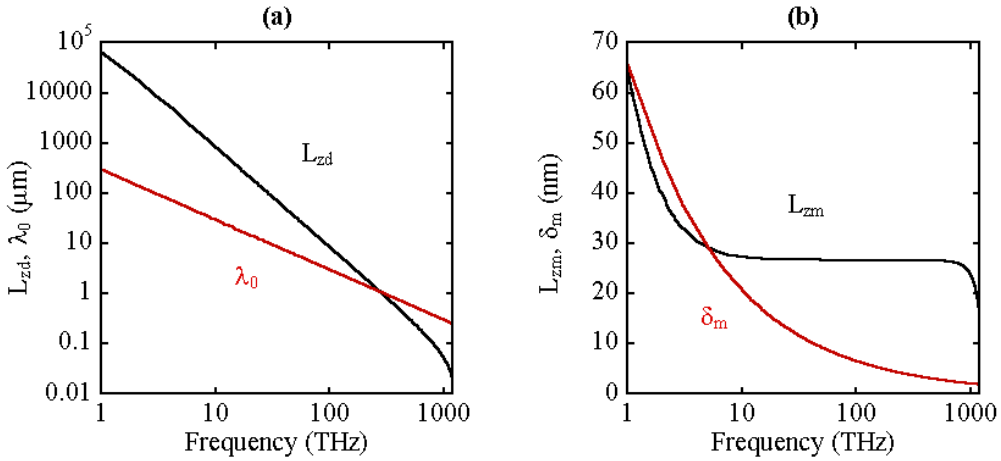

Figure 2.4. (a) Out-of-plane decay length into air (L_{zd}) for planar SPP propagation on copper (black curve) calculated using a Drude model with parameters ω_τ = 1.38.10^{13} rad.s^{-1}, ε_∞=1 and ω_p= 1.12.10^{16} rad.s^{-1} [33]. The free-space wavelength λ_0 is also plotted for comparison (red curve). (b) Out-of-plane SPP decay length into copper (L_{zm}) calculated using identical Drude parameters and skin depth (δ_m) evaluated from equation 2.9 with dc conductivity σ_0=5.8.10^7 $\Omega^{-1}m^{-1}$.

The frequency dependent attenuation length of the mode along the propagation axis, parallel to the surface, can be evaluated using,

$$L_x = \frac{1}{\mathrm{Im}(k_x)} \tag{2.10}$$

It is clear from figure 2.5 that at high frequencies, close to the surface plasma frequency, the propagation length is significantly reduced as the mode is increasingly bound to the supporting interface. In contrast, a value of L_x~ 139 m is obtained at 1 THz, where the mode is poorly confined and able to propagate vast distances. In reality, slight imperfections or curvature of the surface drastically reduce this value.

At optical frequencies, close to the surface plasma frequency, the ability to guide and confine SPPs on sub-wavelength dimensions (figure 2.4) leads to a wide-range of applications in fields such as optical circuit miniaturisation, near-field imaging, nonlinear spectroscopy and sensing [34,35]. There are also potential medical applications. For example, resonant excitation of plasmonic modes in nanoshells injected into the blood stream of mice has been used to locally destroy cancerous tissue [36].

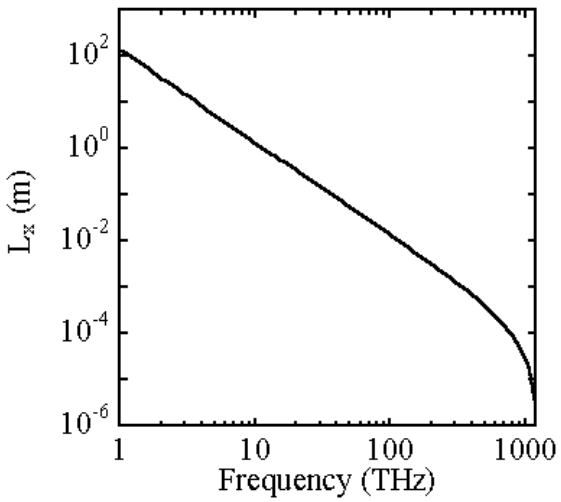

Figure 2.5. Propagation decay length (L_x) for planar SPP propagation on copper, calculated using a Drude model with parameters $\omega_\tau = 1.38.10^{13}$ rad.s^{-1}, $\varepsilon_\infty=1$ and $\omega_p= 1.12.10^{16}$ rad.s^{-1} [33].

At lower frequencies, in the far infrared and microwave regions, metals also support electromagnetic surface waves, but here the out-of-plane fields are only weakly confined, extending hundreds of wavelengths into the bounding dielectric (figure 2.4). Such extended surface modes, known as Sommerfeld or Zenneck waves, for planar and cylindrical surfaces respectively, were first described mathematically at the turn of the twentieth century. The strong frequency dependence of the SPP field confinement is directly linked to the many orders of magnitude variation in the metallic dielectric function, as illustrated in figure 2.6.

In the visible regime (f~ 1000 THz), ε_m is comparable in magnitude with the dielectric constant of the bounding dielectric ε_d, resulting in reasonable impedance matching across the interface and strong coupling between the light field and the surface plasma (tightly confined SPPs). However, in the terahertz regime $|\varepsilon_m| >> \varepsilon_d$ and the impedance mismatch becomes large, resulting in poor coupling and hence weakly confined SPPs. In the perfect conductor limit, the impedance mismatch across the interface becomes infinite and no SPPs can be supported.

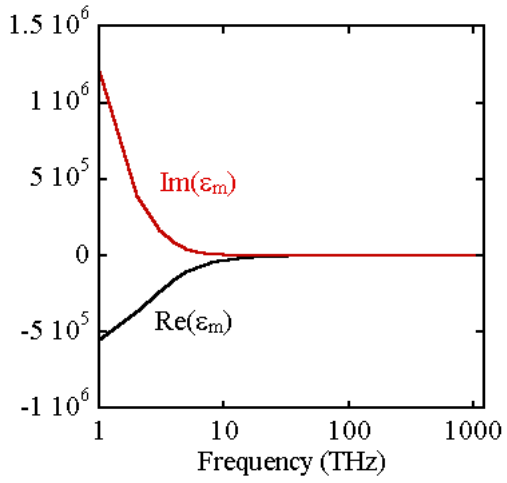

Figure 2.6. Real and imaginary parts of the frequency-dependent dielectric function of copper calculated using a Drude model with parameters $\omega_\tau = 1.38.10^{13}$ *rad.s*$^{-1}$ *and* $\omega_p = 1.12.10^{16}$ *rad.s*$^{-1}$ *[33].*

2.3.2. Spoof plasmons

One way of increasing surface wave confinement at low frequency involves texturing the surface of the metal to form a metamaterial. This was discussed theoretically by Goubau [37] and Mills and Maradudin [38] many years ago. Physically, the increased binding arises because the presence of the indentations leads to greater penetration of the field into the material in an effective medium picture. It has long been known that very thin wire meshes (~λ/50), can support confined surface modes at low frequencies [39]. More recently, this concept was extended by Pendry et al. [21,22] with the introduction of the idea of plasmonic metamaterials consisting of metal surfaces textured with sub-wavelength scale corrugations or holes. In the latter works, such surfaces were shown to support confined SPP-like modes with dispersion controlled only by geometry. Even perfect conductors which cannot support surface plasmons can support these 'spoof' plasmons. The existence of such spoof plasmons was indirectly verified soon afterwards through the use of microwave reflectivity measurements on two-dimensional brass rod arrays [40].

Alternative approaches for increasing SPP confinement in the terahertz regime have also been proposed. For example, semiconductors can be doped to obtain plasma frequencies in the terahertz range [41,42], and high-index dielectric over-layers can be deposited onto flat metallic films to increase confinement [43]. Neither of these approaches offer as much flexibility for engineering all aspects of the SPP dispersion as the metamaterial case. Another disadvantage of the doped-semiconductor approach is that structures are generally restricted to planar geometries due to the reliance on single-crystalline materials, whereas the main disadvantage of dielectric-overlayering is that the field is only tightly confined within the overlayer itself. This last point limits access to the guided mode and restricts the use of the bound fields for sensing purposes. Metamaterials solve this problem by confining the field within air.

The majority of the work in this thesis deals with spoof-plasmon mediated propagation of terahertz SPPs on metamaterials. These studies have been

conducted with the aim of investigating their properties with regard to potential applications in waveguiding and sensing.

References

[1] J. B. Pendry, A. J. Holden, W. J. Stewart and I. Youngs. *Extremely low frequency plasmons in metallic mesostructures.* Phys. Rev. Lett. **76**(25), 4773-4776 (1996).

[2] J. B. Pendry, A. J. Holden, D. J. Robbins and W. J. Stewart. *Magnetism from conductors and enhanced nonlinear phenomena.* IEEE Trans. Microwave Theory Tech. **47**(11), 2075-2084 (1999).

[3] D. R. Smith, W. J. Padilla, D. C. Vier, S. C. Nemat-Nasser and S. Schultz. *Composite medium with simultaneously negative permeability and permittivity.* Phys. Rev. Lett. **84**(18), 4184-4187 (2000).

[4] V. G. Veselago. *The electrodynamics of substances with simultaneously negative values of ε and μ.* Sov. Phys. Usp. **10**(4), 509-514 (1968).

[5] R. A. Shelby, D. R. Smith and S. Schultz. *Experimental verification of a negative index of refraction.* Science **292**, 77-79 (2001).

[6] J. B. Pendry. *Negative refraction makes a perfect lens.* Phys. Rev. Lett. **85**(18), 3966-3969 (2000).

[7] N. Fang, H. Lee, C. Sun and X. Zhang. *Sub-diffraction-limited optical imaging with a silver superlens.* Science **308**, 534-537 (2005).

[8] J. B. Pendry, D. Schurig and D. R. Smith. *Controlling electromagnetic fields.* Science **312**, 1780-1782 (2006).

[9] D. Schurig, J. J. Mock, B. J. Justice, S. A. Cummer, J. B. Pendry, A. F. Starr and D. R. Smith. *Metamaterial electromagnetic cloak at microwave frequencies.* Science **314**, 977-980 (2006).

[10] H-T. Chen, J. F. O'Hara, A. K. Azad, A. J. Taylor, R. D. Averitt, D. B. Shrekenhamer and W. J. Padilla. *Experimental demonstration of frequency-agile terahertz metamaterials.* Nat. Photonics **2**, 295-298 (2008).

[11] W. J. Padilla, A. J. Taylor, C. Highstrete, M. Lee and R. D. Averitt. *Dynamical electric and magnetic metamaterial response at terahertz frequencies.* Phys. Rev. Lett. **96**, 107401 (2006).

[12] H-T. Chen, W. J. Padilla, J. M. O. Zide, A. C. Gossard, A. J. Taylor and R. D. Averitt. *Active terahertz metamaterial devices.* Nature **444**, 597-600 (2006).

[13] H-T. Chen, W. J. Padilla, M. J. Cich, A. K. Azad, R. D. Averitt and A. J. Taylor. *A metamaterial solid-state terahertz phase modulator.* Nat. Photonics **3**, 148-151 (2009).

[14] S. Linden, C. Enkrich, M. Wegener, J. Zhou, T. Koschny and C. M. Soukoulis. *Magnetic response of metamaterials at 100 terahertz.* Science **306**, 1351-1353 (2004).

[15] S. Zhang, W. Fan, N. C. Panoiu, K. J. Malloy, R. M. Osgood and S. R. J. Brueck. *Experimental demonstration of near-infrared negative-index metamaterials.* Phys. Rev. Lett. **95**(13), 137404 (2005).

[16] G. Dolling, M. Wegener, C. M. Soukoulis and S. Linden. *Negative-index metamaterial at 780 nm wavelength.* Opt. Lett. **32**(1), 53-55 (2007).

[17] T. W. Ebbesen, H. J. Lezec, H. F. Ghaemi, T. Thio and P. A. Wolff. *Extraordinary optical transmission through sub-wavelength hole arrays.* Nature **391**, 667-669 (1998).

[18] L. Martín-Moreno, F. J. García-Vidal, H. J. Lezec, K. M. Pellerin, T. Thio, J. B. Pendry and T. W. Ebbesen. *Theory of extraordinary optical transmission through subwavelength hole arrays.* Phys. Rev. Lett. **86**(6), 1114-1117 (2001).

[19] H. Cao and A. Nahata. *Resonantly enhanced transmission of terahertz radiation through a periodic array of subwavelength apertures.* Opt. Express **12**(6), 1004-1010 (2004).

[20] D. Qu, D. Grischkowsky and W. Zhang. *Terahertz transmission properties of thin, subwavelength metallic hole arrays.* Opt. Lett. **29**(8), 896-898 (2004).

[21] J. B. Pendry, L. Martín-Moreno and F. J. Garcia-Vidal. *Mimicking surface plasmons with structured surfaces.* Science **305**, 847-848 (2004).

[22] F. J. Garcia-Vidal, L. Martín-Moreno and J. B. Pendry. *Surfaces with holes in them: new plasmonic metamaterials.* J. Opt. A: Pure Appl. Opt. **7**, 97-101 (2005).

[23] J-Y. Lu, C-P. Yu, H-C. Chang, H-W. Chen, Y-T. Li, C-L. Pan and C-K. Sun. *Terahertz air-core microstructure fiber.* Appl. Phys. Lett. **92**, 064105 (2008).

[24] A. Hassani, A. Dupuis, M. Skorobogatiy. *Porous polymer fibers for low-loss terahertz guiding.* Opt. Express **16**(9), 6340-6350 (2008).

[25] M. Nagel, A. Marchewka and H. Kurz. *Low-index discontinuity terahertz waveguides.* Opt. Express **14**(21), 9944-9954 (2006).

[26] B. Bowden, J. A. Harrington and O. Mitrofanov. *Low-loss modes in hollow metallic terahertz waveguides with dielectric coatings.* Appl. Phys. Lett. **93**, 181104 (2008).

[27] R. Mendis and D. Grischkowsky. *Undistorted guided-wave propagation of subpicosecond terahertz pulses.* Opt. Lett. **26**(11), 846-848 (2001).

[28] M. Wächter, M. Nagel and H. Kurz. *Mettalic slit waveguide for dispersion-free low-loss terahertz transmission.* Appl. Phys. Lett. **90**, 061111 (2007).

[29] K. Wang and D. M. Mittleman. *Metal wires for terahertz wave guiding.* Nature **432**, 376-379 (2004).

[30] T-I. Jeon and D. Grischkowsky. *THz Zenneck surface wave (THz surface plasmon) propagation on a metal sheet.* Appl. Phys. Lett. **88**, 061113 (2006).

[31] S. A. Maier. *Plasmonics: Fundamentals and applications.* Springer, New York (2007).

[32] P. B. Johnson and R. W Christy. *Optical constants of the noble metals.* Phys. Rev. B **6**(12), 4370-4379 (1972).

[33] M. A. Ordal, R. J. Bell, R. W. Alexander Jr., L. L. Long and M. R. Querry. *Optical properties of fourteen metals in the infrared and far infrared: Al, Co, Cu, Fe, Pb, Mo, Ni, Pd, Pt, Ag, Ti, V and W.* Appl. Opt. **24**(24), 4493-4499 (1985).

[34] W. L. Barnes, A. Dereux and T. W. Ebbesen. *Surface plasmon subwavelength optics.* Nature **424**, 824-830 (2003).

[35] E. Ozbay. *Plasmonics: Merging photonics and electronics at nanoscale dimensions.* Science **311**, 189-193 (2006).

[36] D. P. O'Neal, L. R. Hirsch, N. J. Halas, J. D. Payne and J. L. West. *Photothermal tumor ablation in mice using near infrared absorbing nanoshells.* Cancer Lett. **209**, 171-176 (2004).

[37] G. Goubau. *Surface waves and their application to transmission lines*. J. Appl. Phys. **21**, 1119-1128 (1950).

[38] D. L. Mills and A. A. Maradudin. *Surface corrugation and surface-polariton binding in the infrared frequency range.* Phys. Rev. B **39**(3), 1569-1574 (1989).

[39] R. Ulrich and M. Tacke. *Submillimeter waveguiding on periodic metal structure.* Appl. Phys. Lett. **22**(5), 251-253 (1973).

[40] A. P. Hibbins, B. R. Evans and J. R. Sambles. *Experimental verification of designer surface plasmons.* Science **308**, 670-672 (2005).

[41] J. Gómez Rivas, M. Kuttge, P. Haring Bolivar, H. Kurz and J. A. Sánchez-Gil. *Propagation of surface plasmon polaritons on semiconductor gratings.* Phys. Rev. Lett. **93**, 256804 (2004).

[42] T. H. Isaac, W. L. Barnes and E. Hendry. *Determining the terahertz optical properties of subwavelength films using semiconductor surface plasmons.* Appl. Phys. Lett. **93**, 241115 (2008).

[43] J. Saxler, J. Gómez-Rivas, C. Janke, H. P. M. Pellemans, P. Haring Bolívar and H. Kurz. *Time-domain measurements of surface plasmon polaritons in the terahertz frequency range.* Phys. Rev. B **69**, 155427 (2004).

3. Development of a fibre-coupled terahertz time-domain spectrometer

3.1. Introduction

Since its inception [1,2,3,4] terahertz time-domain spectroscopy (TTDS) has developed into a powerful spectroscopic technique, enabling coherent detection with sub-ps time resolution and high sensitivity. Coherent detection refers to the measurement of electric field rather than intensity, so that both amplitude and phase information are obtained. The crux of the technique is the division of a single train of optical pulses into two separate beams, the so-called pump and probe. Pulses in the pump beam are used to generate terahertz radiation whilst those in the probe arm are used to gate the detector. Generally, photoconductive antennas are used to generate and coherently detect radiation, although an alternative approach uses optical rectification and electro-optic sampling (EOS) [5]. In the latter case, broadband terahertz radiation is produced via difference frequency mixing in an electro-optic crystal displaying large $\chi^{(2)}$ non-linearity, such as ZnTe or GaSe. In EOS, the terahertz electric field is measured by recording the change in polarisation experienced by an optical probe pulse collinearly focussed with the terahertz pulse onto an electro-optic crystal with large electro-optic coefficient such as ZnTe or GaSe. In this case, the terahertz electric field induces birefringence and thus a change in the polarisation state of the probe pulse.

In this work, terahertz generation and detection is achieved using photoconductive antennas (as described in section 3.4). For terahertz generation, above bandgap optical pump pulses are used to generate photocarriers in a high-resistivity semiconductor located between two metal tracks. A bias field applied between the electrodes accelerates the photocarriers, producing a rapidly varying photocurrent that radiates bursts of electromagnetic radiation into free-space, synchronous with the optical pump beam [6]. Pulses from the probe beam are simultaneously used to gate a normally insulating photoconductive region between the arms of a dipole

receiving antenna [1]. In the presence of a terahertz electric field, a transient bias is induced across the antenna. This creates a photocurrent proportional to the strength of the terahertz electric field provided that the photoconductor is switched to the conducting state by a probe pulse. Scanning the delay between pump and probe pulses allows mapping of the receiver current as a function of time. In practice, sub-ps carrier lifetimes are required to reduce noise. This is achieved by introducing defects into the photoconductive layer in order to quickly trap photocarriers, either via ion-implantation or low-temperature growth. This method of detection is exceptionally sensitive due to the fact that the receiver is only 'switched on' in the presence of both the optical and terahertz pulses (~400fs every ~10ns) making it insensitive to the incoherent thermal background.

Most TTDS systems rely on free-space optics such as mirrors and lenses for manipulation of the optical beams, but suffer from being inherently inflexible to changes in experimental geometry due to the requirement for careful component realignment and optical delay adjustment. A solution to this problem is provided by fibre-coupled TTDS systems. A commercially available fibre-based TTDS system has been developed by van Rudd et al. [7] and is distributed by Picometrix [8]. This system utilises standard solid-core step-index single mode fibres (SMFs) which introduce significant dispersion. To minimise broadening and loss of terahertz bandwidth, second order dispersion can be compensated using a grating pair [9], but these extra components make the system less compact. In addition, only relatively low average powers (<10 mW for fibre lengths more than a few metres) can be tolerated before the onset of nonlinear broadening mechanisms such as self phase modulation (SPM) [10]. As a result, in the few fibre-coupled TTDS systems characterised to date in the literature [7,9,11] the dynamic range is limited to ~7000 and useful bandwidths are less than ~1.5 THz. In order to improve dynamic range and potentially system bandwidth, different fibre architectures are required. In a paper by Lee et al. [12] it was demonstrated that the use of solid-core large mode area photonic crystal fibres (LMA-PCFs) in which the effective core area is increased by an order of magnitude, enable nonlinearity to be suppressed sufficiently to increase the useful bandwidth by ~50% compared to an SMF based system under comparable conditions (from ~0.8 THz to ~1.2 THz in this case). Unfortunately, for pulse powers >10 mW the 100

fs input pulses are still broadened by the ~2 m LMA-PCF to >140 fs due to the combined effect of group velocity dispersion (GVD) and SPM.

Hollow-core photonic crystal fibres (HC-PCFs) [13] offer an attractive alternative to the solid-core and large mode area fibres discussed so far, allowing pulses to be delivered at relatively high power with low dispersion. These properties are achieved by concentrating the guided mode within a hollow air-core. HC-PCFs exhibit higher damage thresholds, a three orders of magnitude reduction in nonlinear refractive index and dispersion that is controlled by the fibre structure rather than the constituent materials. Unlike solid-core PCFs which guide via total internal reflection, hollow-core fibres exploit band-gap guidance to trap a large proportion of light within the low-index core [14]. An important property of this fibre architecture is a region of low GVD which changes sign near the lower wavelength band edge. In the positive or normal GVD regime, the low frequency components travel faster than the high-frequency components and a short pulse acquires a positive chirp, whereas in the negative or anomalous regime the opposite is true. Therefore, by working slightly above the zero dispersion wavelength, the HC-PCF can be used to provide negative GVD and compensate for positive second-order dispersion from other optical components in the system. This removes the requirement for external dispersion compensation, making the system more compact and less prone to drift.

In the remainder of this chapter we describe the characteristics of a fibre-coupled TTDS system constructed using HC-PCF. We start by describing the optical part of the system (section 3.2) and the HC-PCFs (section 3.3). This is followed by a discussion of the terahertz optics in section 3.4. Results for the free-space characterisation of the fibre-coupled TTDS system are described in section 3.5 and the extension of the system to facilitate near-field probing is discussed in section 3.6.

3.2. The optical system

A train of ~80 fs full-width half-maxima (FWHM) pulses with an 82 MHz repetition rate are generated using a mode-locked, argon-ion pumped Ti:sapphire laser (Spectra Physics Tsunami). In this process, an acousto-optic modulator (AOM) driven at half the longitudinal laser mode beat frequency is used to introduce periodic loss into the cavity. This process phase locks the longitudinal cavity modes and produces a train of ultrashort pulses. Material dispersion is compensated using a prism pair to provide negative GVD. Self-focussing within the Ti:sapphire rod ensures that mode-locking is maintained once it is initiated by the AOM. Self focussing is the spatial analogue of SPM and occurs within a medium with non-zero nonlinear refractive index [10]. In this process, the centre of the optical pulse which is most intense, experiences a higher refractive index than the weaker edges such that the net phase distortion across the transverse beam profile results in beam focussing. The introduction of a slit aperture within the laser cavity isolates the intense laser pulse train and its width controls the pulse bandwidth.

With ~8.25 W pump power, the femtosecond oscillator provides typical output powers of ~650-800 mW over the wavelength range 760-810 nm. The laser beam (average power ~740 mW at 778 nm) is directed to an optical isolator which is used to prevent reflections from the HC-PCF faces feeding back into the laser and causing instability. This component is the major source of positive dispersion. The beam is then divided by a beamsplitter to form the pump and probe arms. Approximately 60% of the power (~270 mW) is sent to the pump arm and ~40% (~185 mW) to the probe fibre. A half wave-plate placed before the beam-splitter allows the ratio to be varied.

The pump beam is chopped at 2.5 kHz to allow lock-in detection and directed into a rapid (up to ~4 Hz) scanning delay line based on a galvanometer and hollow-corner-cube retro-reflector. The rapid-scanning action helps overcome the problem of laser drift and allows real time optimisation of the terahertz signal. The beam is then launched, using a x20 microscope objective, into a ~1.5 m

length of HC-PCF designed for operation at wavelengths near 800 nm (section 3.3). The output beam from the pump fibre is collimated and then focussed onto the transmitter chip using an *f*=4.3 mm aspheric lens. The operation of the terahertz transmitter is described in section 3.4.

From the beam-splitter, the probe beam is sent to a long-range variable delay line consisting of a hollow-corner-cube retro-reflector mounted on a stepper motor driven stage. This allows the pump-probe delay to be varied over ~1 ns. The probe beam is launched in an identical fashion into a second length of HC-PCF (~1.5 m). An identical arrangement to the pump fibre is used at the output, allowing the optical probe beam to be focussed onto the terahertz receiver described in section 3.4. A flip-mirror located before the objective lens on the input side allows the probe beam to be redirected to a near-field probing arm described in section 3.6.

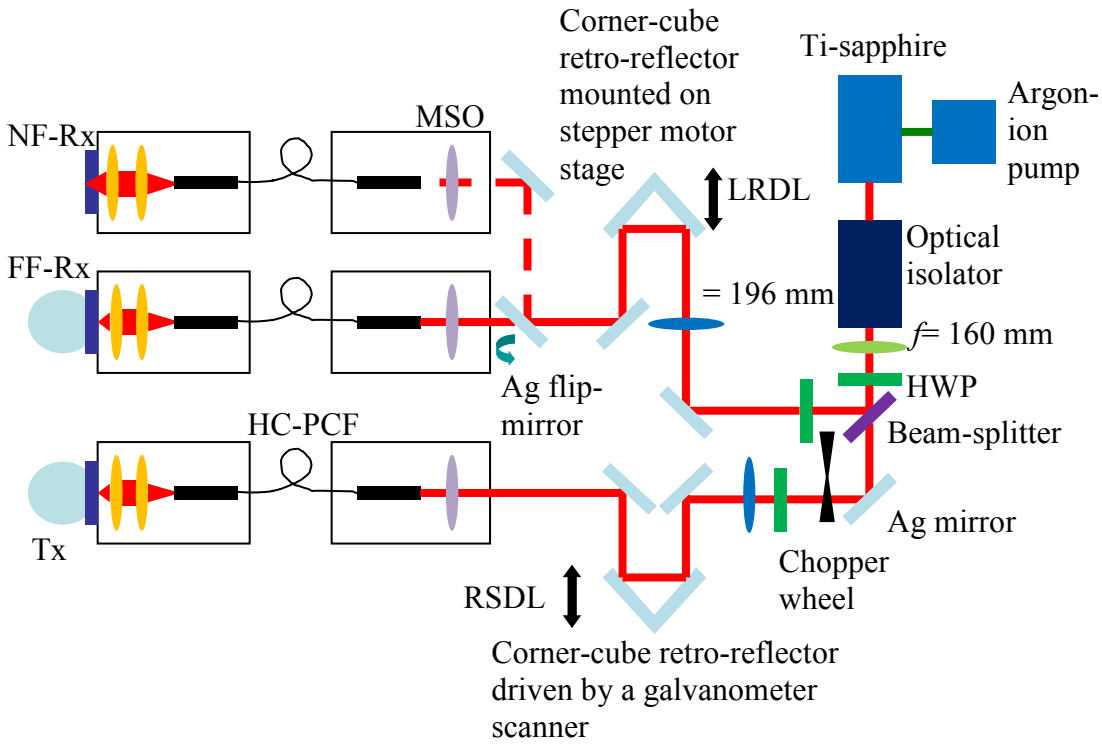

Figure 3.1. Schematic diagram of the entire TTDS system. HWP= half waveplate, RSDL= rapid scanning delay line, HC-PCF= hollow-core photonic crystal fibre, Tx= transmitter, LRDL= long-range delay line, MSO= x20 microscope objective, FF-Rx= far-field receiver, NF-Rx= near-field receiver (section 3.6).

In order to match the numerical aperture of the HC-PCF and maximise fibre throughput, *f*=196 mm lenses are inserted into each arm of the beam, forming a pair with a common *f*=160 mm lens located before the beam-splitter (figure 3.1). Varying the distance between each lens-pair allows the beam diameter to be fine-tuned at the microscope objective. Together with half-waveplates placed before each fibre coupler, which allow for birefringence in the fibres, this allows optimisation of the fibre coupling. For freshly cleaved fibres, coupling efficiencies of ~25-30% can be achieved in our setup, in good agreement with values previously reported [15]. This value was found to degrade slightly with time due to dust and moisture penetration at the cleaved fibre faces. In order to minimise this effect, the whole system is located in a sealed enclosure and purged with dry air. In order to monitor the fibre transmission, beam-splitters at the output of each fibre are used to direct the collimated output beams to a photodiode as shown in figure 3.2. The beam-splitters also allow a camera to be introduced to ensure optimal focussing and positioning of the optical spots at the transmitter and receiver.

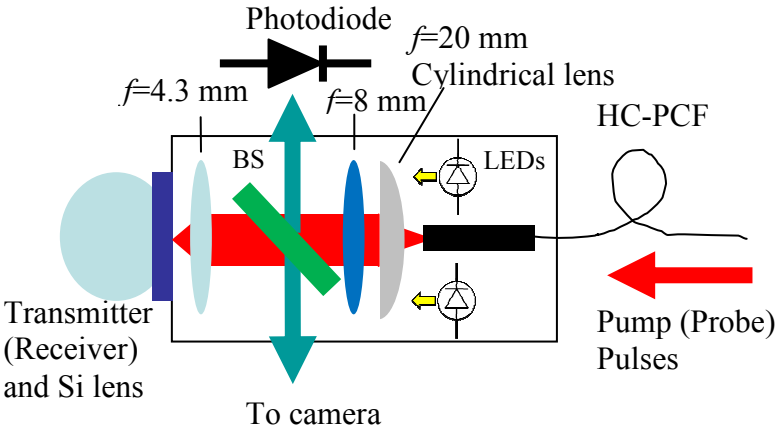

Figure 3.2. Schematic of the transmitter (receiver) HC-PCF output stage. BS= beam-splitter. The f=20 mm cylindrical lens is omitted in the receiver configuration.

At a centre wavelength of 778 nm (chosen to obtain the maximum terahertz signal), ~72 mW of unchopped power is available from the pump fibre and ~40 mW from the probe fibre. For probe fibre throughputs >25 mW the receiver response is found to saturate, so the excess power in this arm is attenuated at the

input side to reduce receiver noise. On both the transmitter and receiver sides the fibre holders and focussing lenses are held on translation stages to allow positioning and focussing of the optical spot with ~1 μm sensitivity. A cylindrical lens is inserted into the transmitter output stage to provide line focussing, allowing more optical power to be applied before the onset of device saturation or damage [16]. Finally, it is important to emphasise that in our setup, both the transmitter and receiver stages are freely repositionable with respect to one another so that changes in experimental geometry are easily facilitated without realignment of the visible optics.

3.3. Optical fibre characterisation

The HC-PCF used in our system was designed for use at 800 nm [15]. The fibre has a 7-cell defect core with diameter ~8 μm. A scanning electron microscope (SEM) image of the end face of the cleaved fibre is shown in figure 3.3.

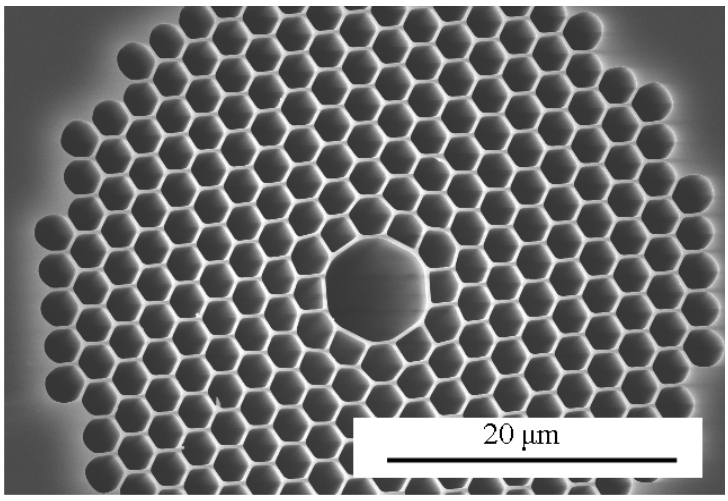

Figure 3.3. SEM image of the cleaved HC-PCF face. Dark regions represent air, light regions silica.

To quantify the wavelength dependent pulse broadening due to the HC-PCF, the output pulse width was measured using interferometric autocorrelation [17]. This technique involves measuring the interference between two time delayed beams

derived from the same source. In our setup (figure 3.4) both beams are focussed onto a GaAsP Schottky photodiode with bandgap larger than the single photon energy, such that the two time-delayed pulses, *E(t)* and *E(t+Δt)*, generate a two-photon absorption signal proportional to *I(Δt)*, given by,

$$I(\Delta t) = \int \left| \left(E(t) + E(t + \Delta t) \right)^2 \right|^2 dt \tag{3.1}$$

For the case where $\Delta t = 0$, we have,

$$I(0) = 16 \int E^4(t) dt \tag{3.2}$$

and for large delays where the fields add incoherently,

$$I(\Delta t) = 2 \int E^4(t) dt \tag{3.3}$$

For $\Delta t = n\pi$, the fields from the two beams are out of phase and *I(Δt)* is a minimum. Counting the number of interference maxima in the autocorrelation trace provides a measure of the temporal pulse width, provided that the input pulse shape is known and the spectral phase is approximately constant.

In order to extract the pulse width Δt, from the autocorrelation width $\Delta \tau$, the input pulse shape must be known. In this work, a sech^2 pulse shape envelope is assumed, which is the common approximation for self mode-locked laser systems. In this case, the pulse and autocorrelation FWHM, with zero defined as the minimum below the hang-line, are linked by the deconvolution factor $\Delta t / \Delta \tau = 0.527$ [17].

By counting the number of interference fringes over the FWHM (*n*), the pulse width can be obtained using,

$$\Delta t = 0.527 n \left(\frac{\lambda_0}{c} \right) \tag{3.4}$$

where λ_0 is the centre wavelength of the laser. An example autocorrelation trace is shown in figure 3.5 and results for the pulse width at the fibre output as a function of centre wavelength are shown in figure 3.6.

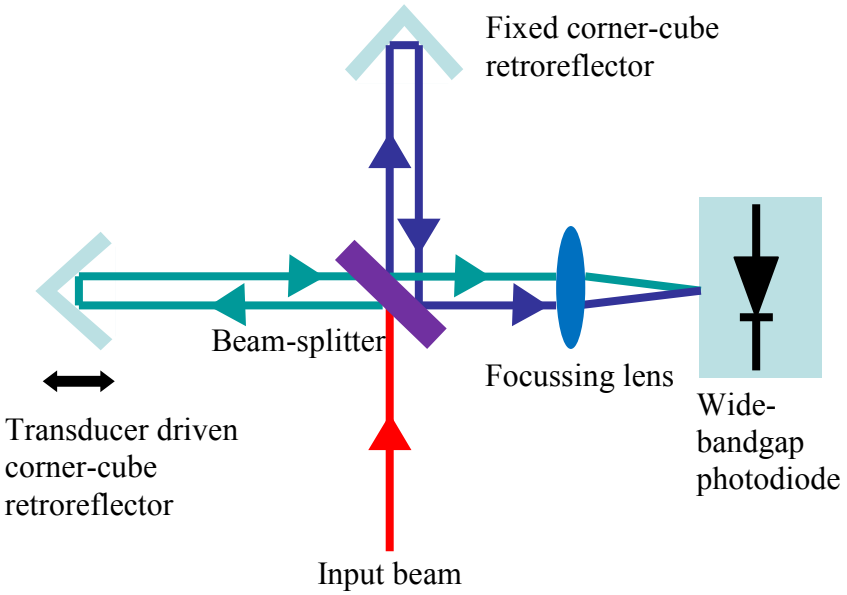

Figure 3.4. Schematic diagram of the interferometric autocorrelator.

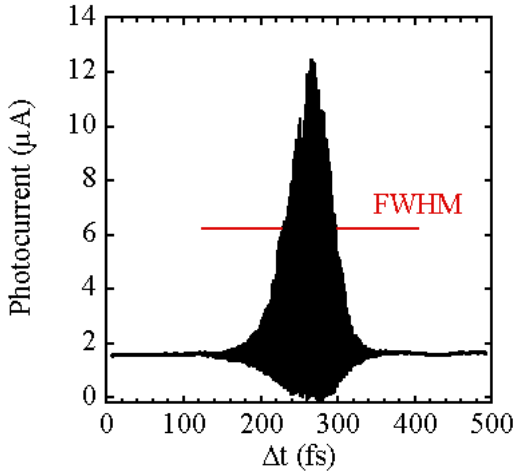

Figure 3.5. Autocorrelation trace obtained at a centre wavelength of 778 nm.

Figure 3.6 shows that the minimum pulse width of ~85 fs is obtained at 772 nm and remains below 100 fs over the range 767 nm to 778 nm. It is important to appreciate that the minimum pulse width at 772 nm lies above the zero dispersion wavelength which lies near 765 nm. This demonstrates that by shifting to longer wavelengths, where the value of the dispersion is more negative, it is possible to provide second-order dispersion compensation, producing shorter optical pulse lengths. To provide a reference, the laser pulse width was measured over the same wavelength range and found to be constant at ~80 fs for a pulse bandwidth of ~9 nm. The 9 nm pulse bandwidth used in these measurements sets a fundamental limit on the minimum achievable pulse width (~71 fs at 780 nm) corresponding to the transform-limit for a sech^2 pulse shape, given by $\Delta t = 0.315/\Delta v$. The ~10 fs broadening of the optical pulse in our system can probably be attributed to a combination of the formation of surface modes due to coupling between the core and cladding modes in the fibre [13] and third-order dispersion.

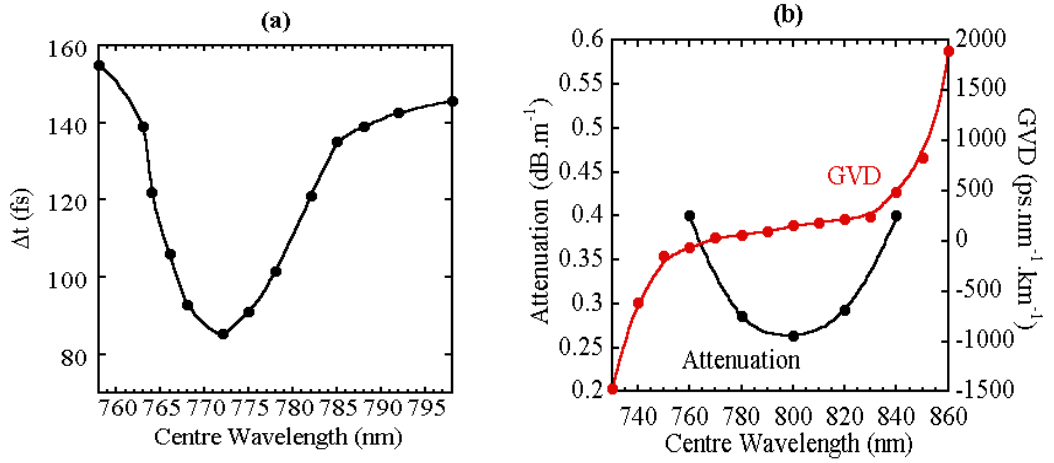

Figure 3.6. (a) HC-PCF output pulse width as a function of centre wavelength for 9 nm laser pulse bandwidth input pulse. (b) HC-PCF attenuation and GVD data from Luan et al. [15]. In this plot the region of GVD>0 represents anomalous (negative) dispersion.

3.4. The terahertz system

3.4.1. Photoconductive transmitters

In the Hertzian dipole approximation the far-field transient electric field *E(t)* radiated by a photoconductive transmitter is given by [18],

$$E(t) \propto \frac{dJ(t)}{dt} = \left(\frac{dn(t)}{dt}\right) ev(t) + n(t) e\left(\frac{dv(t)}{dt}\right) \tag{3.5}$$

where *J(t)* is the photocurrent density, *n(t)* is the number density of photo-carriers produced by the optical pump pulse and *v(t)* is the photo-carrier velocity. This expression can be reformulated in terms of the mobility $\mu(t)$ and bias field *F*, using $v(t) = \int \mu(t - t') F(t') dt'$, which allows for variations in the bias field with time and the frequency dependence of the mobility.

Figure 3.7 shows normalised temporal profiles of the optical pulse amplitude, photocurrent and far-field electric field amplitude calculated from equation 3.5 using a simple model [19] in which the effects of electron-hole screening [20] are neglected and only electrons are considered to contribute to the photocurrent. In this model the optical pulse profile is assumed to be Gaussian, free-carrier relaxation is assumed to follow a single exponential decay and the bias field is assumed to be constant over the illuminated area.

It is clear from figure 3.7 that the terahertz pulse width and hence bandwidth is dominated by the fast rise-time of the photocurrent, whereas the relatively long photocarrier lifetime mainly affects the terahertz pulse shape. The small role of the carrier lifetime in determining the terahertz bandwidth has been confirmed experimentally by comparing emission from transmitters made from low-temperature grown (LT-) and semi-insulating (SI-) GaAs [21], which exhibit ps and hundreds of ps carrier lifetimes respectively. The emission efficiency of a photoconductive antenna is directly proportional to the dc carrier mobility and at low illumination levels also to the bias field. Maximising the first contribution

requires the use of high-mobility semiconductors. However, high resistivities are required to support large bias fields and maximise the second contribution. Materials such as SI-GaAs (ρ~10 MΩcm, μ~5000 $cm^2V^{-1}s^{-1}$) and LT-GaAs (ρ~100 MΩcm, μ~300 $cm^2V^{-1}s^{-1}$) which exhibit high resistivity as well as reasonable mobility provide the most efficient photoconductive sources. In the latter case it is important to appreciate that the terahertz mobility may be significantly larger than the dc value due to the effects of fast carrier trapping [22].

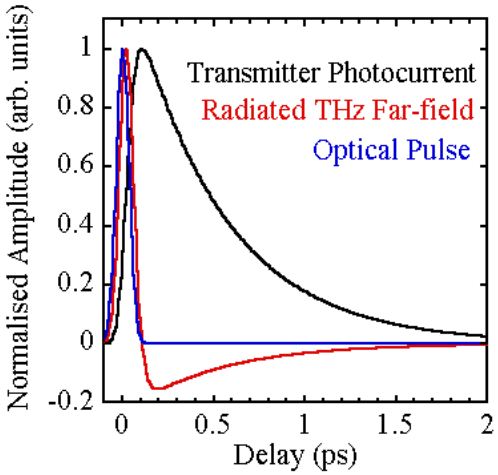

Figure 3.7. Time variation of the photocurrent (black), radiated electric far-field amplitude (red) and optical excitation pulse (blue). In these plots the recombination time is 500 fs, the mobility scattering time is 30 fs and the laser pulse width is 80 fs.

The transmitter devices used in this work consist of a biased coplanar waveguide, with Ti/Au electrodes deposited on a SI-GaAs or LT-GaAs substrate (figure 3.8). An external bias of ~50 V (SI-GaAs) or ~100 V (LT-GaAs) is applied between the tracks and <100 fs pulses with average power ~36 mW are focussed onto the device so as to slightly overlap the junction between the positively biased electrode and the semiconductor substrate. The emitted field is largest when the laser spot is focussed at the edge of the anode and falls off quickly as the spot is moved away. Close to the cathode the field increases once more, although in this case to a lower absolute value. This behaviour is due to the higher mobility of

electrons, as well as trap enhancement of the field close to the anode [23]. Line-focussing is implemented using a cylindrical lens and microscope objective. The LT-GaAs device typically produces transients with twice the amplitude of the SI-GaAs device. In all experiments, the applied bias was restricted to keep the average photocurrent below ~1 mA (SI-GaAs) or ~0.5 mA (LT-GaAs). Above these values the device lifetime was found to be dramatically reduced. Many effects can influence this threshold, including electromigration and dielectric break down caused by the large dc bias field, as well as excess Ohmic heating and thermal runaway caused by the dc photocurrent.

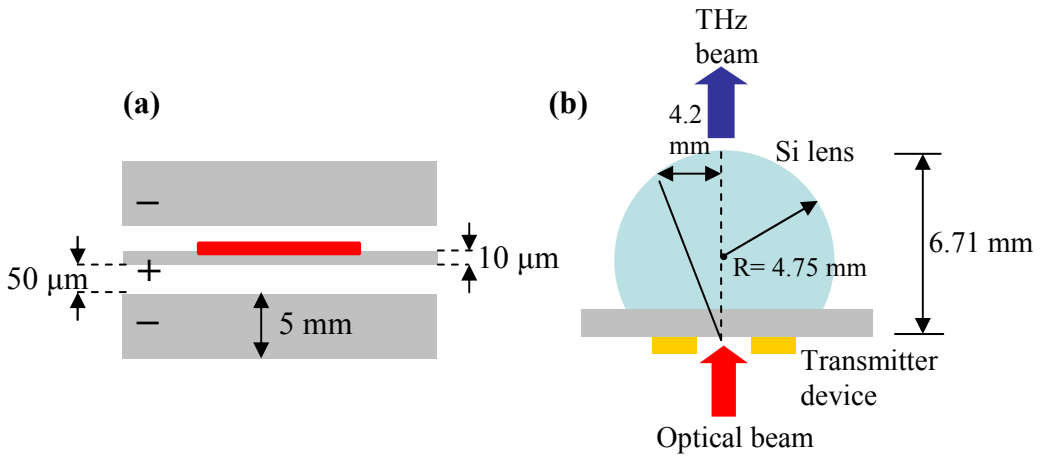

Figure 3.8. (a) Schematic diagram of the coplanar transmitter, showing the positioning of the line focussed laser spot in red and the Ti/Au tracks in grey. (b) Schematic diagram of the transmitter-lens assembly.

Most of the terahertz radiation generated according to equation 3.5, is emitted into the substrate and totally internally reflected at the substrate-air interface. For this reason, an index-matched high-resistivity $(\rho \sim 10\,\mathrm{k\Omega cm})$ hyper-hemispherical silicon lens attached to the backside of the transmitter chip is used to improve the collection efficiency [4]. High-resistivity silicon is chosen due to its exceptionally low loss and dispersion over the frequency range 0.1- 5 THz [24]. The lens is designed so that for paraxial light, the device is located at its focal point. A thin layer of paraffin oil applied between the substrate and lens keeps the two in optical contact whilst maintaining manoeuvrability in the plane of the substrate.

The lens is held on a spring and fitted to a two-axis translation stage to enable precise alignment.

In order to generate radially polarised THz radiation (chapter 6), an annular geometry SI-GaAs photoconducting antenna was fabricated (figure 3.9). This device consists of two concentric Ti/Au electrodes deposited on SI-GaAs. The positively biased inner electrode has a diameter of 20 μm and the outer electrode has an inner diameter of 120 μm. The optical pump beam is focussed so as to overlap the central electrode. An external bias of ~20 V was applied to keep the illumination photocurrent below ~1 mA. Unlike previous designs reported in the literature [25,26], a germanium screen isolated from the metal tracks by a 5 μm thick SiO_2 layer was deposited as shown in figure 3.9(b). The ring-focussing imposed by the opaque but insulating screen was found to significantly reduce the dc photocurrent. This enabled the applied bias to be doubled, increasing the signal by a factor of ~2. The ring-focussing was also found to slightly improve the system bandwidth as illustrated in figure 3.10(b).

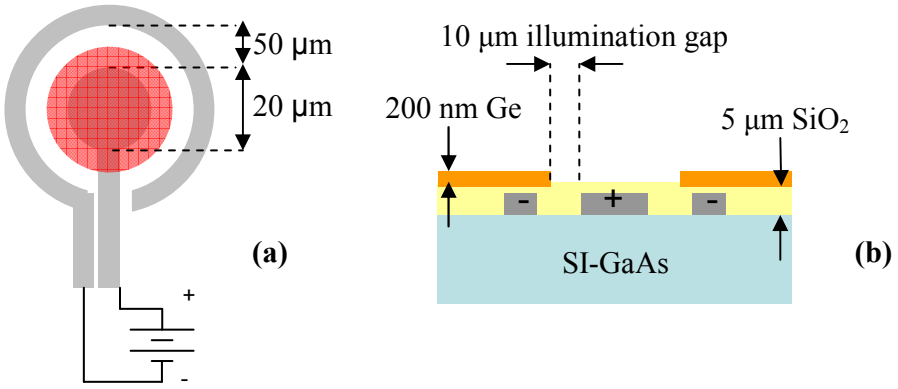

Figure 3.9. (a) *Schematic diagram of the radial transmitter, showing the positioning of the laser spot in red and the Ti/Au tracks in grey. (b) Profile view indicating the positioning of the Ge screen.*

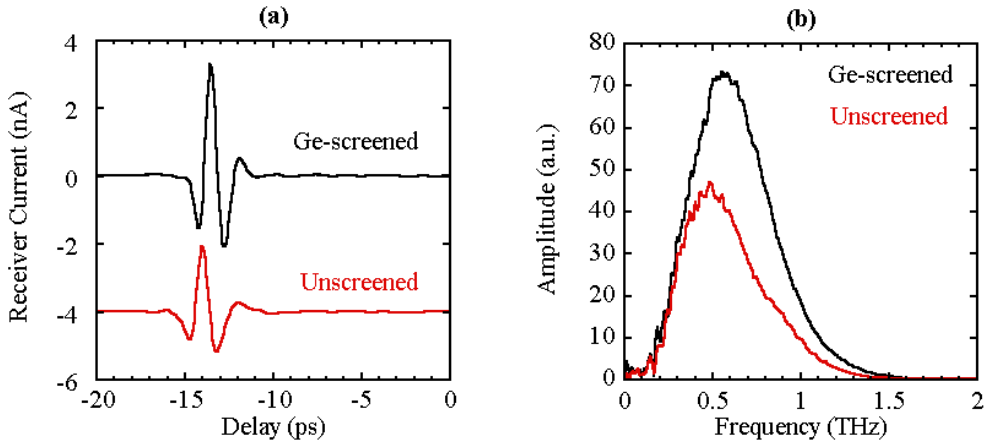

Figure 3.10. Comparison of (a) time-domain traces and (b) spectra obtained using screened and unscreened radial transmitter designs. Signals were captured without external collimating optics for a transmitter to receiver separation of ~25 cm.

The polarisation of the terahertz radiation emitted from the coplanar and radial transmitters was compared using a crossed-bow-tie receiver to simultaneously measure the terahertz field in horizontal and vertical detection planes [27]. For the coplanar transmitter design, the horizontal to vertical polarisation ratio (HVPR), defined as the ratio of the peak to peak receiver currents measured in the two perpendicular detection planes, was found to be ~25:1. This demonstrates that the electric field component of the emitted terahertz radiation is predominantly polarised parallel to the dc bias field. For the radial transmitter the HVPR was ~2:1 which departs from the 1:1 HVPR expected for a perfectly radial source. The discrepancy can at least be partly attributed to the anode feed-line which breaks the annular symmetry [28].

3.4.2. Photoconductive receivers

The first photoconductive terahertz receivers described in the literature were fabricated on radiation damaged silicon-on-sapphire (SOS) by Auston et al. [1]. Since then several other materials have been explored in pursuit of improved device performance. In practice, the choice of material involves finding an

optimal compromise between mobility, resistivity and trapping time. In terms of dynamic range, devices based on ion-implanted or low-temperature grown GaAs have been shown to outperform those based on other materials such as silicon [16].

In this work, two dipole receivers were used. The smaller (larger) device consists of a pair of 10 μm wide parallel Ti/Au tracks separated by 10 μm (50 μm). A narrower region, 20 μm wide, forms two 2.5 μm (22.5 μm) long antenna arms which extend to leave a 5 μm gap as shown in figure 3.11. This dipole antenna region is bridged by a photoconductor made from ion-implanted GaAs (1 μm thick), which has a 300-400 fs carrier lifetime, on a SI-GaAs substrate (~450 μm thick). An insulating AlAs layer (100 nm thick) was used to provide electrical isolation between the photoconductive layer and substrate. Multiple arsenic implantation (2 MeV at 5.4×10^{15} cm^{-2}, 1 MeV at 3.1×10^{14} cm^{-2} and 0.45 MeV at 1.5×10^{14} cm^{-2}) enabled a flat damage profile to be obtained over the active layer thickness. In order to optimise the mobility and carrier lifetime, the devices were annealed in nitrogen at 500°C for 20 minutes following implantation. The ion-implanted layer was then etched away except for a 50 μm wide region containing the dipole in order to reduce the noise associated with the resistance between the tracks. The receiver photocurrent is amplified using a current to voltage transceiver with a bandwidth of 8 kHz at 10^7 VA^{-1} (3 kHz at 10^8 VA^{-1}) and lock-in detection was implemented at 2.5 kHz.

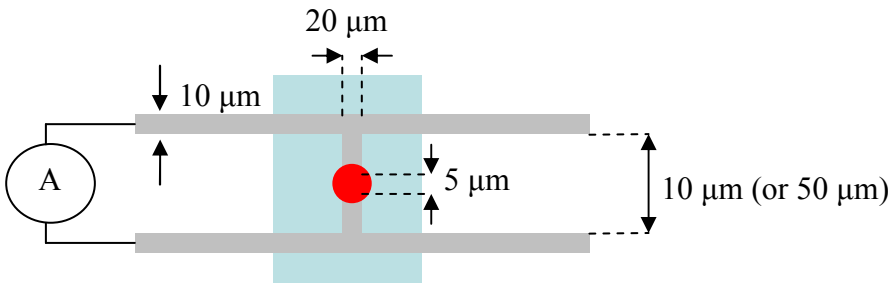

Figure 3.11. Schematic diagram of the 10 μm (50 μm) receiver device, showing the positioning of the focussed laser spot in red, the Ti/Au tracks in grey and the ion-implanted GaAs photoconductive region in blue.

The dynamic range of a terahertz system is defined by the ratio of signal amplitude to receiver noise. The total root-mean-square (RMS) noise is dominated by the thermal (Johnson) contribution which is given by,

$$I_{RMS} = \sqrt{\frac{4k_B T \Delta f}{R}} \tag{3.6}$$

where Δf is the detection bandwidth and R is the average resistance of the photoconducting gap (usually ~1 MΩ). There is also a smaller component due to dc current fluctuations given by,

$$I_{RMS} = \alpha I_{dc} \sqrt{\Delta f} \tag{3.7}$$

where α is the fractional laser noise (~4.10^{-6} $Hz^{-1/2}$ at 2.5 kHz chopping frequency) and I_{dc} is the dc photocurrent (~1 nA). For the arsenic implanted receiver devices used in this work, the noise under illumination was measured to be ~400 $fA/Hz^{-1/2}$ at 2.5 kHz, corresponding to an absolute value of ~110 fA with 1 s lock-in time constant.

3.5. Free-space system characterisation

The size of the gating window, defined by the optical pulse width, sets an upper limit of ~10 THz on the system bandwidth for ~100 fs pulses. In reality the high frequency parts of the spectrum are lost due to the frequency dependent collection efficiency of the dipole antenna as well as the transfer function of the terahertz optics (silicon lenses etc.). For this reason, the system bandwidth is strongly influenced by the components used for collecting, collimating and focussing the terahertz beam.

In order to obtain optimal bandwidth and signal strength, a pair of 90^o off-axis parabolic mirrors separated by a distance equal to the sum of their focal lengths were inserted between the transmitter and receiver to complete the collimation of

the terahertz beam and tighten the focus at the receiver [4]. Introduction of the mirror-pair was found to increase the receiver current by a factor of ~5 compared to a measurement without the mirror pair in place at an identical transmitter-receiver separation. Removing the receiver silicon lens in this geometry reduced signals by a factor of ~15.

An example of the signals obtained using the coplanar transmitter with the 10 µm and 50 µm dipole receivers is shown in figure 3.12. The time-domain traces display a characteristic shape. The small dip preceding the main positive transient is due to the frequency dependence of the focal spot size of the silicon receiver lens and the large dip following the main pulse is due to dynamic screening of the transmitter bias field. It is clear from figure 3.12 that larger values of the receiver current, which is proportional to the terahertz electric field, are obtained with the 50 µm receiver device (~25 nA), at the expense of poorer detection bandwidth (10% fall-off at ~1.5 THz). In contrast, the 10 µm device provides larger detection bandwidth (10% fall-off at ~2.2 THz) at the expense of reduced detection amplitude (~18 nA). From these results, the dynamic range of our system is calculated to be ~2.10^5, ~30 times higher than the commercialised system distributed by Picometrix [7]. This difference can be directly attributed to the thirty-fold increase in average optical power delivered by the HC-PCFs.

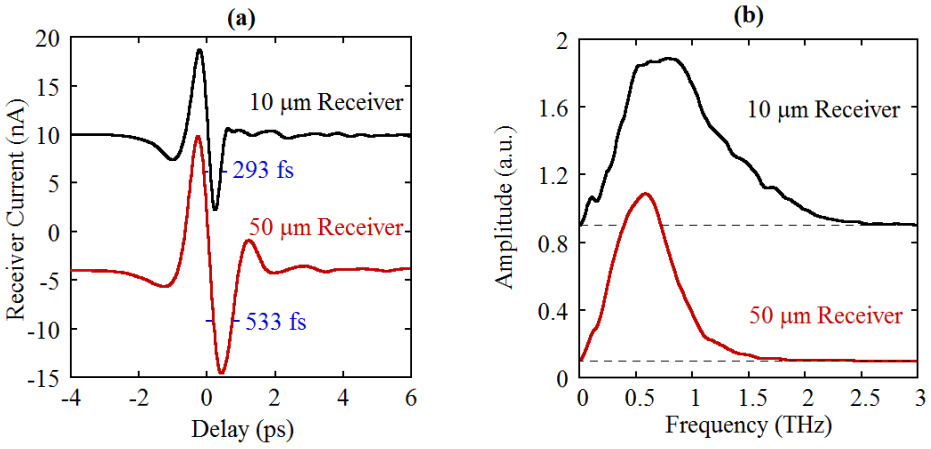

Figure 3.12. (a) Free-space time-domain traces and (b) spectra obtained using the coplanar SI-GaAs transmitter and 10 µm (red) and 50 µm (black) ion-implanted GaAs dipole receivers. The spectra are vertically offset for clarity and the horizontal dashed lines correspond to the position of zero amplitude.

3.6. Development of a fibre-coupled near-field receiver

3.6.1. Introduction

Nearly all terahertz imaging experiments reported to date have been conducted using propagating waves in the far-field, where diffraction limits the spatial resolution to of order the wavelength. Near-field probing detects both propagating and evanescent waves, thus allowing the diffraction limit to be beaten. In terms of metamaterial research, it is conceivable that near-field probing could allow the spatial confinement of SPPs to be probed directly by measuring the evanescent out-of-plane electric field component. In the context of this thesis, this idea provided the key motivation for fabricating and testing a series of near-field probes.

Since its first demonstration in 1998 [29] terahertz near-field studies have received increasing attention in the literature. To date, probing schemes can be grouped into two categories, aperture-based and apertureless. The first technique typically uses a metal aperture fixed in front of a photoconducting dipole antenna. In this case, the spatial resolution is dictated by the aperture diameter and not the free-space wavelength of light or the dipole size [30]. The problem with this technique is the low transmission through the aperture which, for apertures smaller than the dipole length, has been reported to scale with the third power of the diameter [31]. This leads to a fundamental trade-off between the detection efficiency and spatial resolution. The aperture also acts as a high-pass filter and the metal screen may interfere with the fields being probed.

To date, aperture-based terahertz near-field probes have been constructed from LT-GaAs photoconductive antennas fabricated on sapphire substrates. A spatial resolution of ~7 μm was reported with a ~5 μm diameter aperture and ~4 μm dipole-aperture separation, at a probe-sample distance of ~2 μm [31]. Near-field probing has also more recently been demonstrated using apertureless silicon-on-sapphire photoconductive antennas, optically illuminated through the sapphire substrate [32]. In this case, the detection area of the dipole antenna defines the

spatial resolution [33]. Another near-field probing technique relies on placing an object in close contact with an electro-optic crystal such as GaP [34]. In this case the terahertz near-field is measured using EOS and the resolution depends on the optical spot size. Using this technique, resolution down to ~λ/100 (<10 μm) has been demonstrated whilst probing field distributions near rectangular apertures [35]. The techniques discussed so far are the only schemes capable of measuring fields directly.

The first apertureless terahertz near-field probe was demonstrated by van der Valk and Planken in 2002 [36]. In this scheme terahertz pulses are focussed onto a sharp metal tip held in close proximity to a <100> oriented GaP electro-optic crystal. EOS is then used to detect the field component perpendicular to the crystal surface which is strongest in the immediate vicinity of the tip. In this approach the spatial resolution is set by the optical spot focussing. A variation on this technique involves vibrating a subwavelength metal tip in the immediate vicinity of a sample and detecting the scattered terahertz radiation synchronously in the far-field [37]. This technique was originally demonstrated using a stationary tip [38] and shown to yield spatial resolution down to ~150 nm at 2 THz (~λ/1000), limited only by the tip radius. More recently, a vibrating tip was used by Huber et al. [39] to probe doping densities in semiconductor nanostructures with spatial resolution of ~40 nm at 2.54 THz (~λ/3000). Tip-based techniques offer by far the best spatial resolution reported, but can only be used for imaging surfaces rather than probing fields directly.

3.6.2. Device fabrication

In this work, a series of aperture-based 10 μm photoconductive dipoles were fabricated. Firstly, antenna structures were created on LT-GaAs using standard photolithography. Each device was then glued face down to a sapphire substrate using UV curing epoxy. The substrate was then etched down to an AlAs stop-layer using a combination of wet-etching and reactive ion-etching. Finally, the

AlAs was removed in dilute hydrofluoric acid. The final probe structure is shown in figure 3.13.

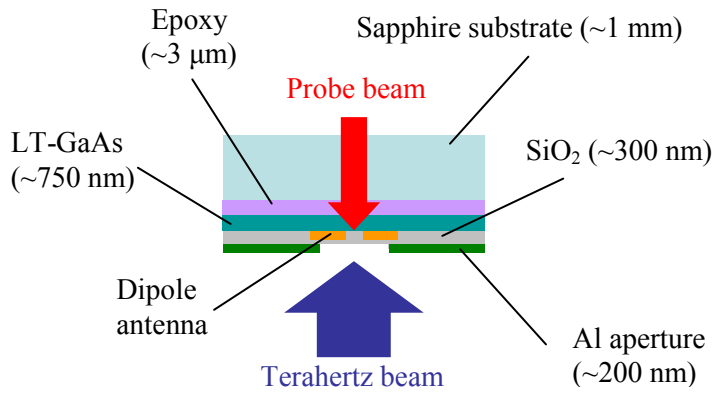

Figure 3.13. Schematic diagram of our aperture-based near-field probe design.

In order to enable the probe-sample separation to be reduced without restriction, the electrical contact pads were placed off the chip surface. This was achieved by bevelling the edges of the sapphire substrate and extending the contact pads onto the bevelled sapphire surfaces. To isolate the antenna from the metal screen, a thin (~300 nm) SiO_2 layer was evaporated on top of each device. Two different near-field probe designs were fabricated. Device I consisted of a 10 μm dipole with 60 μm aperture and device II consisted of a 10 μm dipole with 20 μm aperture. The apertures were formed in a 200 nm thick aluminium screen deposited on top of the SiO_2.

As mentioned in section 3.2, a flip-mirror was used to redirect the optical probe beam into the near-field arm, where the beam was launched into a third ~1.5 m length of HC-PCF using an identical in-coupling arrangement to that already described. The output of the near-field fibre was collimated and focussed using a pair of f=6 mm lenses and the whole assembly was mounted on a motorised three-axis translation stage to enable micron scale translation of the probe. Although fibre throughputs >40 mW were possible using this setup, the power was reduced to ~8 mW to avoid damage to the optical epoxy caused by heat-induced out-gassing.

3.6.3. Device characterisation

Figure 3.14 shows time-domain traces and spectra obtained with the different near-field probes. For the smaller aperture probe it is clear that the high-pass behaviour of the aperture acts to attenuate the lower frequencies whilst slightly enhancing the higher frequencies. The 20 μm aperture probe therefore exhibits a broader detection bandwidth than the 60 μm aperture probe, which exhibits a spectral response that falls off rapidly above ~0.95 THz. It is also clear from figure 3.14(a) that in contrast to the 20 μm aperture probe which has a cut-off at the edge of the spectral range of these experiments, the 60 μm signal exhibits distinctive ringing due to the cut-off behaviour of the aperture.

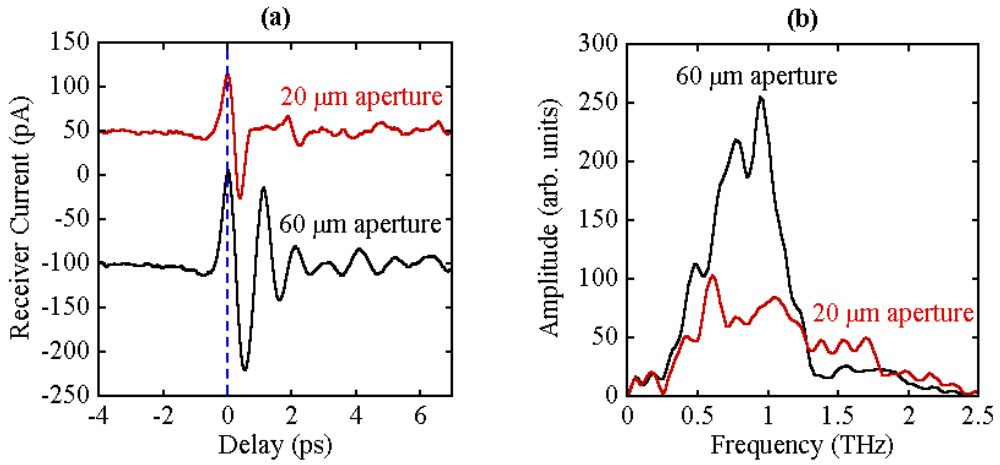

Figure 3.14. (a) Time-domain traces (vertically offset for clarity) and (b) spectra obtained using the 10 μm dipole near-field probes with 20 μm aperture (red) and 60 μm aperture (black). The vertical blue dashed line corresponds to the fixed time delay used to determine the probe resolution (described in the text).

In order to assess device resolution, the probes were scanned across a straight metal (~200 nm Au) edge deposited on high-resistivity silicon. The sample was located beyond the focus of a plano-cylindrical silicon lens and scans were taken along the long axis of the focus and with the edge oriented both parallel and perpendicular to the incident terahertz electric field. In each case, the probe-sample separation was calibrated using the timing delay associated with a terahertz reflection between the probe and sample. The probe-sample parallelism

was set in a similar fashion, by moving the probe about a triangle of points and adjusting the sample angle until the optical reflection timing delay at different points became approximately constant. Two perpendicular cameras were also used to image the setup and check parallelism.

Figure 3.15 shows the results from two perpendicular edge scans obtained using the 10 μm dipole with 60 μm aperture. Scans were repeated for a series of probe-sample separations to ascertain the effect on resolution. In the first set of scans the edge was oriented horizontally, parallel to the incident electric field, whereas in the second set the edge was rotated by 90^{o}. In both cases the dipole arms were oriented parallel to the electric field and the probe was scanned across the sample perpendicular to the metal edge. In order to measure the probe resolution, the receiver current at fixed delay (indicated by the vertical dashed line in figure 3.14(a)) was recorded as a function of position. It is clear from figure 3.15 that the edge resolution is much poorer for the vertical orientation. This point may be explained by considering the different boundary conditions for a PEC-air interface. For the case where the electric field is parallel to the metal edge, continuity of the parallel electric field component across the interface forces the field to zero at the edge. However, when the electric field is perpendicular to the metal edge there is a discontinuity at the edge due to the accumulation of surface charge. In this case, the decay of the surface charge fields may also contribute to the measured resolution. Another possibility is that the resolution is degraded due to the excitation of SPPs on the sample surface. This latter assumption may be justified by realising that SPPs are commonly excited using metal edges oriented perpendicular to the electric field via aperture coupling [40].

For the horizontal edge scans, there is an overall degradation in imaging resolution as the probe-sample separation is increased. For example, at a probe-sample separation of ~20 μm the 10-90% resolution is ~47 μm, whereas at ~50 μm separation, the resolution is degraded by ~26 μm to ~73 μm. This degradation in resolution is approximately equal to the increase in probe-sample separation (30 μm). For the vertical scans, no such effect was observed and the resolution remained approximately constant at ~150 μm. This result indicates that scanning

over the vertical metal edge does not allow inference of the true probe resolution for the reasons discussed above.

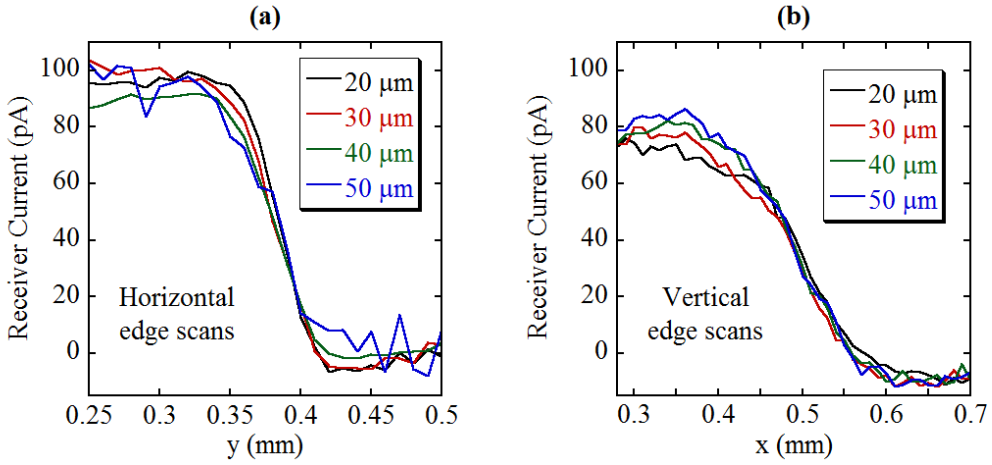

Figure 3.15. (a) Horizontal and (b) vertical edge scans obtained using the 10 µm dipole with 60 µm aperture. For various probe-sample separations indicated in the figure inset.

For comparison, figure 3.16 shows a series of horizontal and vertical edge scans obtained using the 10 µm dipole with 20 µm aperture. Interestingly, the resolution obtained using this probe is almost identical to the larger aperture probe (~45 µm at a probe-sample separation of 20 µm). This result indicates that if the aperture is large enough, the resolution is controlled by the effective dipole length. As with the larger aperture probe, for the horizontally oriented edge, the resolution was found to degrade with increasing probe-sample separation and the degradation in resolution was found to closely correspond to the increase in separation. Also, as with the larger aperture probe, the vertical edge resolution was found to be independent of the probe-sample separation, remaining constant at ~160 µm. From our results, we can infer that the probe resolution is set by the sum of the effective dipole length (or aperture diameter, whichever is smaller) and probe-sample separation. The best resolution of ~45 µm at ~20 µm separation allows an effective dipole length of ~25 µm to be inferred.

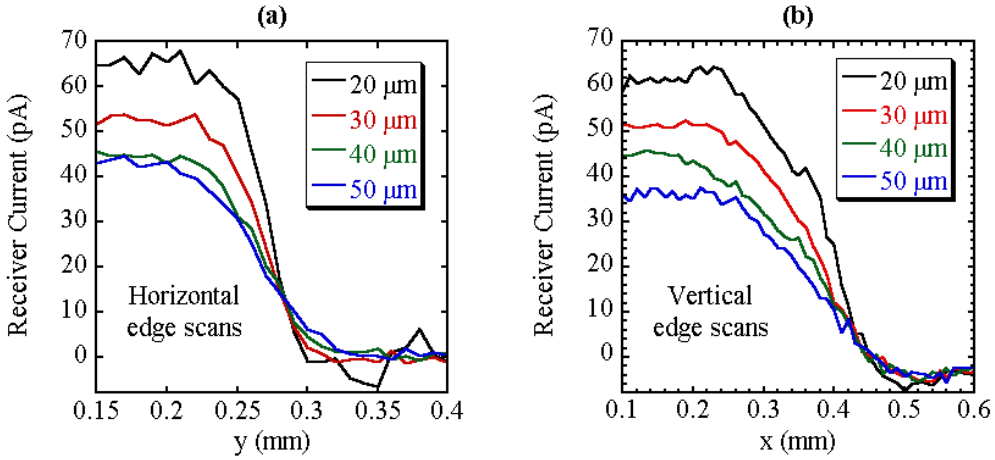

Figure 3.16. (a) Horizontal and (b) vertical edge scans obtained using the 10 µm dipole with 20 µm aperture. For various probe-sample separations indicated in the figure inset.

3.7. Summary

In summary, a novel HC-PCF-coupled TTDS system based on photoconducting antennas was constructed to enable broadband terahertz generation and detection up to ~2.2 THz, in a wide variety of experimental geometries discussed throughout the remainder of this thesis. The bandwidth and dynamic range (~$2x10^5$) of our system compares favourably to both the commercial fibre based spectrometer distributed by Picometrix and other fibre-based systems described in the literature. The use of HC-PCFs increases the power available for terahertz generation and detection and removes the need for separate second-order dispersion compensation, making the system more compact and less prone to drift. The extension of the system to include a near-field arm for evanescent field characterisation was also discussed and preliminary results were presented. The best resolution of ~45 µm was obtained by scanning a 10 µm dipole across a horizontal metal edge at ~20 µm probe-sample separation, indicating a spatial resolution of ~$\lambda/7$. Our results show that the probe resolution is independent of aperture size and decreases with increasing probe-sample separation.

References

[1] D. H. Auston, K. P. Cheung and P. R. Smith. *Picosecond photoconducting Hertzian dipoles*. Appl. Phys. Lett. **45**(3), 284-286 (1984).

[2] C. Fattinger and D. Grischkowsky. *Terahertz beams*. Appl. Phys. Lett. **54**(6), 490-492 (1988).

[3] P. R. Smith, D. H. Auston and M. C. Nuss. *Subpicosecond photoconducting dipole antennas.* IEEE J. Quant. Electron. **24**, 255-260 (1988).

[4] M. van Exter and D. Grischkowsky. *Characterization of an optoelectronic terahertz beam system.* IEEE Trans. Microwave Theory Tech. **38**, 1684-1691 (1990).

[5] Q. Wu and X. C. Zhang. *Free-space electro-optic sampling of terahertz beams.* Appl. Phys. Lett. **67**(24), 3523-3525 (1995).

[6] N. Katzenellenbogen and D. Grischkowsky. *Efficient generation of 380 fs pulses of THz radiation by ultrafast laser pulse excitation of a biased metal-semiconductor interface.* Appl. Phys. Lett. **58**(3), 222-224 (1991).

[7] J. van Rudd, D. Zimdars and M. Warmuth. *Compact, fiber-pigtailed, terahertz imaging system.* Proc. SPIE **3934**, 27-35 (2000).

[8] http://picometrix.com. Picometrix T-2000.

[9] S. A. Crooker. *Fiber-coupled antennas for ultrafast coherent terahertz spectroscopy in low temperatures and high magnetic fields.* Rev. Sci. Instrum. **73**(9), 3258-3264 (2002).

[10] G. P. Agrawal. *Nonlinear fiber optics.* 4th Edition. Elsevier academic press (2007).

[11] R. Inoue, Y. Ohno and M. Tonouchi. *Development of fiber-coupled compact terahertz time-domain spectroscopy imaging head.* Jpn. J. Appl. Phys. **45**(10A), 7928-7932 (2006).

[12] Y. Lee, S. Tanaka, N. Uetake, S. Fujisaki, R. Inoue and M. Tonouchi. *Terahertz time-domain spectrometer with module heads coupled to photonic crystal fiber.* Appl. Phys. B **87**, 405-409 (2007).

[13] J. C. Knight. *Photonic crystal fibres.* Nature **424**, 847-851 (2003).

[14] R.F. Cregan, B. J. Mangan, J. C. Knight, T. A. Birks, P. St. J. Russell, P. J. Roberts and D. C. Allan. *Single-mode photonic band gap guidance of light in air.* Science **285**, 1537-1539 (1999).

[15] F. Luan, J. C. Knight, P. St. J. Russell, S. Campbell, D. Xiao, D. T. Reid, B. J. Mangan, D. P. Williams and P. J. Roberts. *Femtosecond soliton pulse delivery at 800 nm wavelength in hollow-core photonic bandgap fibers.* Opt. Express **12**(5), 835-840 (2004).

[16] S. R. Andrews, A. Armitage, P.G. Huggard and A. Hussain. *Optimization of photoconducting receivers for THz spectroscopy.* Phys. Med. Biol. **47** 3705-3710 (2002).

[17] F. Hache, T.J. Driscoll, M. Cavallari and G.M. Gale. *Measurement of ultrashort pulse durations by interferometric autocorrelation: influence of various parameters.* Appl. Opt. **35**(18), 3230-3236 (1996).

[18] M. Tani, M. Herrmann and K. Sakai. *Generation and detection of terahertz pulsed radiation with photoconductive antennas and its application to imaging.* Meas. Sci. Technol. **13**, 1739-1745 (2002).

[19] L. Duvillaret, F. Garet, J. F. Roux and J-L Coutaz. *Analytical modeling and optimization of terahertz time-domain spectroscopy experiments using photoswitches as antennas.* IEEE J. Select. Topics Quant. Electron. **7**(4), 615-623 (2001).

[20] P. Uhd Jepsen, R. H. Jacobsen and S. R. Keiding. *Generation and detection of terahertz pulses from biased semiconductor antennas.* J. Opt. Soc. Am. B **13**(11), 2424-2436 (1996).

[21] M. Tani, S. Matsuura, K. Sakai and S. Nakashima. *Emission characteristics of photoconductive antennas based on low-temperature-grown GaAs and semi-insulating GaAs.* Appl. Opt. **36**(30), 7853-7859 (1997).

[22] A. Hussain and S. R. Andrews. *Dynamic range of ultrabroadband terahertz detection using GaAs photoconductors.* Appl. Phys. Lett. **88**, 143514 (2006).

[23] S. E. Ralph and D. Grischkowsky. *Trap-enhanced electric fields in semi-insulators: the role of electrical and optical carrier injection.* Appl. Phys. Lett. **59**(16), 1972-1974 (1991).

[24] D. Grischkowsky, S. Keiding, M. Van Exter and C. Fattinger. *Far-infrared time-domain spectroscopy with terahertz beams of dielectrics and semiconductors.* J. Opt. Soc. Am. B **7**(10), 2006-2015 (1990).

[25] J. A. Deibel, M. D. Escarra and D. M. Mittleman. *Photoconductive terahertz antenna with radial symmetry.* Electron. Lett. **41**(5), (2005).

[26] T-I Jeon, J. Zhang and D. Grischkowsky. *THz Sommerfeld wave propagation on a single metal wire.* Appl. Phys. Lett. **86**, 161904 (2005).

[27] A. Hussain and S. R. Andrews. *Ultrabroadband polarization analysis of terahertz pulses.* Opt. Express **16**(10), 7251-7257 (2008).

[28] J. A. Deibel, M. Escarra, N. Berndsen, K. Wang and D. M. Mittleman. *Finite-element method simulations of guided wave phenomena at terahertz frequencies.* Proc. IEEE **95**(8), 1624-1640 (2007).

[29] S. Hunsche, M. Koch, I. Brener and M. C. Nuss. *THz near-field imaging.* Opt. Commun. **150**, 22-26 (1998).

[30] O. Mitrofanov, M. Lee, J. W. P. Hsu, I. Brener, R. Harel, J. F. Federici, J. D. Wynn, L. N. Pfeiffer and K. N. West. *Collection-mode near-field imaging with 0.5-THz pulses.* IEEE J. Select. Topics Quant. Electron. **7**(4), 600-607 (2001).

[31] O. Mitrofanov, M. Lee, J. W. P. Hsu, L. N. Pfeiffer, K. W. West, J. D. Wynn and J. F. Federici. *Terahertz pulse propagation through small apertures.* Appl. Phys. Lett. **79**(7), 907-909 (2001).

[32] A. Bitzer and M. Walther. *Terahertz near-field imaging of metallic subwavelength holes and hole arrays.* Appl. Phys. Lett. **92**, 231101 (2008).

[33] M. Walther. Private communication.

[34] A. J. L. Adam, J. M. Brok, P. C. M. Planken, M. A. Seo and D. S. Kim. *THz near-field measurements of metal structures.* C. R. Physique **9**, 161-168 (2008).

[35] M. A. Seo, A. J. L. Adam, J. H. Kang, J. W. Lee, K. J. Ahn, Q. H. Park, P. C. M. Planken and D. S. Kim. *Near field imaging of terahertz focusing onto rectangular apertures.* Opt. Express **16**(25), 20484-20489 (2008).

[36] N. C. J. van der Valk and P. C. M. Planken. *Electro-optic detection of subwavelength terhertz spot sizes in the near field of a metal tip.* Appl. Phys. Lett. **81**(9), 1558-1560 (2002).

[37] K. Wang, A. Barkan and D. M. Mittleman. *Propagation effects in apertureless near-field optical antennas.* Appl. Phys. Lett. **84**(2), 305-307 (2004).

[38] H-T. Chen, R. Kersting and G. C. Cho. *Terahertz imaging with nanometer resolution.* Appl. Phys. Lett. **83**(15), 3009-3011 (2003).

[39] A. J. Huber, F. Keilmann, J. Wittborn, J. Aizpurua and R. Hillenbrand. *Terahertz near-field nanoscopy of mobile carriers in single semiconductor nanodevices.* Nano. Lett. **8**(11), 3766-3770 (2008).

[40] E. V. Alieva, G. Beitel, L. A. Kuzik, A. A. Sigarev, V. A. Yakovlev, G. N. Zhizhin, A. F. G. van der Meer and M. J. van der Wiel. *Linear and nonlinear FEL-SEW spectroscopic characterization of nanometer-thick films*. Appl. Spectrosc. **51**(4), 584-591 (1997).

4. Studies of surface plasmon polaritons on surfaces decorated with two-dimensional hole arrays

4.1. Introduction

In this chapter we present the first direct observations of terahertz SPP propagation on plasmonic metamaterials consisting of metal sheets perforated by two-dimensional arrays of square copper-lined holes. In section 4.2 the analytical theory developed by Pendry et al. [1,2] is introduced and its extension to more accurately describe the dispersive behaviour of SPP propagation on this class of metamaterial is discussed. The fabrication of samples is discussed in section 4.3, followed in section 4.4 by a description of the experimental technique. Finally, in section 4.5 experimental results are compared with theory and numerical simulations.

4.2. Analytical theory

Consider a perfect electrical conductor (PEC) slab perforated with a two-dimensional array of blind, square (a x a) holes with side a, pitch d and depth h filled with a medium of dielectric constant ε_h as shown in figure 4.1.

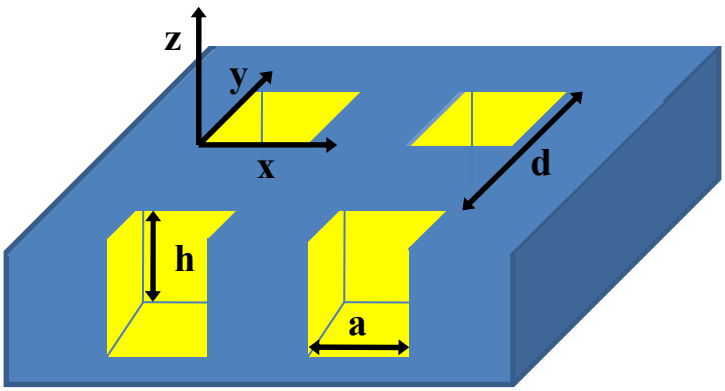

Figure 4.1. Schematic of planar two-dimensional hole array metamaterial. Blue regions correspond to PEC and the yellow regions correspond to dielectric filled holes.

In order to derive an analytical dispersion relation for this structure, the divergence in reflection of normally incident p-polarised plane waves is considered in the limit where, $a < d << \lambda_0$. In the Pendry model [1,2], expressions for the incident and reflected plane wave fields are matched to the dominant TE_{10} mode within the cavities. As the structure is periodic, Bloch boundary conditions are utilised and field matching boundary conditions are applied over a single unit cell to solve for the whole structure. The boundary conditions at the metamaterial surface (z=0) require the tangential component of the electric field E_x to be continuous over the entire unit cell ($0<x,y<d$), whereas the transverse magnetic field component H_y needs only be matched at the hole openings ($0<x,y<a$). In addition to these boundary conditions, for holes of finite depth, the condition E_x=0 must be imposed at the hole bottom (z=-h). Field matching yields an explicit relation for the specular reflection coefficient [2], the divergence of which gives the dispersion relation,

$$k_x = k_0\sqrt{1+\frac{S^4 k_0^2 Q^2}{\pi^2/a^2 - \varepsilon_h k_0^2}} \tag{4.1}$$

where k_x is the SPP wavevector along the propagation axis, $k_0 = \omega/c$, is the total wavevector in air, $S = 2\sqrt{2}a/\pi d$ is the overlap integral describing coupling between the incident plane wave and TE_{10} mode within the cavities and $Q = 1 - e^{-2|q_z|h}/1 + e^{-2|q_z|h}$ accounts for the finite depth of the holes, where q_z is the out-of-plane wavevector in the cavities. For holes of infinite depth, the specular reflection coefficient can be simplified to a form analogous with Fresnel's equation [2], allowing the metamaterial to be conceptually replaced by a homogeneous medium described by an effective dielectric function given by,

$$\varepsilon_{eff} = \frac{\varepsilon_h}{S^2}\left(1-\frac{\pi^2 c^2}{a^2 \varepsilon_h \omega^2}\right) \sim 1 - \frac{\omega_{spoof}^2}{\omega^2} \tag{4.2}$$

This simple analytical approach is based on the assumption that for the case where $a<d<<\lambda_0$, the metamaterial can be represented as a homogeneous medium with an

effective dielectric function displaying a plasma form, defined by a resonance at the spoof plasma frequency $\omega_{spoof} = \pi c / a\sqrt{\varepsilon_h}$. This is simply the cut-off frequency of an open-top cavity of side a, filled with a medium of dielectric constant ε_h. In other words, the holes act like waveguides with a cut-off frequency ω_{spoof}, below which only evanescent fields can exist within the cavities and thus SPPs can be supported.

Figure 4.2 shows the dispersion relation calculated using equation 4.1 for the set of parameters stated in the figure caption. It is evident from the figure that the simple analytical model neglects the effects of diffraction, which leads to a significant modification of the dispersion curve close to the zone boundary ($k_x=\pi/d$). In periodic air-filled hole arrays, the asymptotic region of the dispersion curve close to the spoof plasma frequency (where $k_x = \pi / a\sqrt{\varepsilon_h}$) always lies beyond the zone boundary and cannot be accessed. In order to reach this part of the dispersion curve, the holes must be filled with a higher index dielectric such that $a\sqrt{\varepsilon_h} > d$. For example, filling the holes with silicon (ε_h=12.11) lowers the spoof plasma frequency for this structure from 2 THz to ~0.57 THz (figure 4.2). In this case, the dispersion curve plateaus within the first Brillouin zone, leading to lower group velocity and tighter field confinement.

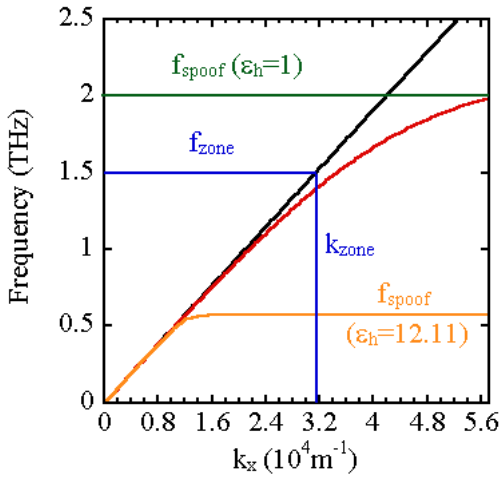

Figure 4.2. Analytical calculation of SPP dispersion along the propagation axis for a two-dimensional hole array metamaterial with parameters a= 75 μm, d= 100 μm and h= 50 μm, for ε_h=1 (red) and ε_h=12.11 (orange). The light line is plotted in black.

Figure 4.3 shows a comparison between the analytical dispersion curve calculated using equation 4.1 and that obtained from finite-difference time-domain (FDTD) numerical modelling, for a hole array with the parameter set stated in the figure caption. For the FDTD case, the structure is still modelled as a PEC but the effects of additional cavity modes and higher-order diffraction are implicitly included. As is evident from figure 4.3, the simple analytical model shows a poor agreement with numerical simulations even at small wavevector where the condition $a<d<<\lambda_0$, is satisfied.

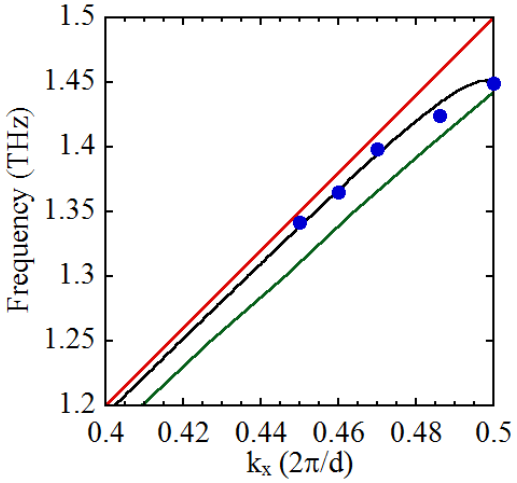

Figure 4.3. Comparison between analytical (green line), MEA calculation (black line) and numerical FDTD simulations (blue dots) of the SPP dispersion along the propagation axis for a 2d hole array with parameters a= 66 μm, d= 100 μm, h= 58 μm and ε_h=1. The light line is plotted in red. [MEA result is taken from a calculation performed by Antonio Fernández-Domínguez].

This point was originally highlighted by García de Abajo and Sáenz [3] for infinitely deep holes and attributed to the non-local response of the metamaterial (i.e. $\varepsilon_{eff}(\omega) \rightarrow \varepsilon_{eff}(\omega,\underline{k})$). In their work, numerical simulations were used to show that the inclusion of higher-order cavity modes within the defects led to significant reshaping of the SPP dispersion relation, not only close to the zone boundary (where the condition $a<d<<\lambda_0$ breaks down), but also at small wavevector, where the low-frequency portion of the SPP dispersion curve is shifted closer to the light line. The important finding of this work, is that even well away from the zone boundary, where $a<d<<\lambda_0$, the metamaterial cannot be

accurately described as an homogeneous effective medium with effective dielectric function $\varepsilon_{eff}(\omega)$.

In this work, a model in which the effects of both additional cavity modes and higher-order diffraction are included for finite depth holes was developed by colleagues at the Universidad Autónoma de Madrid and Universidad de Zaragoza-CSIC [4]. The model is a modal expansion approximation (MEA) in which the number of cavity modes and diffraction orders considered in the calculation were chosen to provide sufficient convergence. As can be seen from figure 4.3 the MEA is in much closer agreement with FDTD simulations than the simple analytical model. More recently, the MEA approach was independently described by Hendry et al. [5] and validated by comparison with microwave measurements of the dispersion of a wax-filled tube array [6].

4.3. Sample fabrication

Two different hole-array samples were fabricated by copper plating lithographically patterned polymer films. A thin layer of SU8-5, an epoxy-based negative photoresist, was initially spun on to a silicon wafer to create a base layer and exposed to UV light to render it inert. A 60-μm-thick layer of SU8-50 photoresist was then applied and contact optical lithography was used to pattern the surfaces with two-dimensional square arrays of holes. Copper was deposited onto the cured SU8 surfaces by electroless catalytic plating using the Shipley Circuposit^{TM} process [7].

Plating consisted of four distinct stages. In the first, the sample was treated with an alkaline conditioner solution to promote even surface coverage. An acidic pre-dip treatment was then used to clean the sample surfaces. The samples were then immersed in a colloidal palladium-tin catalyst at 40 ^{o}C for ~5 minutes. Finally, the samples were transferred to a low-build copper plating solution for ~30 minutes, providing a dense fine-grain surface finish. In this final stage, agitation at 40 Hz was found to significantly improve uniformity by preventing the formation of

hydrogen bubbles that otherwise produced defects. Samples were then rinsed in deionised water, soaked in isopropanol and blow dried.

Sample I was fabricated with a period d= 150 μm and hole edge a= (91±5) μm, and sample II with d= 100 μm and a= (66±4) μm. Scanning electron microscope (SEM) images of sample I are shown in figure 4.4.

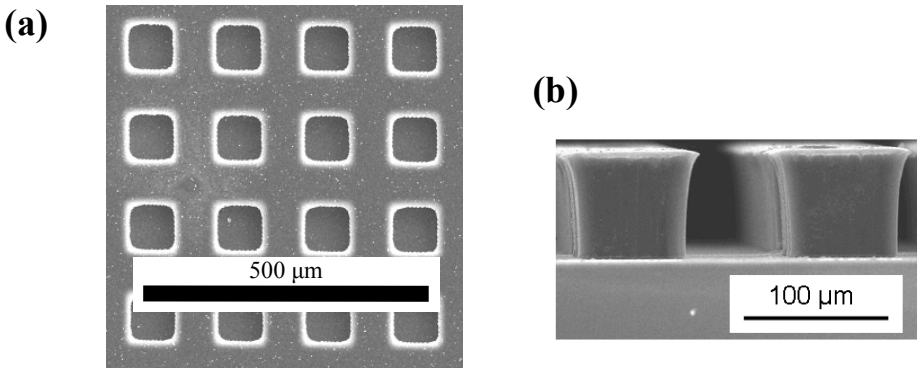

Figure 4.4. (a-b) SEM images of metamaterial sample I. (b) shows a cross section of the structure.

The hole depth in each sample was measured to be h= (58±6) μm, and the copper thickness was ~0.5 μm. The uncertainties in the sample parameters reflect systematic variations across the sample surfaces associated with spin-coating and the existence of undercut in the hole side-walls (see figure 4.4). The patterned area was 35 mm long and 6 mm wide.

4.4. Experimental arrangement

Experiments were carried out using the SI-GaAs coplanar photoconducting transmitter and 10 μm arsenic-implanted dipole receiver described in section 3.4. As discussed in chapter 2, because of the evanescent character of SPPs, the in-plane wavevector is always greater than that of light in free-space ($k_x > k_0$) and coupling light into SPPs requires a scheme for phase matching. In this work

broadband coupling of the p-polarised free-space radiation into SPPs was achieved by focussing the terahertz beam onto a wavelength-scale aperture defined by the gap between the sample and the edge of a stainless steel razor blade oriented perpendicular to the sample plane [8]. In this scheme, diffraction at the aperture provides larger wavevector components parallel to the surface, allowing a small fraction of the incident radiation to couple into SPPs [9]. The 1/e diameter of the THz beam at the in-coupling aperture was estimated to be ~2 mm at 1 THz.

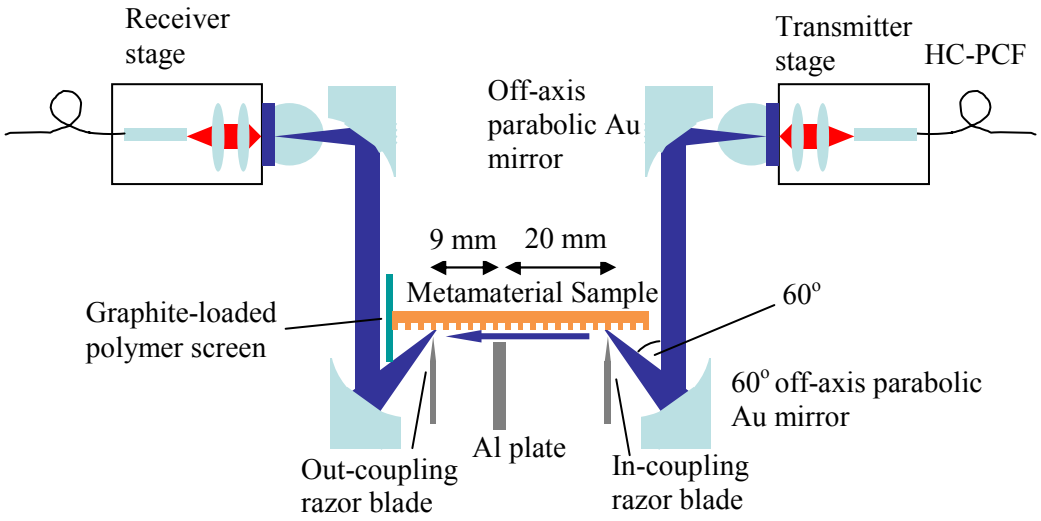

Figure 4.5. Schematic diagram of the experimental coupling apparatus.

The small sample width perpendicular to the SPP propagation direction was found to have no affect on our results as long as the centre of the incident terahertz beam was positioned to within ± 2 mm of the long central axis of the sample. A terahertz absorbing, graphite-loaded polymer screen was positioned to prevent radiation scattered from the end of the sample from reaching the receiver. Without this screen, contributions from the razor blade out-coupler and sample edge would be difficult to separate due to the small delay between them. The in-coupling (h_1) and out-coupling (h_2) aperture heights were experimentally chosen to maximize the SPP signal amplitude. For experiments on sample I the aperture heights were set to ~200±10 μm and for sample II they were fixed at ~100±10 μm. For coupling to plane copper surfaces the aperture heights were set to ~300±10 μm. In these experiments a total amplitude in-coupling and out-coupling efficiency of ~1% was estimated for both metamaterial samples by comparison with a free-

space reference signal obtained by passing the coupling apparatus. This value is in good agreement with previous measurements [8].

An intermediate aperture (h_3), made from a 1.5-mm-thick aluminium sheet was used to probe the extent of the SPP field perpendicular to the sample surface and diffraction at the final razor blade (aperture h_2) was used to transform the SPP back into free-space radiation for detection. The SPP signal was small but finite when h_3 was nominally zero due to a slight curvature of the sample surfaces attributed to the non-uniform spin-coating process.

It is important to appreciate that the propagation distance, after excitation, for the modal shape of the surface wave to fully develop is governed by the out-of-plane amplitude decay length, L_{zd}. This point was mentioned by Jeon and Grischkowsky [10] for SPP propagation along smooth copper surfaces and is consistent with the idea of a finite interaction length (chapter 2). To reach its fully evolved form, the SPP must propagate several out-of-plane decay lengths, as confirmed by the numerical finite-integration technique (FIT) simulations described in section 4.5. For a flat copper sheet at 1 THz, L_{zd}~6 cm, making observations of fully-developed Zenneck waves on flat surfaces difficult. This explains the large discrepancy between theoretical and experimental measurements of Zenneck waves reported to date [10]. In the metamaterial case however, L_{zd} is reduced to a few millimetres or less over a large frequency range near the band edge (verified using FIT simulations as described in section 4.5), implying that the SPP waves have fully developed before reaching the intermediate aperture, h_3.

4.5. Results

Figures 4.6 and 4.7 show time-domain signals and spectra obtained after propagating 29 mm along the two metamaterial samples for two different probing heights, h_3=200 μm and h_3=1000 μm. For comparison, the signal obtained for propagation on a 29 mm long smooth copper surface (the unevolved Zenneck wave) is also shown in figure 4.8.

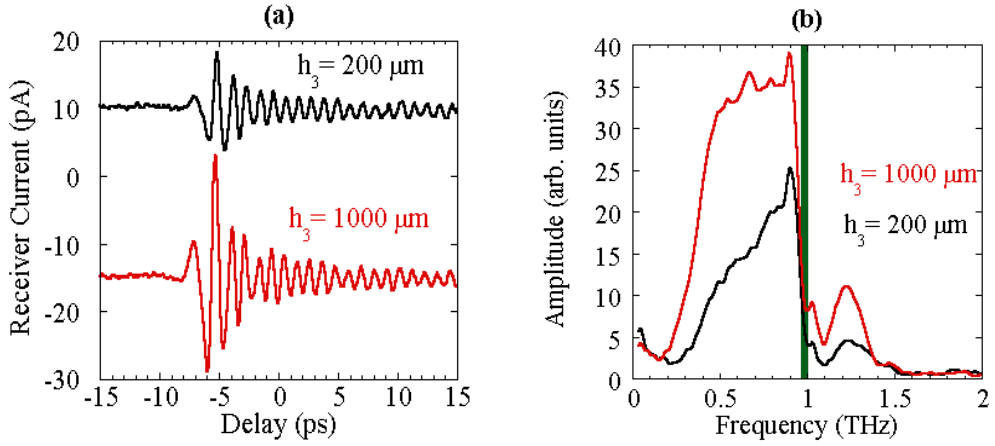

Figure 4.6. (a) Time-domain traces and (b) spectra obtained for sample I. The vertical green line corresponds to the zone boundary f_{zone}=(0.98±0.02) THz obtained from FDTD simulations.

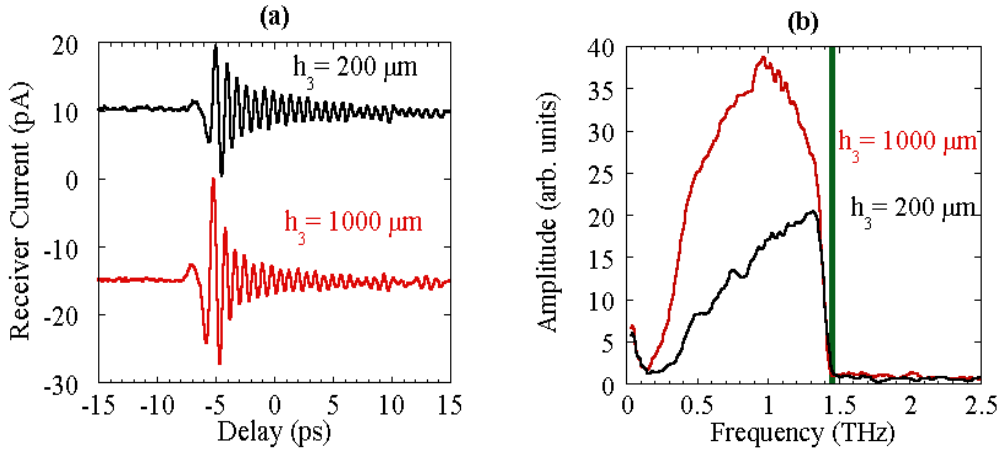

Figure 4.7. (a) Time-domain traces and (b) spectra obtained for sample II. The vertical green line corresponds to the zone boundary f_{zone}=(1.45±0.02) THz obtained from FDTD simulations.

The time-domain trace for propagation along the smooth copper surface (figure 4.8) is similar to that obtained for free-space propagation (figure 4.9). Because of the extremely low dispersion of the Zenneck wave on a flat surface, the small change in shape is mainly due to the filtering effect of the apertures. In contrast, the signals obtained from the two metamaterial samples show pronounced ringing, which persists for more than 10 ps and the corresponding spectra exhibit a sharp cut-off close to the Brillouin zone boundary (indicated by the vertical lines in

figures 4.6(b) and 4.7(b)). In this case, the position of the zone boundary is calculated from FDTD simulations. The uncertainty in the zone boundary frequencies reflect uncertainty in the values of the structural parameters *a* and *h* as discussed in section 4.3. For air-filled holes, the TE_{10} spoof plasma frequencies lie at ~1.65 THz and ~2.27 THz for samples I and II respectively and cannot be accessed for the reasons described earlier.

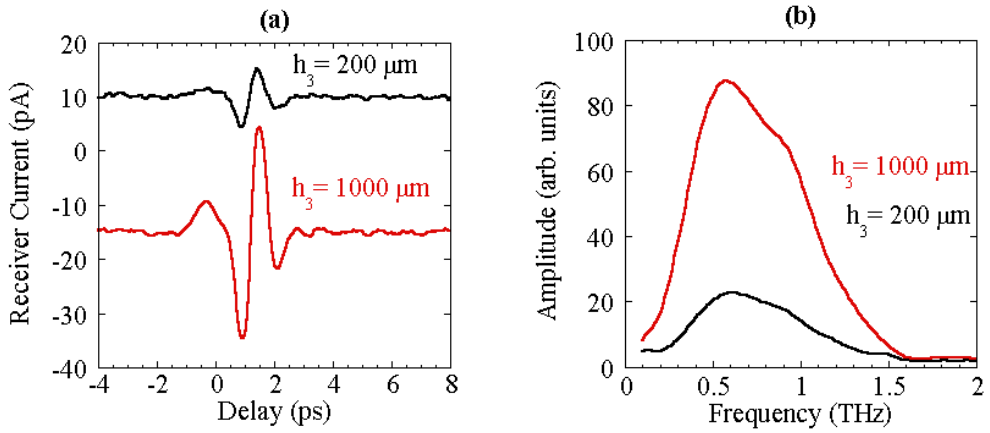

Figure 4.8. (a) Time-domain traces and (b) spectra obtained for SPP propagation on a flat copper sheet.

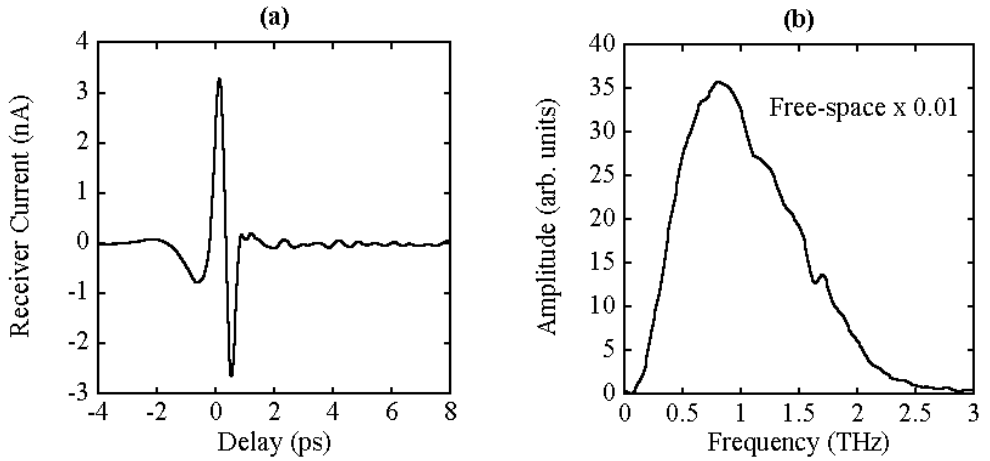

Figure 4.9. (a) Time-domain trace and (b) spectra obtained from a free-space reference signal by-passing the coupling apparatus.

In order to probe the SPP out-of-plane field confinement, the height of the intermediate aperture, h_3, was varied. By assuming that the effect of this aperture is simply to pass part of the incident SPP without significantly altering its field

distribution, then the effect is to integrate the Poynting vector parallel to the surface. In this case, energy conservation requires that the ratio of the transmitted (A_2) and incident (A_1) field amplitudes on either side of the aperture is given by,

$$A_2(\omega)/A_1(\omega) = \sqrt{1-\exp(-2k_{zd}h_3)} \tag{4.3}$$

Because the detected field after out-coupling, $E_2(\omega)$, is proportional to $A_2(\omega)$, this implies that k_{zd} can in principle be determined from the variation of $E_2(\omega)$ with h_3. To test the above assumptions, numerical finite integration technique (FIT) simulations of the SPP propagation along our samples were undertaken with the metal modelled as a PEC. Figure 4.10 shows the distribution of the electric field evaluated in the x–z plane of sample II, for three different values of h_3. The aperture dimensions and positions are the same as in the experiment, except for the position of the output coupler which is located beyond the right-hand edge of the figure and is not shown. The frequency of the incident radiation (1.3 THz) is chosen to be close to the zone boundary, where large confinement of the SPP is expected. It is clear from these results that the intermediate aperture selectively passes the SPP whilst blocking unwanted radiation diffracted at the input coupler. Note also that the SPP has fully evolved after propagating ~5 mm.

Figure 4.11(a) shows the out-of-plane decay of the fields extracted from the FIT simulation at several points along the x-axis, allowing comparison of the field confinement within and after the intermediate aperture. It is clear from this figure that the field profile is approximately maintained during the transmission process and that the out-of-plane decay of the SPP closely corresponds to that calculated from the MEA.

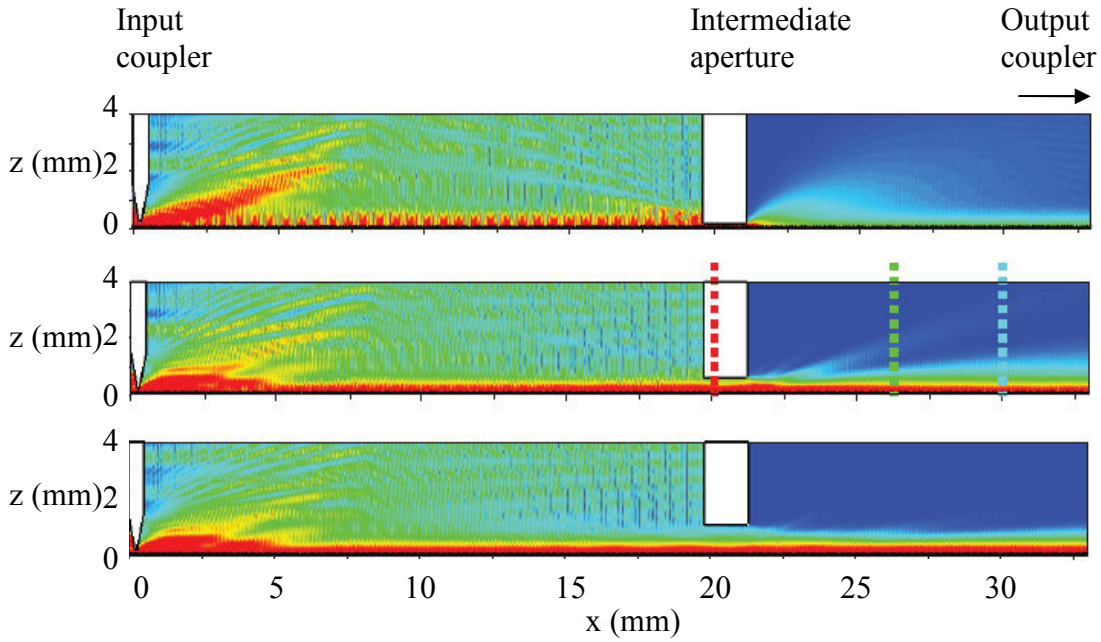

Figure 4.10. Simulated absolute electric-field maps for SPP propagation along sample II at a frequency of 1.3 THz for (from top to bottom) h_3=0.1 mm, h_3=0.5 mm and h_3=1.0 mm. Red represents high fields, descending through yellow and green to sky blue. Dark blue regions correspond to zero field. Dashed lines correspond to the positions of the z-cuts plotted in figure 4.11(a). [From an FIT simulation carried out by Antonio Fernández-Domínguez].

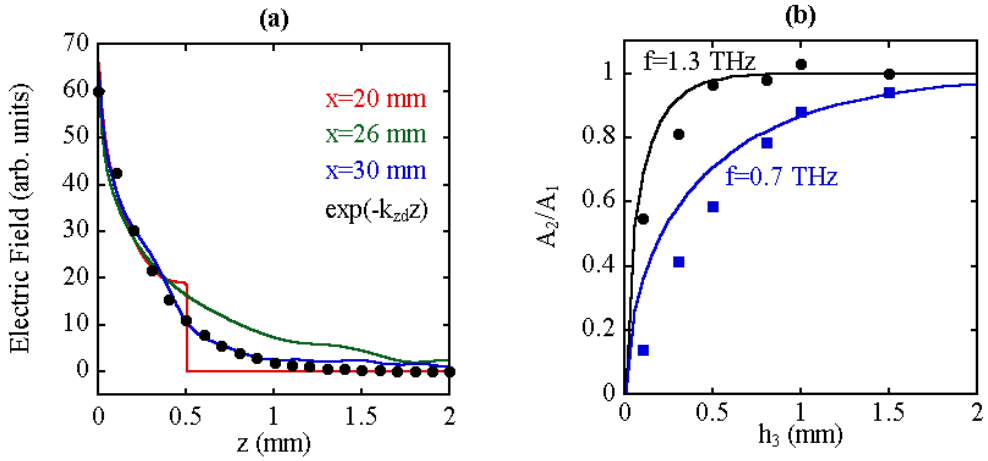

Figure 4.11. (a) Comparison between the SPP electric field profile obtained from FIT simulations at different propagation distances and that predicted using k_{zd} from the MEA calculation (points). (b) Ratio A_2/A_1 as a function of probing height on sample II at two different frequencies, 0.7 THz (blue) and 1.3 THz (black). Lines correspond to equation 4.3 evaluated using the MEA and the points to the FIT predictions. [FIT results are extracted from a simulation carried out by Antonio Fernández-Domínguez].

In order to verify that the dependence of the output signal amplitude on h_3 allows determination of k_{zd}, the ratio A_2/A_1 obtained using the FIT simulations was compared with that evaluated using equation 4.3 with k_{zd} taken from the MEA calculations (figure 4.11(b)). The good agreement between the FIT result, which includes diffraction at the intermediate aperture, and the MEA predictions, which neglect it, demonstrates the experiments ability to probe the confinement of the SPP propagating at the surface of the metamaterial. This is true for h_3 greater than or of order the free-space wavelength, but for smaller h_3, the FIT aperture transmission is less than predicted by the MEA due to diffraction.

The experimental variation of $E_2(\omega)$ with h_3 for the two samples is shown in figure 4.12, which also shows theoretical predictions calculated using equation 4.3 with k_{zd} evaluated from the MEA. The theoretical bands are scaled vertically to fit the data and the theoretical values for L_{zd} are included in each figure.

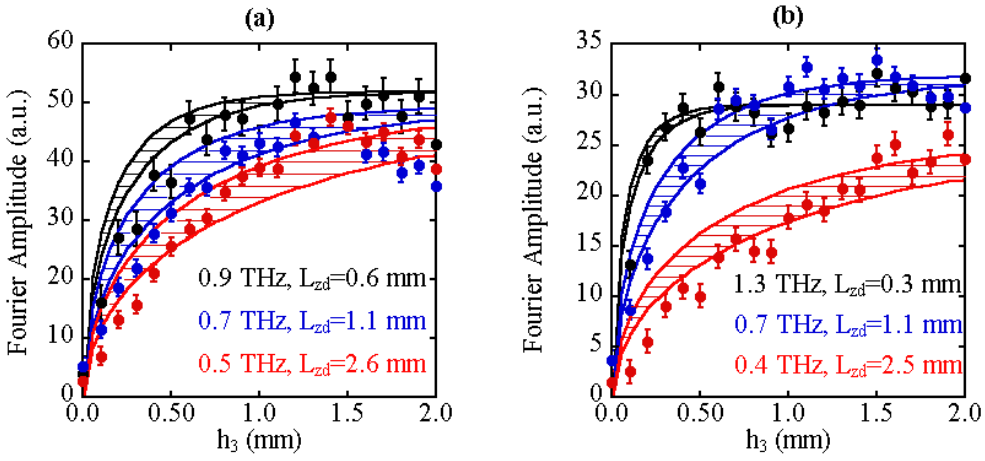

Figure 4.12. Experimental (points) and theoretical (bands) electric-field amplitudes as a function of h_3 for (a) Sample I and (b) Sample II. The error bars denote uncertainties in the experimental measurement and the theoretical curves are represented as shaded bands to reflect the uncertainty in geometrical sample parameters evaluated from equation 4.3 using the MEA. The out-of plane decay lengths calculated using the MEA are also displayed.

As is evident from figure 4.12, the agreement between theory and the measured amplitudes appears very good, particularly for the higher frequencies where the confinement is strongest and diffraction is weakest and for aperture heights

greater than the free-space wavelength. A fitting of the complete data sets (including the smallest aperture heights) to equation 4.3 overestimates the decay length by a factor of order two for the reasons discussed. For signal-to-noise reasons it was not possible to restrict the fitted data to large h_3. A more accurate experimental determination of L_{zd} requires either a near-field probing scheme avoiding diffraction (chapter 3) or an analytical treatment that takes aperture diffraction into account. It is however clear that wavelength scale field confinement is observed over a wide frequency range near the band edge and that the degree of confinement is in close agreement with theory when account is taken of the approximations inherent in equation 4.3.

Due to restrictions in the experimental geometry, the SPP propagation loss was not directly measured in these experiments. Therefore, in order to estimate the attenuation lengths, separate FIT simulations were carried out in which the metal was modelled as a lossy conductor with $\sigma_0 = 5.8 \times 10^7\ \Omega^{-1}m^{-1}$. The same calculation was also repeated with the metal modelled as a PEC to quantify the diffractive and Ohmic loss contributions.

In order to estimate the amplitude attenuation, the modulus of the FIT time-domain waveforms were integrated at different propagation lengths, as shown for sample II in Figure 4.13(a). The solid lines represent exponential fits to the data. For the PEC case, the amplitude attenuation was estimated to be 0.08 cm^{-1} whereas in the lossy conductor case the value increased to 0.11 cm^{-1}. From these results it is possible to estimate the Ohmic loss contribution as 0.03 cm^{-1}.

The combination of this result with the out-of-plane decay lengths calculated from the MEA (figure 4.13(b)) clearly demonstrate that for these samples there is a tolerable trade-off between loss and confinement, with wavelength-scale field confinement observed at the band edge and confinement of order two free-space wavelengths observed down to ~0.1 THz.

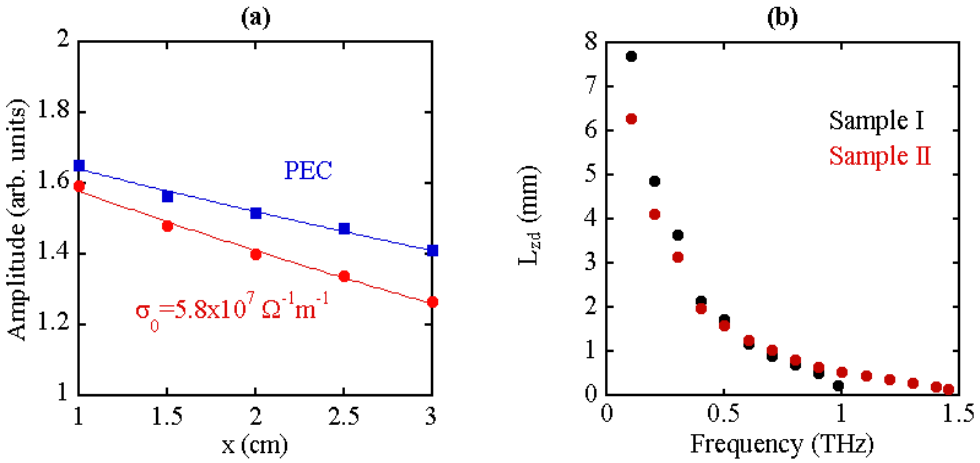

Figure 4.13. (a) SPP amplitude calculated from FIT calculation (points) for various propagation lengths along sample II. Lines represent exponential fits to the data. (b) out-of-plane decay length L_{zd} calculated using the MEA for both metamaterial samples.

Due to the small signal amplitudes and lack of an exact reference signal in the aperture coupling geometry discussed so far, no reliable phase information could be extracted from the experimental data sets. To analyse the phase data, a more efficient end-fire coupling scheme (described in chapter 5) was later utilised to dramatically improve the signal strengths. Reference signals were obtained with the sample removed and used to calibrate the position of the light line. In this case, by extracting the phase difference ($\Delta\varphi$) between the SPP and reference signals, the wavevector shift can be calculated as a function of frequency using the expression,

$$\Delta k = k_x - k_0 = \frac{\Delta\varphi}{L_{SPP}} \tag{4.4}$$

where L_{SPP} is the SPP propagation length. Figure 4.14 shows a comparison between the experimentally extracted phase data and that obtained directly from the MEA. It is clear that for both samples the experimental results show reasonable agreement with the MEA over a large frequency range.

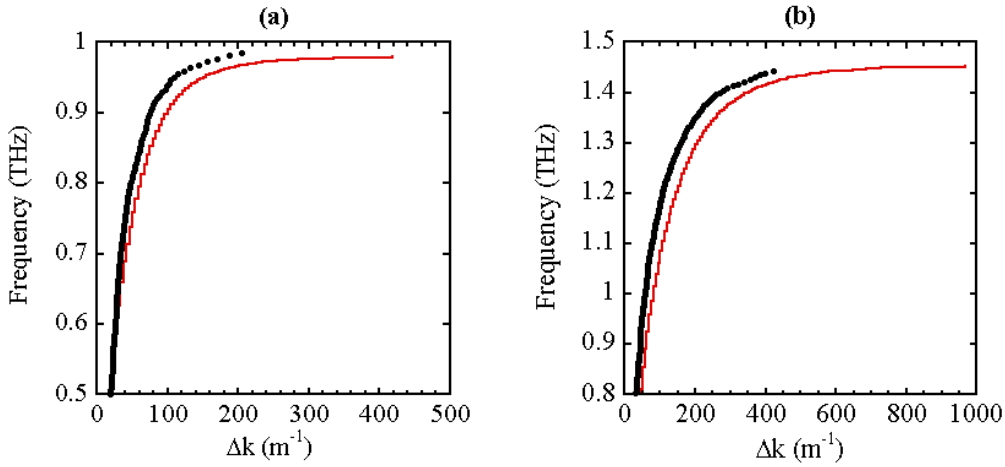

Figure 4.14. Dispersion curves for SPP propagation along (a) sample I and (b) sample II. Black points correspond to experimental values and the red lines correspond to values extracted from the MEA calculation.

We estimate, from repeated measurements, that the maximum error in Δk is <10% at the lowest frequencies, decreasing to <5% where the curves begin to plateau. The discrepancy between theory and experiment can be explained by appreciating that the value of L_{SPP}=35 mm used to evaluate equation 4.4 is overestimated due to the non-zero SPP interaction length (chapter 2). As it takes the SPP a few mm to evolve, the effective value for L_{SPP} is correspondingly reduced and depends on frequency. The uncertainty in structural parameters also leads to an error of ~2% in the frequencies of the analytical calculation, which accounts for the disagreement at high frequency. Figure 4.14 shows that the largest values of Δk are not measured in the experiment. This can be explained by appreciating that the tightly bound fields in the immediate vicinity of the zone boundary are not detected due to a combination of increased attenuation and dispersion-induced temporal broadening. In the case of sample II, it is also possible that the largest wavevectors are only weakly excited in the experiment due to the poorer modal overlap with the source.

The wavelength scale SPP confinement observed for the air-filled hole arrays discussed so far is dominated by diffraction induced bending of the TE_{10}

dispersion curve at the band edge, rather than the proximity to the spoof plasma frequency. In order to investigate the effect of removing periodicity, two structures consisting of random arrangements of holes were fabricated using the technique described in chapter 5 and investigated using the end-fire coupling technique. The first consisted of holes with side a=25±1 μm and the second of holes with side a=50±1 μm, both samples had hole depth h=60±5 μm. By fabricating the random hole arrays with such small dimensions, the spoof plasma frequency was pushed well beyond the spectral range of our experiments so as to remove any confinement mechanism. No restriction was placed on the minimum hole separation in these samples so that quasi-periodicity was avoided. For this reason, some regions of the sample contained large aggregates of holes, the net-effect of which is to weight the spectral response of the samples to lower frequencies. Figure 4.15 shows the time-domain and frequency data for these samples. Also plotted is a reference signal obtained by removing the sample and keeping the lens separation fixed.

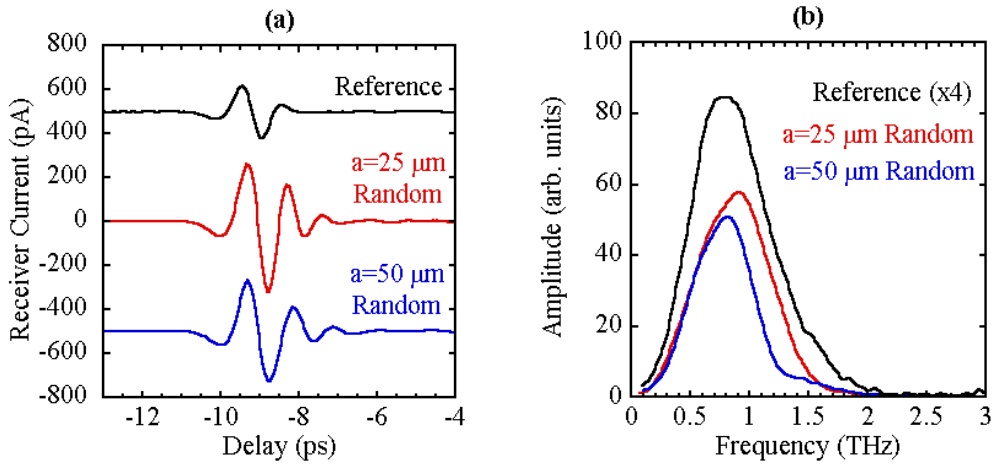

Figure 4.15. (a) Time-domain traces and (b) spectra obtained for propagation along the random metamaterial samples.

We believe that we are recording the guidance of radiation along the samples due to the factor of ~2 increase in signal strength obtained with the sample, as well as the reshaping of the time-domain traces depicted in figure 4.15(a). The ~200 pA signal strength is very similar to that obtained on a bare copper sheet (~170 pA) using the same coupling technique. The relative coupling efficiency for these

samples is somewhat lower than for the periodic structures (~500 pA). This can be explained by the much poorer modal field overlap with the source. The spectra in figure 4.15(b) clearly show that the smaller hole array sample is weighted towards higher frequency and that both samples exhibit relatively broadband featureless spectra. The first point can be understood by appreciating that aggregation is more pronounced in the larger hole sample and hence the effect of the cavities is larger. A logical extension to this part of the work would be to investigate larger hole sizes where the spoof plasma frequency can be lowered. For example, a 100 μm hole size would exhibit a spoof plasma frequency close to 1.5 THz. In this case it should be possible to more tightly confine radiation to the sample whilst preserving the broadband propagation character demonstrated in figure 4.15(b).

4.6. Summary

In summary, field confinement on the order of the free-space wavelength has been experimentally observed over a large frequency range, on two planar metamaterial samples consisting of two-dimensional arrays of copper-lined holes. This degree of confinement represents more than a two orders of magnitude increase compared to a flat metal sheet over the same frequency range. The good agreement between numerical simulations, analytical theory and experimental results suggest that for these samples the condition $d,a << \lambda$ assumed in the metamaterial concept is in practice quite relaxed. From FIT simulations, the amplitude attenuation coefficient was estimated to be 0.11 cm^{-1}, reflecting a tolerable trade-off between loss and confinement. These characteristics are encouraging for potential applications in terahertz waveguiding as well as in chemical or biochemical sensing. The vertical confinement and hence field enhancement could be further increased by filling the holes with a high-index dielectric such as silicon, so as to lower the spoof plasma frequency below the band edge. In this case however, the guidance bandwidth would be significantly reduced. It is also anticipated that by switching from two-dimensional arrays of cavities to laterally graded hole arrays [11], that significant lateral confinement may be realised in the future. Subsequent work by Zhu et al. [12] has shown that

waveguiding on metal sheets pierced with one-dimensional arrays of bottomless rectangular slits can yield lateral confinement of order two wavelengths. It can therefore be anticipated that linear chains of blind holes may provide a similar degree of lateral confinement. Results for SPP propagation on two random metamaterial samples were also presented, where it was shown that the removal of periodicity leads to poor field confinement due to the fact that the waveguide cut-offs lie beyond the spectral range of the experiment. In this case, it is anticipated that larger hole samples would lead to increased confinement by bringing the TE_{10} cut-off into the spectral range of the experiment, whilst preserving the broadband propagation characteristic.

References

[1] J. B. Pendry, L. Martín-Moreno and F. J. Garcia-Vidal. *Mimicking surface plasmons with structured surfaces.* Science **305**, 847-848 (2004).

[2] F. J. Garcia-Vidal, L. Martín-Moreno and J. B. Pendry. *Surfaces with holes in them: new plasmonic metamaterials.* J. Opt. A: Pure Appl. Opt. **7**, 97-101 (2005).

[3] F. J. García de Abajo and J. J. Sáenz. *Electromagnetic surface modes in structured perfect-conductor surfaces.* Phys. Rev. Lett. **95**, 233901 (2005).

[4] C. R. Williams, S. R. Andrews, S. A. Maier, A. I. Fernández-Domínguez, L. Martín-Moreno and F. J. García-Vidal. *Highly confined guiding of terahertz surface plasmon-polaritons on structured metal surfaces.* Nat. Photonics **2**, 175-179 (2008).

[5] E. Hendry, A. P. Hibbins and J. R. Sambles. *Importance of diffraction in determining the dispersion of designer surface plasmons.* Phys. Rev. B **78**, 235426 (2008).

[6] A. P. Hibbins, E. Hendry, M. J. Lockyear and J. R. Sambles. *Prism coupling to 'designer' surface plasmons.* Opt. Express **16**(25), 20441-20447 (2008).

[7] http://rohmhaas.com. Circuposit plating process.

[8] E. V. Alieva, G. Beitel, L. A. Kuzik, A. A. Sigarev, V. A. Yakovlev, G. N. Zhizhin, A. F. G. van der Meer and M. J. van der Wiel. *Linear and nonlinear FEL-SEW spectroscopic characterization of nanometer-thick films.* Appl. Spectrosc. **51**(4), 584-591 (1997).

[9] J. Saxler, J. Gómez Rivas, C. Janke, H. P. M. Pellemans, P. Haring Bolívar and H. Kurz. *Time-domain measurements of surface plasmon polaritons in the terahertz frequency range.* Phys. Rev. B **69**, 155427 (2004).

[10] T-I. Jeon and D. Grischkowsky. *THz Zenneck surface wave (THz surface plasmon) propagation on a metal sheet.* Appl. Phys. Lett. **88**, 061113 (2006).

[11] S. A. Maier and S. R. Andrews. *Terahertz pulse propagation using plasmon-polariton-like surface modes on structured conductive surfaces.* Appl. Phys. Lett. **88**, 251120 (2006).

[12] W. Zhu, A. Agrawal and A. Nahata. *Planar plasmonic terahertz guided-wave devices.* Opt. Express **16**(9), 6216-6226 (2008).

5. Studies of surface plasmon polaritons on coaxial hole arrays

5.1. Introduction

The ability to confine radiation at two or more frequencies is important for sensing. In order to reliably distinguish between the absorption spectra of two different materials, which may increase monotonically with frequency or display specific resonances, the ability to ratio data at several frequencies is essential. It is well known that coaxial structures can support a variety of guided modes in transmission, including a TEM mode where the field extends radially from the central pillar [1]. The bandpass characteristics of arrays of such structures have been analysed and experimentally investigated within the context of frequency selective surfaces [2,3] as well as being explored within the field of enhanced transmission [4,5,6]. To our knowledge, no waveguiding studies on surfaces structured with arrays of coaxial apertures have been reported to date.

In this chapter we report terahertz SPP waveguiding on metamaterials consisting of two-dimensional arrays of 'blind' annular apertures. We start in section 5.2 by describing FDTD simulations which show the presence of two distinct spoof plasmonic modes below the light line. An analytical model based on a modal expansion calculation is shown to provide close agreement with FDTD simulations, providing physical insight into the electromagnetic character of these geometric resonances. Sample fabrication is described in section 5.3. In section 5.4 the experimental setup is described and experimental results are analysed and compared with the analytical calculation.

5.2. Simulations

FDTD simulations were used to identify the presence of two spoof plasmonic modes in the blind coaxial structure depicted in figure 5.1. The structure was

modelled as a PEC and Maxwell's equations were solved over a single unit cell by implementing periodic boundary conditions.

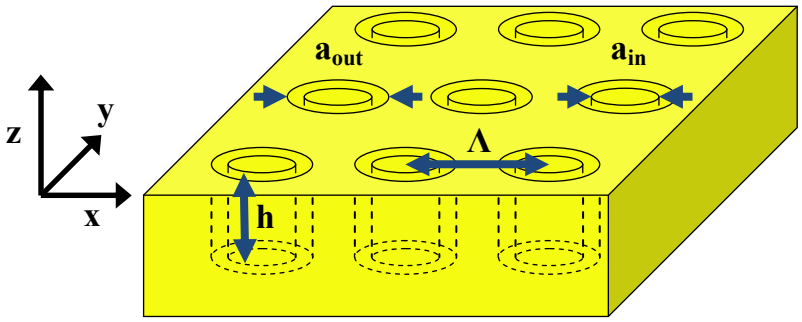

Figure 5.1. Schematic of coaxial metamaterial structure, consisting of cylindrical air-filled cavities of diameter a_{out} and depth h in a metal sheet, with cylindrical metal pillars of diameter a_{in} coaxially inserted into them.

The calculated dispersion curve is shown in figure 5.2. It is clear that the coaxial structure supports two spoof plasmonic modes that lie below the light line. For the set of structural parameters indicated in the figure caption, the two band edges are located at 1.06 THz and 1.79 THz respectively. The lowest frequency TEM-like mode is bound to the central pillar, however, unlike a true TEM mode it displays a wavevector cut-off at the zone boundary. The shape of the TEM-like dispersion curve, which plateaus at large wavevectors, reflects an effective spoof plasma frequency at ~1.06 THz whereas the higher frequency cut-off is simply due to diffraction of the TE_{11} dispersion curve. This mode would still be supported if the central pillar were removed. The FDTD simulation also allows evaluation of the field confinement at the two band edges, indicating that the fields at the TEM-like cut-off are bound to within ~λ/9 (~31 μm) of the sample surface, corresponding to a five-fold field enhancement with respect to the fields close to the TE_{11} cut-off, which are bound to within ~λ/2 (~86 μm) (figure 5.2). This additional confinement is particularly attractive in terms of sensing, as the structures are air-filled and access to the bound fields is unrestricted.

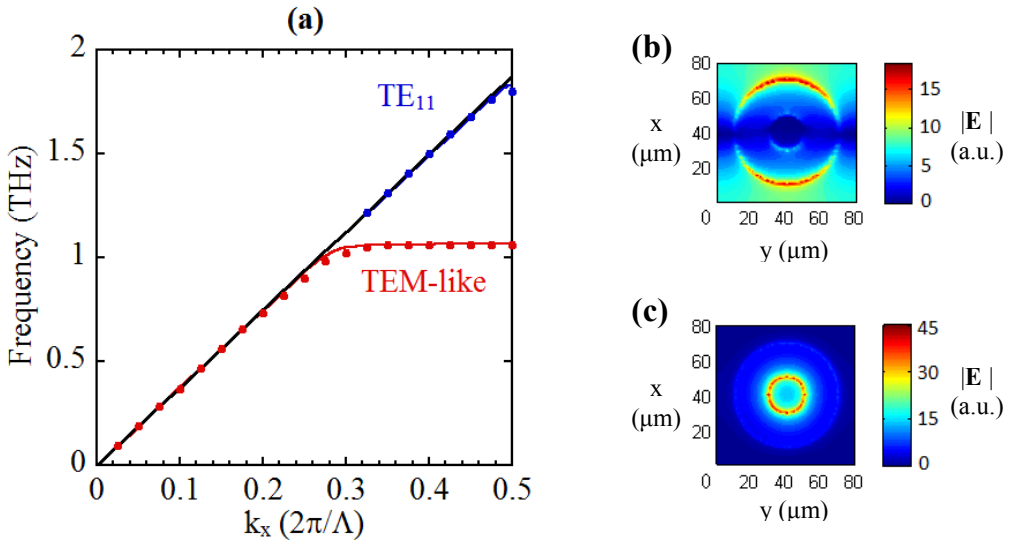

Figure 5.2. (a) Comparison between the MEA dispersion curve (solid lines) and FDTD simulations (points) for the parameter set h=60 μm, a_{in}=20 μm, a_{out}=60 μm and Λ=80 μm. (b-c) field maps at the band edge (k_x=π/d) evaluated 1 μm above the sample surface for (b) TE_{11} mode and (c) TEM-like mode. [MEA result is taken from a calculation performed by Sol Carretero-Palacios].

The dispersion of the two spoof plasmonic modes was verified via an analytical modal expansion approximation (MEA) calculation. In this case the structure is considered as a PEC and only the TEM and TE_{11} modes are considered within the cavities [1]. Both modes are matched to plane waves at the structure surface and higher order diffraction is implicitly included. Figure 5.2(a) shows a comparison between the dispersion curves calculated using the MEA (evaluated by colleagues at the Universidad de Zaragoza-CSIC) and that obtained from the FDTD simulations and demonstrates the close agreement.

FDTD simulations were also used to study the effect of varying the various structural parameters on the two mode cut-off frequencies. It can be seen from figure 5.3 that the cavity depth *h* plays the dominant role in controlling the TEM-like cut-off, whereas the other parameters a_{in} and a_{out} play no significant role. The TE_{11} cut-off is unaffected by the structural parameter variations, demonstrating that the dispersion of this mode arises from the array periodicity (see chapter 4). For this air-filled structure, the TE_{11} spoof-plasma frequency lies at ~2.4 THz and

cannot be accessed. In this case, the TE_{11} cut-off frequency can be approximated using $f_c \sim 2c/\pi(a_{in}+a_{out})$ [7].

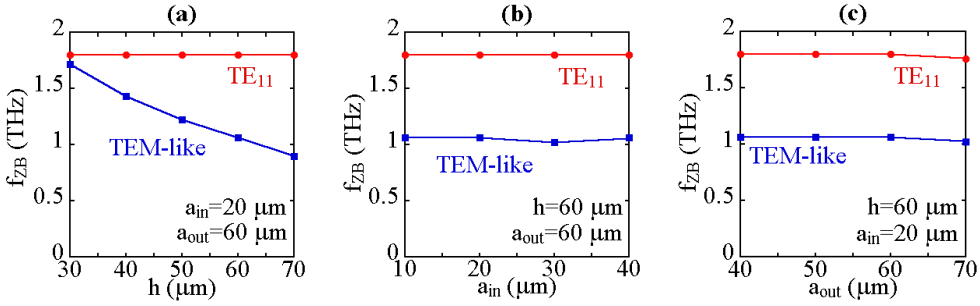

Figure 5.3. FDTD plots showing the effect of varying the parameters h, a_{in} and a_{out} on the modal cut-off frequencies at the zone boundary, f_{ZB}. In each case the other parameters are fixed to a_{in}=20 μm, a_{out}=60 μm, h=60 μm and Λ=80 μm.

It is clear from figure 5.3 that in order to clearly separate the two modes in frequency, deep cavities are required. For the structural parameters stated in the figure caption there is a critical depth of ~30 μm, below which the TEM-like spoof plasmon mode is lost above the light line.

5.3. Sample fabrication

High aspect ratio 38 x 8 mm arrays of annular holes with a_{in}=20±1 μm, a_{out}=60±1 μm, h=60±5 μm and Λ=80 μm, were fabricated in SU8-50 photoresist on Pyrex wafers via perfect contact optical lithography. In this process, a NiCr mask pattern is first transferred onto the Pyrex wafer via S1813 photolithography and liftoff. A 60 μm layer of SU8-50 photoresist is then coated onto the same side of the wafer and exposed through the NiCr. In this way, the problem of uneven exposure due to poor mask contact caused by non-uniformity and the presence of an edge bead was eliminated. Verticality of the side walls was found to be significantly improved by using an I-line UV-filter (λ=365 nm, $\Delta\lambda_{FWHM}$=20 nm). Metallisation of the samples, including the side walls, was achieved by sputter coating 3 μm of copper. This resulted in a top surface layer thickness of ~3 μm and cavity floor

and wall coverage of 1±0.5 μm. The ~8% variation in the hole depth is due to the spin coating process.

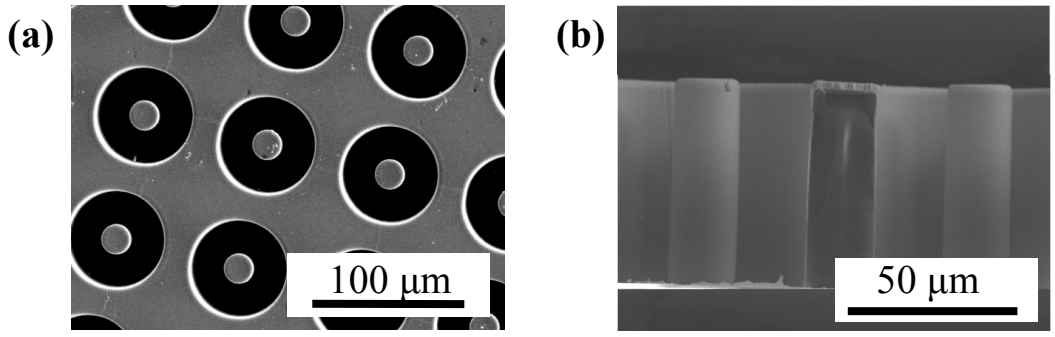

Figure 5.4. (a-b) SEM images of the coaxial sample. (b) shows a cross section of the structure. In this case, the darker region in the centre of the image is the side wall separating consecutive periods of the structure.

It is clear from figure 5.4 that the optimised SU8 fabrication technique removes the previous problem of undercut in the side walls (chapter 4) and allows much smaller feature sizes to be fabricated. It is anticipated that this fabrication technique could be used to create feature sizes down to ~10 μm, allowing the operating frequency of these metamaterial waveguiding structures to be pushed beyond 3 THz.

5.4. Experimental results

5.4.1. Far-field measurements

Initial experiments were carried out using the coplanar LT-GaAs photoconducting transmitter and 10 μm dipole receiver described in section 3.4. The coupling arrangement is shown in figure 5.5. In this experiment a new coupling technique was implemented using a pair of plano-cylindrical lenses with a FWHM beam focus at the lens face of ~200 μm at 1 THz. This technique has previously been used to couple terahertz radiation to parallel plate waveguides [8]. The samples

were separated from the lens faces by ~50 μm at both ends and translated perpendicular to the optical axis to optimise the coupling. The small sample-lens separation was set using a Mylar spacer which was removed before taking measurements. In this case, the lens focus provides efficient end-fire coupling by matching the symmetry of the mode and optimising the mode overlap. This scheme provides a much more efficient coupling mechanism than using razor blades (chapter 4) and allows the experimental geometry to be simplified. Removing the sample resulted in a reduction in the peak to peak signal by a factor of ~5 in amplitude, indicating that the free-space contribution to the detected SPP signal was small.

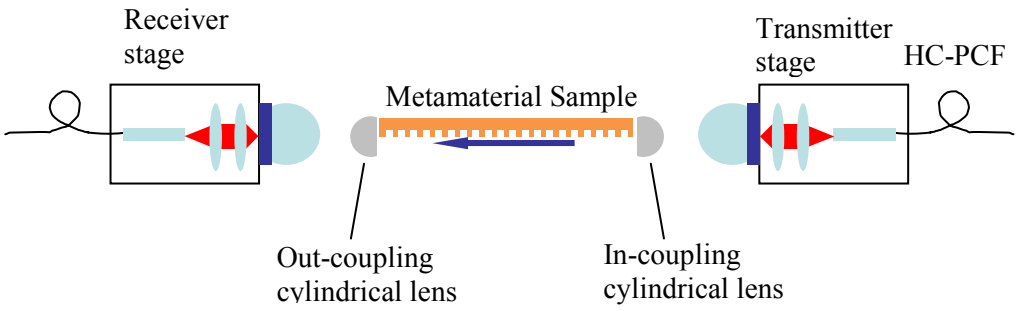

Figure 5.5. Schematic diagram of the coupling arrangement.

Figure 5.6 shows time-domain traces and spectra obtained after propagation along the coaxial sample. Also plotted is a reference signal obtained by removing the sample and keeping the lens separation fixed. It is clear that the presence of two SPP modes leads to beating in the time-domain and the production of two distinct peaks in the Fourier transform. It is also clear that the high frequency 'edges' of these peaks show excellent agreement with the position of the modal cut-offs predicted by the FDTD simulations and MEA calculations. From figure 5.6 it can be seen that a large peak to peak signal (>800 pA) can be produced by the lens coupling technique, greatly improving the signal-to-noise ratio.

In order to estimate the coupling efficiency, a separate reference signal with the lenses at their mutual focus was acquired and ratioed to the metamaterial signals. In this case, both the transmitter-to-lens and receiver-to-lens separations were kept

fixed. From this comparison, the total amplitude coupling efficiency was found to be >20% for both SPP modes. Due to the symmetry of the system, the in-coupling and out-coupling efficiencies are approximately equal. This implies that the average amplitude coupling efficiency at each lens exceeds 45%. This value provides a significant increase in coupling efficiency compared to other broadband coupling schemes reported to date in the literature. For example, aperture coupling using razor blades (chapter 4) typically yields an amplitude coupling efficiency of ~10% at each blade [9] whereas prism based edge-diffraction techniques have been reported to yield amplitude coupling efficiencies up to ~20% [10]. It is interesting to note that similar coupling efficiencies of ~50% have been reported in simulations of end-fire coupling to wires using radial antennas [11]. In this case, symmetry and spatial matching of the incident and guided fields proves to be critical. This also explains the high efficiency of our coupling technique.

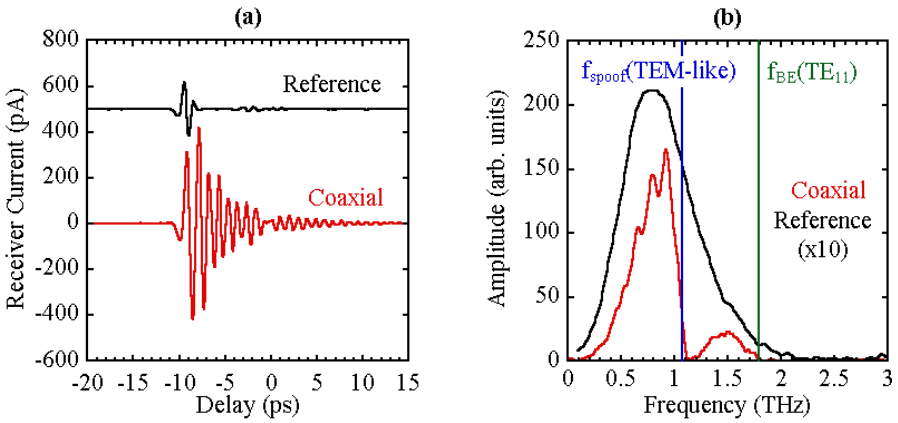

Figure 5.6. (a) Time-domain trace and (b) spectrum obtained for propagation along the coaxial metamaterial sample (red). A reference obtained by removing the sample is also plotted (black). The vertical blue and green lines correspond to the cut-offs calculated from FDTD simulations.

The improved signal to noise ratio from this coupling scheme enables the reliable extraction of phase information, allowing the SPP dispersion to be calculated using equation 4.4. Figure 5.7 shows the experimental phase data and extracted dispersion relation. It is clear from figure 5.7(a) that above the TEM-like cut-off there is an offset in the phase corresponding to ~13 radians (indicated by the

dashed blue line). From FDTD simulations, the dispersion curve would be expected to return to the light line at this point, before diverging again close to the TE_{11} mode cut-off. The most likely explanation for this offset is the finite frequency resolution of the experiment, which prevents the resonance close to the TEM-like plasma frequency from being resolved properly. In this case, the offset arises from the requirement for continuity of phase in the Fourier transform. When analysing the dispersion of the TE_{11} mode, this offset is subtracted from the data. Errors in the experimental data were estimated from repeat measurements and are not plotted in figure 5.7 for clarity. The experimental error in wavevector was highest at low frequencies (~15% at 0.4 THz, ~13% at 1.2 THz) and decreased close to the plateaued regions (~6% at 0.9 THz, ~10% at 1.5 THz). It is clear from figure 5.7(b) that within the range of Δk measured in the experiment, the experimental dispersion curves show close agreement with those calculated from the analytical modal expansion. The discrepancy in the case of the TEM-like mode can be accounted for by the ~8% variation in the cavity depth which affects the frequency of the mode cut-off (figure 5.3(a)).

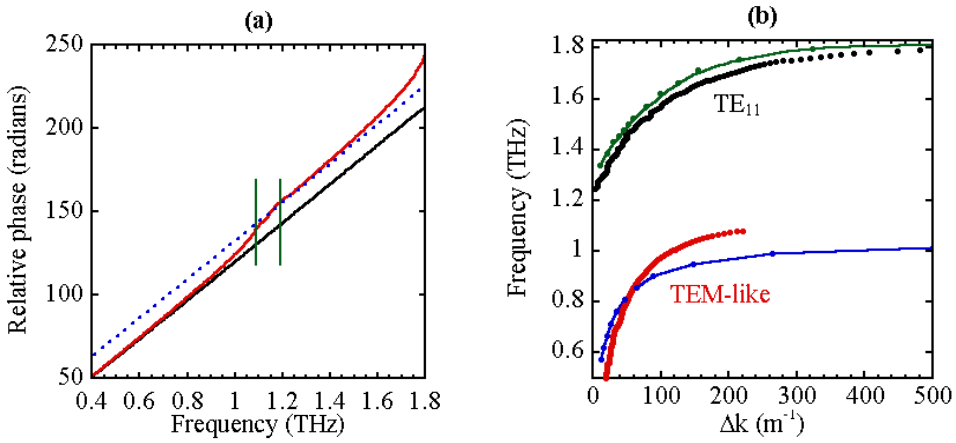

Figure 5.7. (a) Coaxial phase data (red), the light line is indicated in black. The dashed blue line corresponds to the phase offset discussed in the text and the vertical green lines indicate the spectral region omitted due to signal-to-noise reasons. (b) Extracted dispersion curve showing the TE_{11} (black) and TEM-like (red) modes. In the former case the phase offset is removed. The green and blue curves are derived from the MEA.

Experimentally, we cannot measure the very tightly bound fields close to the TEM-like cut-off. This is because the plateaued region of the dispersion curve is very tightly bound to the surface and displays a very small group velocity, leading to both higher attenuation and significant spreading of the signal in time. The very large wavevector components close to the TEM-like cut-off are also only weakly excited in the experiment due to the large phase mismatch with respect to light in free-space which results in tighter field confinement and hence lower modal overlap with the excitation field.

Using this data, we can calculate the confinement at the two spectral peaks shown in figure 5.6(b). For the TEM-like mode at 0.90 THz, we calculate a modal confinement of L_{zd}~621±39 μm (~2λ) and for the TE_{11} mode at 1.50 THz we obtain a value of L_{zd}~498±51 μm (~2.5λ). The uncertainties in each case are evaluated from the wavevector errors described above. These values for the field confinement are ~100 times smaller than expected for a flat copper sheet at the same frequencies (chapter 2) and demonstrate the ability to achieve wavelength-scale confinement of radiation at two distinct frequencies using coaxial structures. These values also show good agreement with the theoretical values extracted from the modal expansion calculation (~550 μm at 0.9 THz and 1.5 THz). Closer to the mode cut-off frequencies the confinement increases further. Figure 5.8 shows a comparison between the decay lengths experimentally extracted from the phase data and those calculated from the analytical modal expansion, which show reasonable agreement over a wide range of frequencies.

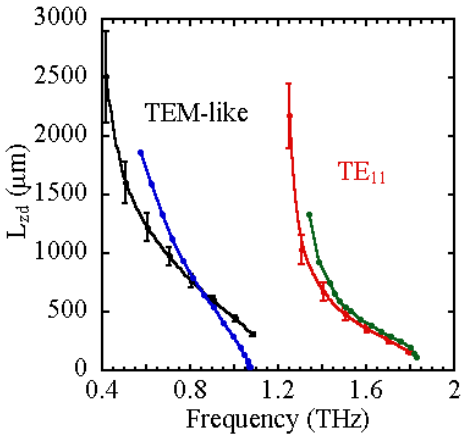

Figure 5.8. Out-of-plane decay length in air, evaluated from the experimental phase data (black and red curves) and MEA calculation (blue and green curves).

5.4.2. Near-field probing

In order to test the ability to probe the out-of-plane decay lengths directly, scans were performed using the aperture-based near-field dipole receivers described in section 3.6. In these experiments, in-coupling was achieved using the plano-cylindrical lens already discussed and the near-field receiver was scanned across the edge of the metamaterial at a fixed distance of ~50 μm. A removable steel razor blade placed ~4 mm from the in-coupling lens at a height of ~1 mm above the sample surface was used to help discriminate against unguided radiation. Figure 5.9(a) shows the field perpendicular to the plane at two frequencies, 0.9 THz and 1.5 THz, corresponding to the two spectral peaks shown in figure 5.6(b).

Exponential fits to the data enabled the out-of-plane decay length, L_{zd}, to be extracted directly. Interestingly, both with and without the razor blade, a finite background signal was detected. This is accounted for in the exponential fitting. We tentatively assign this contribution to radiation lost by the SPP via diffraction. From these measurements, we obtain average values of L_{zd}=320±55 μm at 0.9 THz and L_{zd}=298±62 μm at 1.5 THz. The errors in each case are evaluated from repeat measurements made with two different near-field probes (10 μm dipole with 20 μm and 60 μm apertures), both with and without the razor blade. The

discrepancy between these decay lengths and the values extracted from the phase data (which agree closely with theory) suggests that the metal screen on the near-field probe perturbs the field supported by the sample. In principle, an accurate determination of the SPP decay length would require a probe with no aperture, although in this case there might be a residual dielectric effect as well as arefacts associated with coupling to the metal tracks. A scan was also taken across the transverse axis of the sample, as shown in figure 5.9(b), collected using the larger aperture near-field probe (10 µm dipole with 60 µm aperture). In this case, the plot displays an approximately Gaussian transverse profile with FWHM ~6.1 mm. The lateral extent in this case is due to the line-focus produced by the in-coupling lens and the finite sample width.

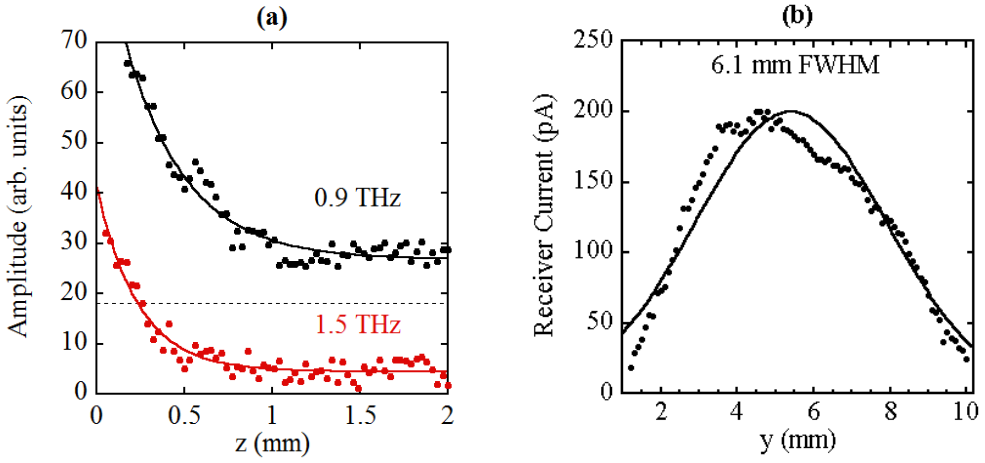

Figure 5.9. (a) Out-of-plane scans performed using the 10 µm dipole with 20 µm aperture (vertically offset for clarity) and (b) transverse near-field scan performed using the 10 µm dipole with 60 µm aperture. Both scans were obtained at a probe-sample separation of ~50 µm. Points represent experimental data and lines correspond to exponential and Gaussian fits to the data plotted in (a) and (b) respectively. The horizontal dashed line in (a) represents the position of zero amplitude for the 0.9 THz scan.

Despite the low signal strengths, the adequate signal-to-noise ratio of these measurements is demonstrated in figure 5.10(a) for a scan captured with only 40 averages. The corresponding spectrum, shown in figure 5.10(b), displays two distinctive peaks as with the far-field measurements discussed earlier (figure 5.6). The relative decrease in the low-frequency part of the spectrum is due to the high-pass filtering behaviour of the 20 µm aperture.

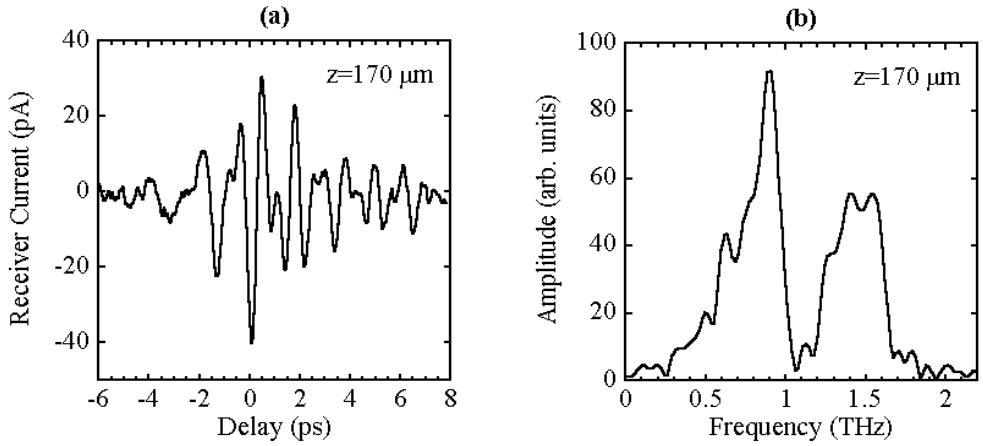

Figure 5.10. (a) Time-domain trace and (b) spectrum obtained using the 10 μm dipole with 20 μm aperture near-field probe at a distance ~170 μm above the coaxial metamaterial sample.

5.4.3. Attenuation measurements

In order to measure the amplitude attenuation of the coaxial structure, a cut-back method was implemented in the experimental geometry shown in figure 5.5. In this approach, the sample was removed between measurements and reduced in length by cleaving. For each measurement, the out-coupling lens and receiver were then repositioned to maintain a constant sample-lens and lens-receiver separation. From these measurements the amplitude attenuation was found to be 0.22±0.06 cm^{-1} (figure 5.11(b)). The biggest source of error comes from the variation in coupling efficiency due to slight variations in sample position between measurements (shown by the error bars in figure 5.11(b)). For comparison, FIT simulations were used to calculate the amplitude attenuation as described in chapter 4. In this case, the effects of diffractive and Ohmic loss could be straightforwardly separated by first modelling the structure as a PEC and then as a lossy conductor (copper) with $\sigma_0 = 5.8.10^7\ \Omega^{-1}m^{-1}$. In this case the total loss was found to be 0.20 cm^{-1}, in good agreement with the experimental result. From the PEC calculation the diffractive contribution is estimated to be 0.15 cm^{-1} and clearly dominates over the Ohmic contribution. These properties are very encouraging in terms of high-confinement waveguiding due to the tolerable trade-off between loss and confinement.

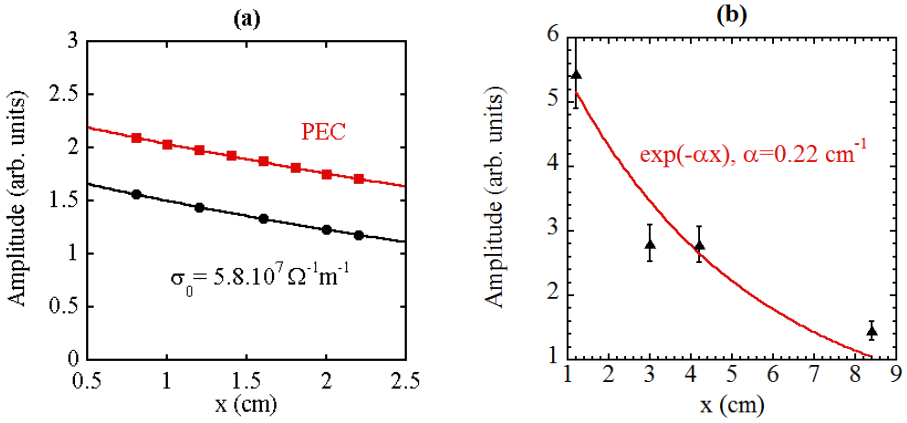

Figure 5.11. (a) SPP amplitude calculated from an FIT calculation (points) for various propagation lengths along the coaxial structure. Lines represent exponential fits to the data. (b) experimental measurements (triangles) of the amplitude attenuation using a cut-back method. The solid red line corresponds to an exponential fit to the data.

5.5. Summary

In summary, a novel cylindrical-lens coupling geometry was shown to enable highly efficient SPP excitation on metamaterial samples consisting of two-dimensional coaxial hole arrays. Samples were shown to support two spoof-plasmon modes, allowing wavelength-scale field confinement to be experimentally realised at two distinct frequencies (L_{zd}=621±39 μm at 0.9 THz and L_{zd}=498±51 μm at 1.5 THz) in good agreement with values obtained from an analytical calculation. The lower frequency mode has a frequency cut-off determined by the cavity resonance where as the higher frequency mode is cut off by periodicity. For comparison, direct measurement of the out-of-plane decay length was attempted using near-field probing. From this measurement, values of L_{zd}=320±55 μm at 0.9 THz and L_{zd}=298±62 μm at 1.5 THz were obtained. The discrepancy between the near-field and phase measurements of the out-of-plane confinement (which closely agree with theory) seems to indicate that the metal screen of the probe perturbs the field being measured. Accurate probing probably requires the fabrication of probes without apertures, although in this case there may be a residual dielectric effect and artefacts associated with coupling to the

metal tracks. The propagation loss on the coaxial sample was experimentally measured using a cut-back method and found to be 0.22±0.06 cm^{-1} in excellent agreement with FIT simulations which predict losses of 0.20 cm^{-1}. These simulations also enable us to identify diffraction as the key loss mechanism. From FDTD simulations it has been shown that, in principle, bound fields decaying within ~λ/9 of the sample surface are supported close to the TEM-like cavity cut-off. This produces a five-fold field enhancement with respect to the field confinement at the higher frequency band edge, where radiation is confined by diffraction. The dual wavelength capability is particularly attractive in terms of sensing, as is the fact that the structures are air-filled and access to the bound fields remains unrestricted. In terms of sensing, we anticipate that these structures could be straightforwardly applied to thin film sensing by detecting the resonant shift in both cut-off frequencies. In this case, quantifying the resonant shifts would enable different dielectrics to be separated and allow the frequency dependent refractive index and absorption gradients to be estimated. In terms of biosensing it is also conceivable that this functionality might enable different molecular conformations to be separated. Another possibility would be to match the engineered metamaterial cut-offs to the known resonant phonon peaks in a crystalline solid. In this case, one might expect a resonant enhancement in sensitivity due to the combination of resonances. The great advantage of the metamaterial approach to sensing is that the structures are freely scalable and by using the fabrication technique described, could be designed to operate anywhere within the range 0.1-3.6 THz.

References

[1] N. Marcuvitz. *Waveguide handbook.* McGraw-Hill Book Company Inc. New York (1951).

[2] A. Roberts and R. C. McPhedran. *Bandpass grids with annular apertures*. IEEE Trans. Antennas Propag. **36**(5), 607-611 (1988).

[3] P. A. Krug, D. H. Dawes, R. C. McPhedran, W. Wright, J. C. Macfarlane and L. R. Whitbourn. *Annular-slot arrays as far-infrared bandpass filters.* Opt. Lett. **14**(17), 931-933 (1989).

[4] F. I. Baida and D. Van Labeke. *Light transmission by subwavelength annular aperture arrays in metallic films.* Opt. Commun. **209**, 17-22 (2002).

[5] W. Fan, S. Zhang, K. J. Malloy and S. R. J. Brueck. *Enhanced mid-infrared transmission through nanoscale metallic coaxial-aperture arrays.* Opt. Express **13**(12), 4406-4413 (2005).

[6] W. Fan, S. Zhang, B. Minhas, K. J. Malloy and S. R. J. Brueck. *Enhanced infrared transmission through subwavelength coaxial metallic arrays.* Phys. Rev. Lett. **94**, 033902 (2005).

[7] F. I. Baida, A. Belkhir, D. Van Labeke and O. Lamrous. *Subwavelength metallic coaxial waveguides in the optical range: role of the plasmonic modes.* Phys. Rev. B **74**, 205419 (2006).

[8] R. Mendis and D. Grischkowsky. *Undistorted guided-wave propagation of subpicosecond terahertz pulses.* Opt. Lett. **26**(11), 846-848 (2001).

[9] E. V. Alieva, G. Beitel, L. A. Kuzik, A. A. Sigarev, V. A. Yakovlev, G. N. Zhizhin, A. F. G. van der Meer and M. J. van der Wiel. *Linear and nonlinear FEL-SEW spectroscopic characterization of nanometer-thick films.* Appl. Spectrosc. **51**(4), 584-591 (1997).

[10] J. F. O'Hara, R. D. Averitt and A. J. Taylor. *Prism coupling to terahertz surface plasmon polaritons.* Opt. Express **13**(16), 6117-6126 (2005).

[11] J. A. Deibel, K. Wang, M. D. Escarra and D. M. Mittleman. *Enhanced coupling of terahertz radiation to cylindrical wire waveguides.* Opt. Express **14**(1), 279-290 (2006).

6. Studies of surface plasmon polaritons on metawires

6.1. Introduction

The surface of a wire can support an azimuthally independent, radially polarised SPP called the Sommerfeld wave [1]. Recently, the properties of this mode have received growing attention because of possible applications in terahertz waveguiding [2,3,4,5] and sensing [6,7]. Unfortunately, in the terahertz region, the close proximity of the Sommerfeld wave dispersion curve to the light-line leads to poor modal confinement. This is detrimental to sensing and also for waveguiding due to increased bend loss [3] and the potential for electromagnetic coupling to nearby objects.

Although it has long been known that the radial extent of the Sommerfeld wave can be reduced by applying thin dielectric coatings [8], surface structuring provides a potentially more flexible approach to engineering the dispersion [9,10]. The idea of using corrugated wires for waveguiding, builds upon work from the 1950s in which the propagation of microwaves along cylinders with arrays of discrete [8,11] and helical [11] grooves was explored. Despite these early works at lower frequency, the idea of using sub-wavelength structured corrugated wires for terahertz waveguiding has only recently received much attention, with theoretical studies predicting sub-wavelength field confinement on wires textured with periodic arrays of circumferential grooves called metawires [12,13]. In comparison with smooth wires, this increase in field confinement not only makes the structures less susceptible to bend loss, but also produces large field enhancements at the wire surface, something that is particularly attractive in terms of sensing. Simulations also suggest that either by gradually tapering the metawire or grading the groove depth, energy can be concentrated into increasingly smaller volumes, in the former case facilitating narrowband terahertz super-focussing [12,13]. Terahertz focussing using tapered smooth wires has also been simulated [14], indirectly inferred by experiment [15] and described quasi-analytically [16]. This builds on the well-known idea that reducing the wire diameter reduces the

radial decay length into the dielectric [8]. Despite the fact that it is difficult to directly compare the two focussing approaches, in part due to the huge flexibility in design parameters in the metawire case, the analysis of Shen et al. [17] in which the effects of loss are explicitly included, provides some evidence that the focussing capabilities may be similar. The same analysis also suggests that the finite conductivity of the metal becomes increasingly important as energy is focussed, due to enhanced absorption resulting from increased energy concentration within the metal. This is important as it may limit practical focussing capabilities.

In this chapter, we present the first experimental results demonstrating terahertz waveguiding on helical and discretely grooved metawires. We also present a detailed theoretical analysis of the dispersion and azimuthal symmetry of the SPP modes supported by both classes of structure. We begin in section 6.2 by outlining the theory describing Sommerfeld wave propagation along smooth wires, before moving on to discuss the theory describing SPP propagation on both discretely grooved (section 6.3) and helical geometry (section 6.4) metawires. In section 6.5 the sample fabrication and experimental setup are outlined and finally, in section 6.6, experimental results are presented and discussed.

6.2. Sommerfeld wave theory

The propagation of SPPs along a cylindrical metal-dielectric interface was first examined by Sommerfeld in 1899 [1]. For a metal wire bounded by air, Maxwell's equations can be solved independently within the metal and dielectric regions. Continuity of the fields is then imposed at the wire surface, allowing a transcendental equation to be formulated, which can be solved numerically to yield the Sommerfeld wave solution. In addition to this mode, a variety of azimuthally-dependent modes may also be supported, but they are quickly attenuated as the majority of the field resides in the metal region [1].

To find the Sommerfeld wave solution, Maxwell's equations are evaluated within the cylindrical coordinate system (ρ,θ,z). The time dependency of the fields is assumed to be harmonic and is omitted for clarity. Within the dielectric region bounding the wire, the radially decaying electromagnetic fields can be described by modified Bessel functions [13] and are given by,

$$E_z(\rho,z) = E_d K_0(iq_d\rho)\exp(ik_z z) \tag{6.1}$$

$$H_\theta(\rho,z) = \frac{\varepsilon_d k_0}{q_d Z_0} E_d K_1(iq_d\rho)\exp(ik_z z) \tag{6.2}$$

where E_z is the electric field component along the axis of the wire, E_d is the electric field amplitude within the dielectric and K_0 and K_1 are the modified Bessel functions of the second kind (order 0 and 1 respectively) that control the radial decay into the dielectric. The total wavevector within the dielectric is $k_0 = \omega/c$ and is linked to the radial and propagation wavevector components, q_d and k_z, by the expression $\sqrt{\varepsilon_d}k_0 = \sqrt{k_z^2 + q_d^2}$ and $Z_0 = \sqrt{\mu_0/\varepsilon_0}$ is the impedance of free-space.

Similar expressions to equations 6.1 and 6.2 can be formulated for the fields in the metal,

$$E_z(\rho,z) = E_m I_0(iq_m\rho)\exp(ik_z z) \tag{6.3}$$

$$H_\theta(\rho,z) = -\frac{\varepsilon_m(\omega)k_0}{q_m Z_0} E_m I_1(iq_m\rho)\exp(ik_z z) \tag{6.4}$$

where E_m is the electric field amplitude in the metal, I_0 and I_1 are the modified Bessel functions of the first kind, $q_m = \sqrt{\varepsilon_m(\omega)\cdot k_0^2 - k_z^2}$, is the radial wavevector within the metal and $\varepsilon_m(\omega)$ is the dielectric function of the metal.

Imposing continuity of E_z and H_θ at the wire surface ($\rho=R$) yields,

$$\frac{q_d}{\varepsilon_d}\frac{K_0(iq_dR)}{K_1(iq_dR)} = -\frac{q_m}{\varepsilon_m(\omega)}\frac{I_0(iq_mR)}{I_1(iq_mR)} \tag{6.5}$$

Equation 6.5 can be solved numerically to evaluate the dispersion relation of the Sommerfeld wave, as shown in figure 6.1. A simple Drude model is used to evaluate the dielectric function of the metal to provide qualitative information on the Sommerfeld dispersion curve. It is important to realise that above ~480 THz for copper [18], the metal absorption increases dramatically due to the onset of interband transitions and the accuracy of the Drude model breaks down. Despite this, the model can still be used to describe the qualitative behaviour of the Sommerfeld wave dispersion.

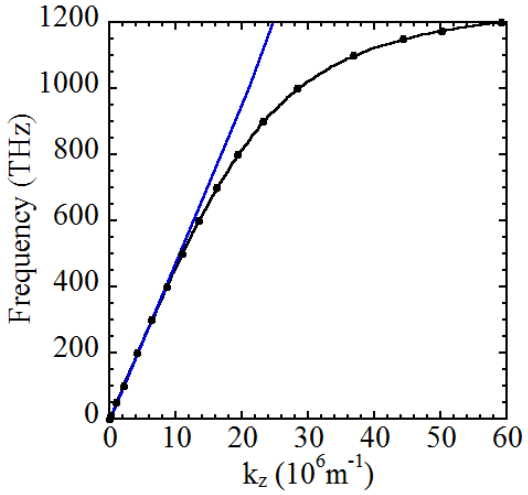

Figure 6.1. Dispersion relation of the Sommerfeld wave (black) calculated from equation 6.5 using a Drude model for copper, with parameters $\omega_\tau = 1.38.10^{13}$ *rad.s*$^{-1}$ *and* $\omega_p = 1.12.10^{16}$ *rad.s*$^{-1}$ *[19] for an R=600 μm wire bounded by air* ($\varepsilon_d=1$). *The light line is plotted in blue.*

It is clear that at visible frequencies, the Sommerfeld wave dispersion curve deviates significantly from the light line, indicating tight field confinement to the wire surface. At terahertz frequencies however, where the dispersion curve lies close to the light line, the mode is only weakly confined, extending tens of wavelengths into the bounding dielectric. Within the terahertz region, this lack of

confinement fundamentally limits the application of terahertz Sommerfeld waves to guiding and sensing, although the low dispersion and attenuation are attractive. In order to gain more information about the properties of the Sommerfeld wave, the frequency-dependent radial decay length in air $L_{\rho d}$ and amplitude attenuation length L_z can be calculated from the radial and in-plane wavevectors using expressions equivalent to equations 2.7 and 2.9 (figure 6.2).

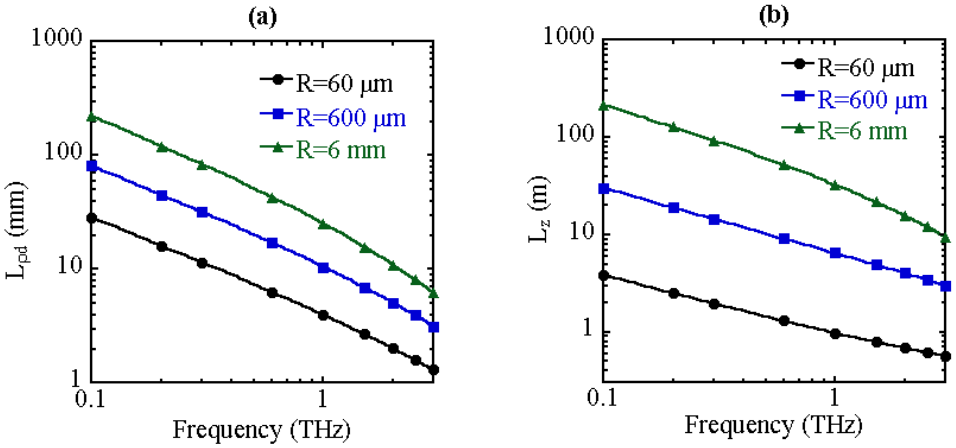

Figure 6.2. (a) Radial decay length into air for differing wire radii, evaluated from equation 6.5 using a Drude model for copper with parameters $\omega_\tau = 1.38.10^{13}$ *rad.s*$^{-1}$ *and* $\omega_p = 1.12.10^{16}$ *rad.s*$^{-1}$ *[19]. (b) Attenuation lengths for different wire radii evaluated from the Sommerfeld model with identical Drude parameters.*

As well as being strongly dependent on frequency, figure 6.2 shows that both the field extension into air and attenuation length are strongly influenced by the wire radius [20]. In the limiting case where R tends to infinity and the curvature of the wire surface becomes negligible, asymptotic expressions for the modified Bessel functions yield the Zenneck wave solution describing SPP propagation on a flat metal sheet. In the opposite limit, where the wire radius tends to zero, it has been suggested that the skin depth within the metal is increasingly enhanced due to coherent interference between the radially symmetric field components around the curved surface [21]. This effect is most pronounced for low frequencies where the absolute value of the skin depth is largest and results in terahertz wave propagation with a phase velocity much less than the speed of light. For this reason a phase lag develops between the high and low frequency components and

the asymptotic approach of the dispersion curve to the light line can deviate significantly from theory. In the Sommerfeld model, the penetration depth into the metal is found to be independent of wire radius. Therefore for wire radii below the skin depth (~65 nm at 1 THz for copper) the Sommerfeld model breaks down.

6.3. Discretely grooved metawire (U-ring) theory

The poor confinement of terahertz SPPs propagating along metal wires (Sommerfeld waves) can be dramatically improved by structuring the metal on a sub-wavelength scale to form a metamaterial. As for the case of planar metamaterials, a sub-wavelength structured metawire formed from a PEC can support confined spoof plasmons with dispersion characteristics controlled by the cut-off properties of the cavities. The effects of the finite conductivity of the metal are generally neglected at terahertz frequencies due to the small penetration depth into the metal. This allows the metawire to be modelled as a PEC, dramatically simplifying the implementation of boundary conditions. The simplest metawire design is the U-ring structure represented schematically in figure 6.3, which consists of a PEC wire of outer radius R, inscribed with an array of periodic grooves of pitch Λ, width a and depth h.

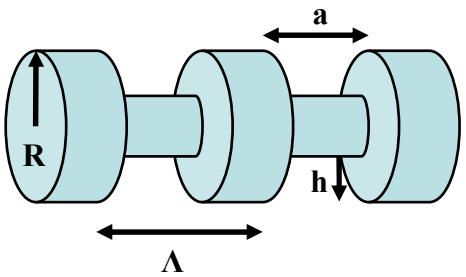

Figure 6.3. Schematic diagram of the U-ring metawire structure.

As the U-ring structure is periodic, Bloch's theorem can be used to solve Maxwell's equations over a single unit cell. Within the air-filled ($\varepsilon_d=1$) grooves,

the electromagnetic fields can be expanded as a sum of propagating and counter-propagating radial ring waveguide modes (index *l*) [13] as,

$$E_z(\rho,z)=\sum_l D_l\left(J_0(q_l\rho)-\frac{J_0(q_l r)}{N_0(q_l r)}N_0(q_l\rho)\right)\chi_l(z) \tag{6.6}$$

$$H_\theta(\rho,z)=\sum_l -\frac{k_0\varepsilon_d}{q_l Z_0}D_l\left(J_1(q_l\rho)-\frac{J_0(q_l r)}{N_0(q_l r)}N_1(q_l\rho)\right)\chi_l(z) \tag{6.7}$$

where D_l are the modal amplitudes, $q_l=\sqrt{\varepsilon_d k_0{}^2-(\pi l/a)^2}$ are the radial mode wavevectors within the cavities, J_0 and J_1 are Bessel functions (order 0 and 1 respectively), N_0 and N_1 are Neumann functions (order 0 and 1 respectively), $r=R-h$ is the inner ring radius and χ_l represent the ring waveguide modes which are only non-zero within the grooves and are given by,

$$\chi_l(z)=\sqrt{(2-\delta_{l,0})/a}\cos\left(\frac{\pi l}{a}[z+a/2]\right)\ \text{for}\ |z|<\frac{a}{2} \tag{6.8}$$

For the region bounding the metawire ($\rho>R$) the electromagnetic fields can be expanded as a sum of diffraction orders as,

$$E_z(\rho,z)=\sum_{n=-\infty}^{\infty}C_n K_0(iq_n\rho)\frac{\exp(ik_n z)}{\sqrt{\Lambda}} \tag{6.9}$$

$$H_\theta(\rho,z)=\sum_{n=-\infty}^{\infty}\frac{k_0\varepsilon_d}{q_n Z_0}C_n K_1(iq_n\rho)\frac{\exp(ik_n z)}{\sqrt{\Lambda}} \tag{6.10}$$

where C_n are the nth-order diffraction coefficients, $q_n=\sqrt{\varepsilon_d k_0{}^2-k_n{}^2}$ is the radial wavevector associated with the n^{th} diffraction order and $k_n=k_z+2\pi n/\Lambda$ is the propagation wavevector associated with the n^{th} diffraction order.

In order to derive the transcendental equation, continuity of the electromagnetic fields is enforced at the surface forming the outer radius of the wire ($\rho=R$). In

practice, the matching process is greatly simplified by considering only the fundamental ring waveguide mode ($l=0$) which is always propagating ($q_0=k_0$) and can therefore be assumed to dominate the field behaviour within the circumferential grooves [13]. This assumption is valid as long as the free-space wavelength is much larger than the groove width, yielding the transcendental continuity equation given by,

$$\sum_{n=-\infty}^{\infty} \frac{k_0}{q_n} \frac{K_1(iq_nR)}{K_0(iq_nR)} \left|\Omega_{l=0,n}\right|^2 = -\frac{J_1(k_0R)N_0(k_0r) - J_0(k_0r)N_1(k_0R)}{J_0(k_0R)N_0(k_0r) - J_0(k_0r)N_0(k_0R)} \quad (6.11)$$

where $\Omega_{l=0,n} = \sqrt{a/\Lambda} \cdot sinc(k_n a/2)$ is the overlap integral that describes the coupling between the $l=0$ ring waveguide mode and the n^{th}-order diffracted Bloch wave. As with the Sommerfeld continuity equation, equation 6.11 can be solved numerically to yield the dispersion for the lowest order SPP mode supported by the U-ring structure. Figure 6.4 illustrates that this quasi-analytical approach is in good agreement with numerical FDTD simulations.

The inclusion of higher order ring waveguide modes in the above analysis involves computing an extended set of overlap integrals ($\Omega_{l,n}$) between each of the n Bloch modes in vacuum and l ring waveguide modes within the grooves. In this case, a more involved field matching procedure is required, which in the case where $\lambda >> a$, results in only minor modifications to the SPP dispersion curve.

In the limit where R tends to infinity, the asymptotic expressions for the Bessel functions can be used. In this case, equation 6.11 takes the simplified form of the dispersion relation describing SPP propagation along a planar one-dimensional array of grooves, given by [10],

$$k_z = k_0 \sqrt{1 + \left(\frac{a}{\Lambda}\right)^2 \tan^2(k_0 h)} \quad (6.12)$$

In this case, the spoof plasma frequency, $f_{spoof} = c/4h$, controls the behaviour of the fields at large wavevectors. The dependence of f_{spoof} on h in this simplified model shows that the critical parameter in controlling the dispersion is the groove depth. Increasing h leads to a lowering of the spoof plasma frequency and flattening of the SPP dispersion curve. This behaviour is also common to the U-ring structure.

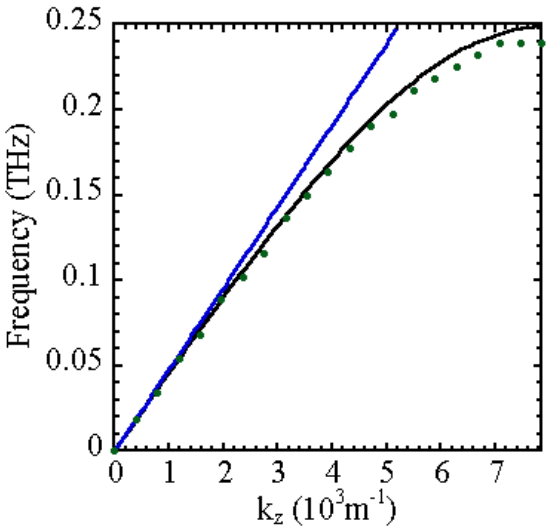

Figure 6.4. Comparison between dispersion curves calculated using the quasi-analytical U-ring model (black curve) and FDTD simulations (green points) for R=600 μm, Λ=400 μm, a=200 μm and h=150 μm. The light line is plotted in blue.

As well as the azimuthally independent *m=0* mode described thus far, the U-ring structure supports a number of higher-order modes exhibiting azimuthal dependence. In this case, an additional factor of $e^{im\theta}$ must be included in the field expressions and the TE (transverse-electric) and TM solutions of Maxwell's equations cannot be decoupled. In order to map out the dispersion of the higher *m>0* modes, FDTD simulations can be used. Figure 6.5 shows the full set of modal dispersion curves (including *m=0*) obtained for a U-ring metawire with parameters stated in the figure caption. The absolute electric field maps of the azimuthally varying modes evaluated at the band edge are also displayed.

It is evident from figure 6.5 that the field maps associated with the m^{th} SPP mode, for $m>0$, exhibit $2m$ circumferential nodes and no odd numbered nodal solutions exist. The significance of this point will become evident in the next section.

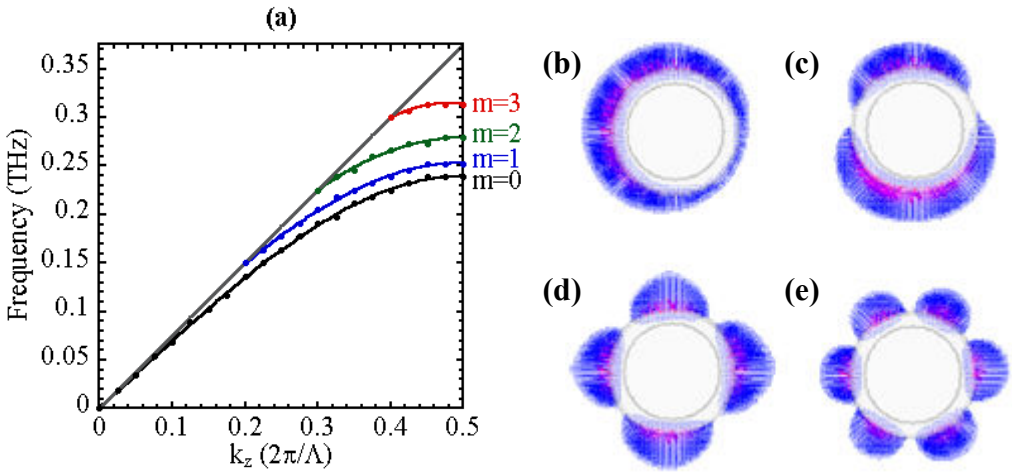

*Figure 6.5. (a) Dispersion curves for the full set of SPP modes evaluated on a U-ring metawire with R=600 μm, Λ=400 μm, a=200 μm and h=150 μm. Also plotted is the light line (grey line). (b)-(e) |**E**| maps evaluated at the band edge ($k_z=\pi/\Lambda$). Purple corresponds to high fields and blue to low. (b) m=0. (c) m=1. (d) m=2. (e) m=3.*

As the structure under consideration is azimuthally symmetric, the asymmetry in the field plots shown in figure 6.5 is attributed to the off-axis positioning of the excitation field.

6.4. Helical metawire theory

We now move on to consider a helical metawire consisting of one wire tightly wound around another straight wire of the same diameter, as depicted schematically in figure 6.6. For this type of structure, no analytical model exists and the SPP dispersion and field distributions are evaluated using FDTD simulations in which the helical grooves are modelled with a triangular profile.

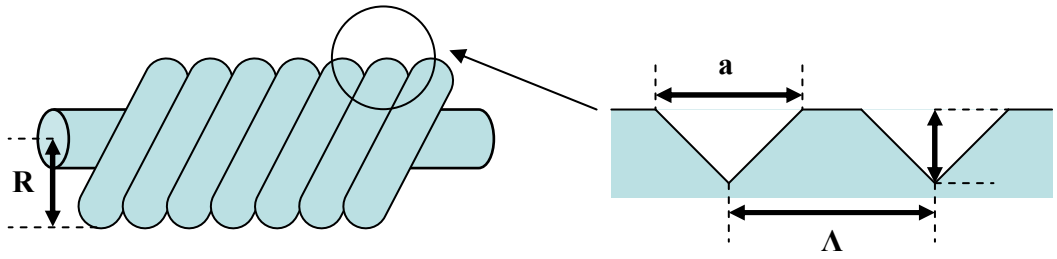

Figure 6.6. Schematic diagram of the helical metawire structure with close up of the approximately triangular groove profile.

Figure 6.7 shows that for the helical metawire, the lack of azimuthal symmetry leads to very different electric field distributions at the band edge, in that the m^{th} SPP mode now exhibits $2m+1$ circumferential nodes. It is also clear that with decreasing wavevector, the number of nodes in the field pattern gradually reduces by one and becomes even. Thus, at long wavelengths, the modes found on a helical metawire resemble those found on a U-ring metawire.

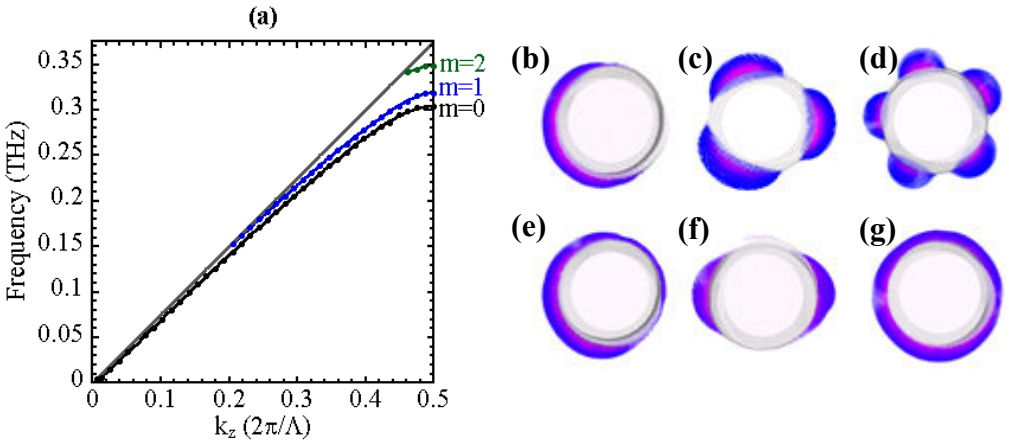

*Figure 6.7. (a) Dispersion curves for the full set of SPP modes evaluated on a helical metawire with R=600 μm, Λ=400 μm, a=200 μm and h=150 μm. Also plotted is the light line (grey line). (b)-(g) |**E**| maps for the helical metawire SPP modes. Purple corresponds to high fields and blue to low. (b) m=0 at $k_z=\pi/\Lambda$ (c) m=1 at $k_z=\pi/\Lambda$ (d) m=2 at $k_z=\pi/\Lambda$ (e) m=0 at $k_z=0.8\pi/\Lambda$ (f) m=1 at $k_z=0.5625\pi/\Lambda$ (g) m=0 at $k_z=0.59\pi/\Lambda$. [Results are extracted from an FDTD simulation carried out by Antonio Fernández-Domínguez].*

In order to appreciate why the SPP modes supported by the helical metawire exhibit this k_z dependent symmetry, the electromagnetic fields bound to the helical structure can be expanded in terms of diffracted waves [22,23] as,

$$F_m(\rho,\theta,z) = \exp(ik_z z)\exp(im\theta)\sum_n A_{n,m-n}(\rho)\exp\left(in\{2\pi z/\Lambda - \theta\}\right) \quad (6.13)$$

where the modal amplitude $A_{n,m-n}(\rho)$ contains the radial dependence of the n^{th} diffracted wave and $F_m(\rho,\theta,z)$ is an eigenfunction of the helical translation operator $S_{\varphi,\frac{\Lambda\varphi}{2\pi}}$ [22] satisfying the relation,

$$S_{\phi,\frac{\Lambda\phi}{2\pi}} F_m(\rho,\theta,z) = F_m\left(\rho,\theta+\phi,z+\frac{\Lambda}{2\pi}\phi\right) = \exp\left(i\left\{m+k_z\frac{\Lambda}{2\pi}\right\}\phi\right)F_m(\rho,\theta,z) \quad (6.14)$$

At this point, it is useful to introduce the helical coordinate ξ [24] which is parallel to the cylindrical coordinate z, but measured from the surface $z = \Lambda\theta/2\pi$,

$$\xi = z - \frac{\Lambda\theta}{2\pi} \quad (6.15)$$

The SPP fields given by equation 6.13 can then be reformulated in terms of ξ as,

$$F_m(\rho,\theta,\xi) = f(\rho,\xi)\exp\left(i\left\{m+k_z\frac{\Lambda}{2\pi}\right\}\theta\right) \quad (6.16)$$

When equation 6.16 is evaluated along the helical surface (ξ=*constant*), the eigenfunction evolves in time as $cos\left[(m+k_z\Lambda/2\pi)\theta-\omega t\right]$. For this reason, snapshots of the electromagnetic fields at the band edge where $k_z = \pi/\Lambda$ show $2m+1$ nodes along one helix pitch, as θ is varied from 0 to 2π, whereas for $k_z=0$, they show only $2m$ nodes.

6.5. Experimental setup

Two grooved wires were studied in this work. A 15 cm long helically grooved metawire was formed by tightly wrapping steel wire of ~400 μm diameter around a ~400 μm diameter steel core. The metawire was nickel plated to ensure robustness and the input and output end faces were polished flat. The resultant structure had a period of 400±10 μm and an approximately triangular groove profile of base width ~200 μm and depth ~150 μm (figure 6.8). A 15 cm long U-ring metawire was fabricated by physical machining, in this case with the parameters a=100±5 μm, h=250±12 μm, Λ=200±10 μm and R=1250±60 μm. Comparison was made with a bare copper wire of radius 600 μm.

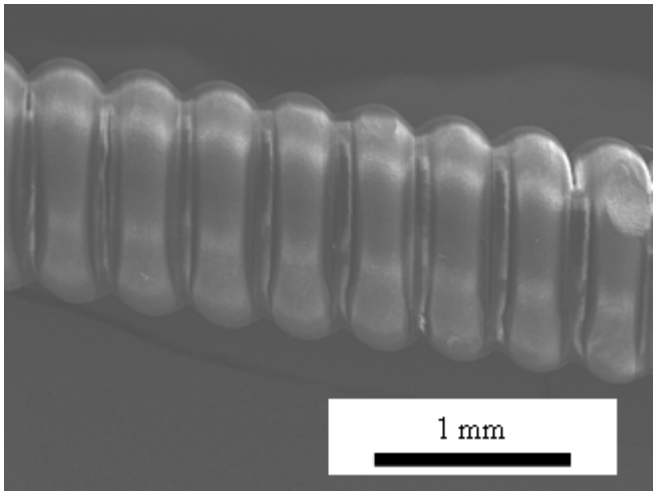

Figure 6.8. SEM image of the helical metawire structure.

Each of the metawire structures was studied using the radially polarised transmitter and 50 μm ion-implanted receiver described in chapter 3. The terahertz beam generated by the transmitter was collimated to a diameter of ~6 mm using a silicon substrate lens and end-fire coupled to the wire [25], which was placed ~2 mm away from the tip of the lens. In this geometry, efficient SPP excitation occurs by matching the symmetry of the mode and optimising the mode overlap. The lens to wire distance was kept constant in these experiments by using a thin expanded polystyrene disk (transparent at terahertz frequencies) as a spacer. Radiation propagating off the output end of the wire was similarly out-coupled to

the 50 μm ion-implanted GaAs dipole receiver. On the output side, the wires were slightly displaced from the optical axis to maximise the detected signal.

Various alternative coupling mechanisms have been suggested in the literature, including focussing linearly polarised light onto grooves milled into the wire surface [26] or onto a wavelength scale gap defined by a perpendicularly oriented wire [2]. Another approach involves coaxial aperture excitation via the insertion of a tapered metal wire into a sub-wavelength circular aperture [27]. The latter two techniques were initially trialled in this work and found to be ~3-6 times less efficient than the coupling scheme illustrated in figure 6.9.

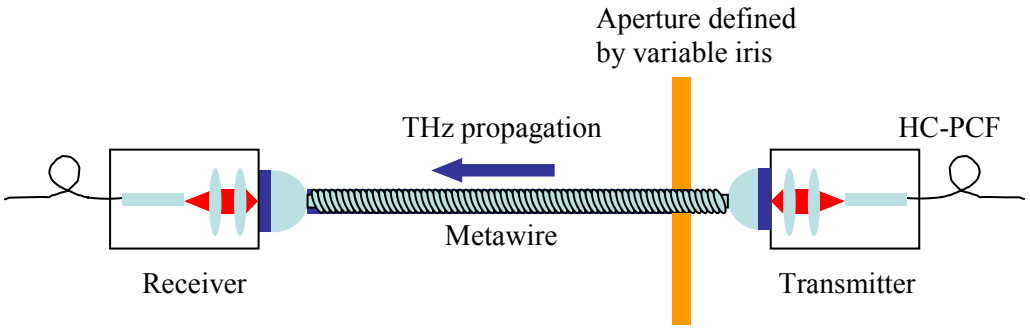

Figure 6.9. Schematic diagram of the end-fire coupling apparatus.

In the helical metawire case, the elimination of free-space contributions to the detected signal was partially achieved using the iris aperture depicted in figure 6.9 which was located ~1 cm from the input end of the wire. Setting the aperture to a diameter of ~3 mm was found to reduce the free-space background significantly, without affecting the metawire signal. Further to this, the helical metawires were curved along the arc of a circle of radius 26 cm. In the U-ring case, an aperture was also used, but in this case the diameter was set to ~1 cm and the metawires were not curved.

6.6. Results

Figure 6.10 shows time domain traces obtained with and without the smooth wire. The spectrum of the wire signal is also shown. It is apparent that for the smooth wire, a single-cycle-like pulse, the partially-evolved Sommerfeld wave, propagates to the detector. To illustrate the lack of free-space contributions to the detected signal, a trace captured with the wire removed is also shown. For the bare wire, a clear polarity inversion could be observed by displacing the wire to either side of the detector optical axis (figure 6.11). Asymmetry in the effect was attributed to a redistribution of the field profile as a result of the bending of the wire, the assumption being that most radiation is lost tangentially at the outer circumference of the bend. The guided signal along the bare wire was peaked at lower frequency and spectrally narrower than the input spectrum (which extended beyond 1.2 THz, see figure 6.10(b)). This behaviour, which is consistent with other experimental studies [28] might be explained by the poorer spatial overlap between the incident terahertz beam (~6 mm diameter) and the higher frequency Sommerfeld wave components which are bound most tightly to the wire and produces an effective low-pass response in the coupling process [29].

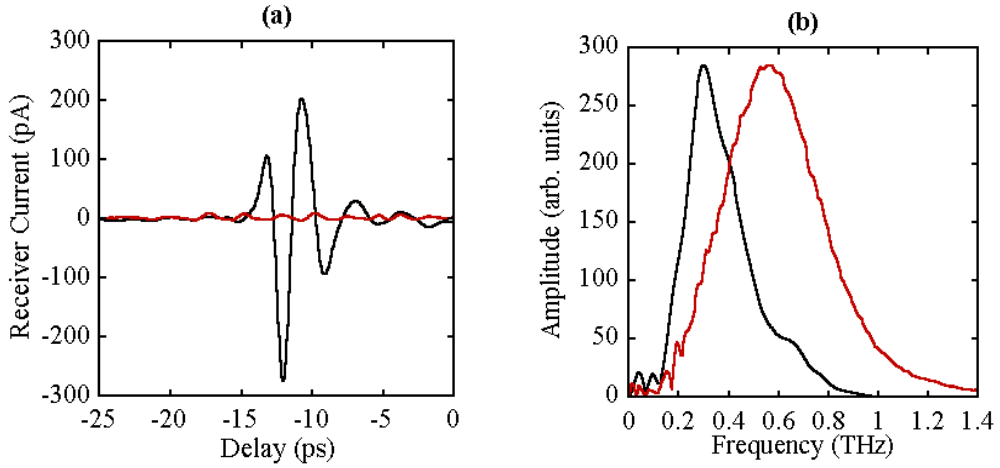

Figure 6.10. (a) Time-domain trace (black) and (b) spectra (black) for propagation along the curved l=15 cm, 600 μm radius copper wire. The time-domain trace with the wire removed is also plotted (red). For comparison, a normalised free-space spectrum (red), obtained with transmitter and receiver face to face at a separation of 15 cm, is shown in (b).

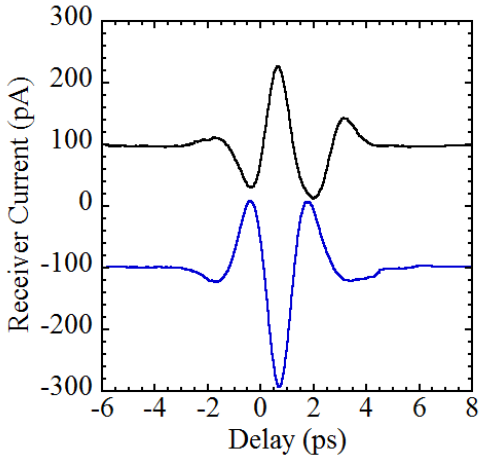

Figure 6.11. Time-domain trace for propagation along the curved l=15 cm, 600 μm radius copper wire with the receiver displaced to either side of the wire axis. Traces were obtained with the radial transmitter with no Ge screen.

Figure 6.12 shows the time-domain trace and spectrum together with the spectrum of a second, nominally identical sample of the helical structure. The similarity between the spectra from the two metawire samples shows the reproducibility of the data to small variations in experimental alignment. In contrast to the bare wire results, propagation on the helical wire is accompanied by significant dispersion, together with beating due to the presence of modes with different frequencies. By comparing the area under the normalised spectra, we can estimate that the spectrally averaged amplitude coupling efficiency is ~3 times higher for the smooth wire, presumably due to better mode matching with the radial source.

We attribute the three spectral peaks at 0.305±0.02 THz, 0.320±0.02 THz and 0.353±0.02 THz to the three lowest order helical metawire modes (figure 6.7). This is in part due to the fact that their relative amplitudes were found to depend upon the orientation of the receiver antenna, indicating some kind of azimuthal mode symmetry, but mainly due to the agreement with calculations described below. Because care was taken to exclude spectral artefacts associated with reflections in the experiment, we tentatively assign the two peaks at 0.249 and 0.273 THz, to either unintentional variations in the pitch of the metawire or, more

likely, to the frequency dependence of the coupling of the guided modes to free space radiation.

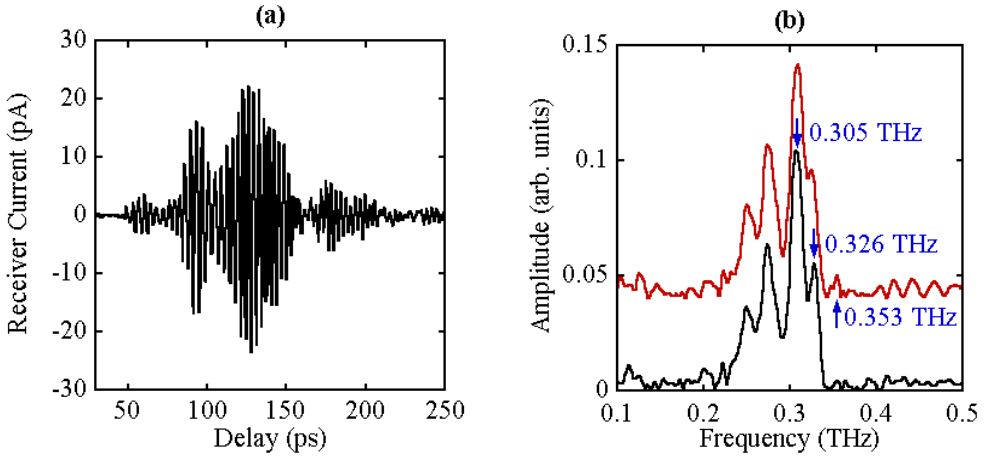

Figure 6.12. (a) Time-domain trace and (b) spectra for SPP propagation along the l=15 cm helical metawire, with SPP peaks marked by blue arrows.

FIT calculations were also performed on a 9.6 cm long structure illuminated in the near field by a linearly polarized plane wave propagating parallel to the wire axis. The band edges from both the FDTD (at 0.305, 0.320 and 0.349 THz) and FIT (0.304, 0.321 and 0.351 THz) simulations were found to be in excellent agreement with the highest frequency peaks found in the experimental amplitude spectra. This allows us to be confident that the experimental peaks do indeed correspond to the helical metawire SPP modes. In the FIT simulations, the simulation time (700 ps) was chosen so that reflection of the electromagnetic fields from the output end of the wire was avoided. The spectra (figure 6.13) clearly recreate the experimental spectra except for the structure in the tails below 0.3 THz. The FIT results also demonstrate that the measured spectrum depends on the azimuthal position of the detector. This point explains the experimentally observed sensitivity to the receiver polarisation mentioned earlier.

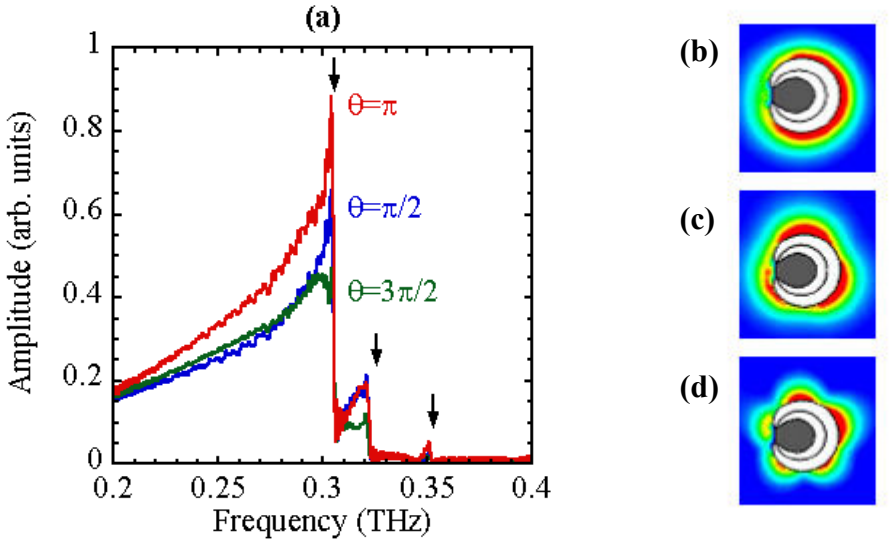

Figure 6.13. (a) FIT simulation results showing the three SPP peaks at three different azimuthal positions (15 μm above the wire surface), θ=π/2, π and 3π/2. Black arrows correspond to experimental peak positions. (b-d) Electric field maps of the three modes evaluated at the band edge ($k_z=\pi/\Lambda$). Red corresponds to high field strengths, descending through yellow and green, to sky blue which indicates low field strengths. The dark blue regions correspond to zero field. (b) m=0. (c) m=1. (d) m=2. [Results are extracted from an FIT simulation carried out by Antonio Fernández-Domínguez].

Figure 6.14 shows time-domain traces and spectra obtained for propagation along the U-ring structure. In contrast with the helical metawire data, it is clear that there is no beating in the time-domain, resulting in what appears to be a single spectral cut-off frequency close to the band edge at ~0.7 THz. In order to analyse the observed propagation characteristics, both FDTD and FIT simulations were undertaken. Although the FDTD calculation predicts the presence of no less than 15 spoof plasmonic modes below the light line with band edges within the range 0.21-0.56 THz (figure 6.15), both experimentally and via FIT simulations only a single band edge is observed close to 0.7 THz (as illustrated in figure 6.14(b)). This result along with the presence of a clear spectral minimum close to the lowest predicted band edge at 0.21 THz (figure 6.14) seems to suggest that the finely spaced SPP bands overlap to form a continuous tail. The spectrally averaged coupling efficiency is ~13% and has a maximum value of ~30% just below the band edge. It is also noted that additional (*m>14*) U-ring modes may

exist in the region up towards the light line and that we simply do not resolve them in our simulation due to the coarse mesh size. Unfortunately, a finer mesh could not be implemented in this work due to the very large simulation volume and long computational times.

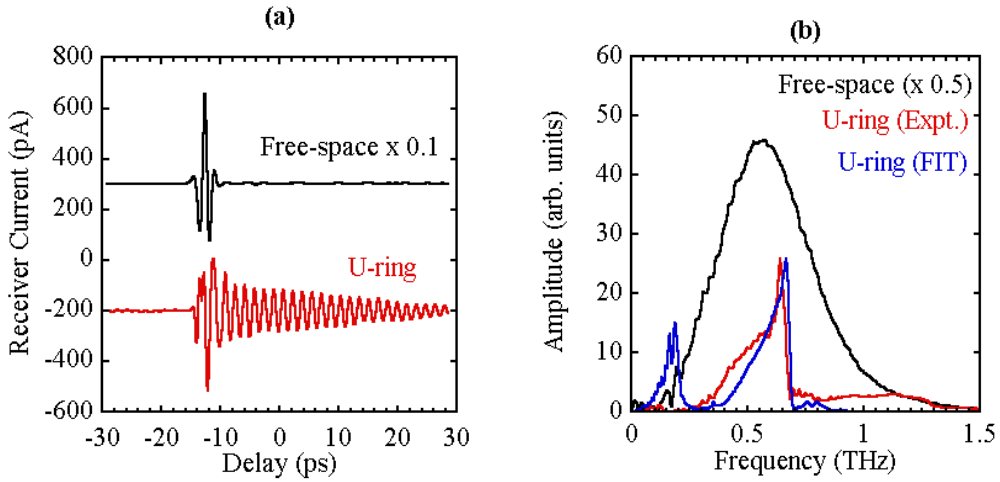

Figure 6.14. (a) Time-domain trace for propagation along the l=15 cm U-ring metawire (red) and in free-space (black). (b) spectra for SPP propagation along the l=15 cm U-ring metawire (red) in free-space (black) and for comparison spectra obtained from an FIT simulation (blue).

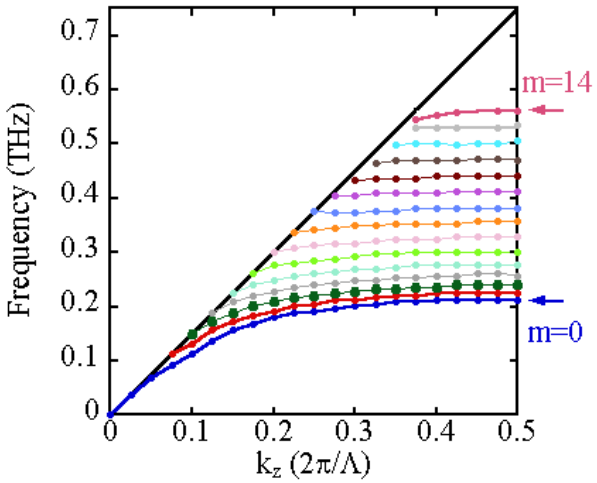

Figure 6.15. Dispersion curves for the full set of SPP modes evaluated on the U-ring metawire with Λ=200 μm, a=100 μm, h=250 μm and R=1250 μm. The light line is also plotted (black line).

The phase difference between the metawire and free-space time-domain signals allows the modal confinement to be estimated using an equivalent expression to equation 4.4 (figure 6.16). The wavevector shift of ~22 m^{-1} close to the spectral peak at 0.6375 THz yields an out-of-plane confinement estimate of ~1.3 mm (~3λ). This value corresponds to an increase in confinement of ~20 compared to a smooth copper wire of equal diameter at the same frequency. Closer to the band edge, the confinement increases to ~850 μm (~2λ) at 0.6712 THz. We anticipate that greater field confinement could be achieved either by decreasing Λ, or switching to a smaller wire diameter. In the latter case this would also reduce the number of modes supported by the structure, leading to spectral narrowing. The main effect of reducing h would be to decrease the number of modes below the light line by increasing the cut-off frequency of the m=0 mode.

The ability to confine radiation to within three free-space wavelengths of the surface over a large propagation distance of 15 cm is encouraging in terms of waveguiding. From FDTD simulations, a radial decay length of ~λ/6 (~96 μm) is predicted for the m=14 mode at the band edge. These highly bound regions of the field are not detected in the experiment due to a combination of larger attenuation, temporal spreading and lower coupling efficiency due to the poorer mode overlap with the transmitter.

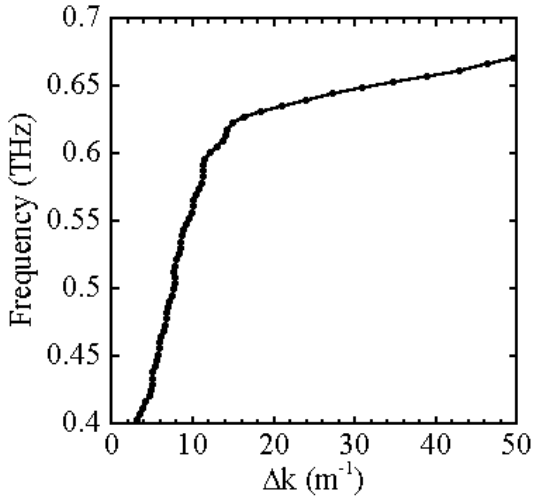

Figure 6.16. Experimental dispersion extracted from phase data for propagation on the U-ring metawire.

6.7. Summary

In summary, we have described the first direct observations of terahertz frequency SPP modes on helical and discretely grooved metawires. With the aid of FDTD and FIT simulations we have been able to numerically model the propagation and identify SPP modes with different azimuthal symmetries. The helical metawire is found to support three azimuthally dependent SPP modes, leading to beating in the time-domain and relatively narrowband guidance. In contrast, the discretely grooved metawire displays broadband character due to the fine frequency-spacing of the supported modes, exhibiting a sharp cut-off close to the band edge. In the latter case, the structure is found to confine radiation to within three free-space wavelengths at the spectral peak, ~20 times smaller than compared to a smooth copper wire of equal diameter. For the U-ring structure it is anticipated that reducing the wire diameter would reduce the number of SPP modes supported by the structure, leading to a reduction in the effective bandwidth but an increase in field confinement. This would also reduce the density of modes within the first Brillouin zone, enabling individual peaks to be resolved as with the case of the helical metawire. The same effect could also be achieved by reducing h so as to increase the cut-off frequency of the m=0 mode. We believe that these structures may find applications in waveguiding and sensing. Particularly in confined geometries, where the metawire design may be more suitable than planar metamaterials.

References

[1] A. Sommerfeld. *Electrodynamics.* Academic Press, New York. Translated from the German by E. G. Ramberg. 177-187 (1964).

[2] K. Wang and D. M. Mittleman. *Metal wires for terahertz wave guiding.* Nature **432**, 376-379 (2004).

[3] T-I. Jeon, J. Zhang and D. Grischkowsky. *THz Sommerfeld wave propagation on a single metal wire.* Appl. Phys. Lett. **86**, 161904 (2005).

[4] K. Wang and D. M. Mittleman. *Guided propagation of terahertz pulses on metal wires.* J. Opt. Soc. Am. B **22**(9), 2001-2008 (2005).

[5] M. Wächter, M. Nagel and H. Kurz. *Frequency-dependent characterization of THz Sommerfeld wave propagation on single-wires.* Opt. Express **13**(26), 10816-10822 (2005).

[6] N. C. J. van der Valk and P. C. M. Planken. *Effect of a dielectric coating on terahertz surface plasmon polaritons on metal wires.* Appl. Phys. Lett. **87**, 071106 (2005).

[7] M. Walther, M. R. Freeman and F. A. Hegmann. *Metal-wire terahertz time-domain spectroscopy.* Appl. Phys. Lett. **87**, 261107 (2005).

[8] G. Goubau. *Surface waves and their application to transmission lines.* J. Appl. Phys. **21**, 1119-1128 (1950).

[9] J. B. Pendry, L. Martín-Moreno and F. J. Garcia-Vidal. *Mimicking surface plasmons with structured surfaces.* Science **305**, 847-848 (2004).

[10] F. J. Garcia-Vidal, L. Martín-Moreno and J. B. Pendry. *Surfaces with holes in them: new plasmonic metamaterials.* J. Opt. A: Pure Appl. Opt. **7**, 97-101 (2005).

[11] W. Rotman. *A study of single-surface corrugated guides.* Proc. IRE **39**(8), 952-956 (1951).

[12] S. A. Maier, S. R. Andrews, L. Martín-Moreno and F. J. García-Vidal. *Terahertz surface plasmon-polariton propagation and focusing on periodically corrugated metal wires.* Phys. Rev. Lett. **97**, 176805 (2006).

[13] A. I. Fernández-Domínguez, L. Martín-Moreno, F. J. García-Vidal, S. R. Andrews and S. A. Maier. *Spoof surface plasmon polariton modes propagating along periodically corrugated wires.* IEEE J. Select. Topics Quant. Electron. **14**(6), 1515-1521 (2008).

[14] J. A. Deibel, M. Escarra, N. Berndsen, K. Wang and D. M. Mittleman. *Finite-element method simulations of guided wave phenomena at terahertz frequencies.* Proc. IEEE **95**(8), 1624-1640 (2007).

[15] Y. B. Ji, E. S. Lee, J. S. Jang and T-I. Jeon. *Enhancement of the detection of THz Sommerfeld wave using a conical metal wire waveguide.* Opt. Express **16**(1), 271-278 (2008).

[16] H. Liang, S. Ruan and M. Zhang. *Terahertz surface wave propagation and focusing on conical metal wires.* Opt. Express **16**(22), 18241-18248 (2008).

[17] L. Shen, X. Chen, Y. Zhong and K. Agarwal. *Effect of absorption on terahertz surface plasmon polaritons propagating along periodically corrugated metal wires.* Phys. Rev. B **77**, 075408 (2008).

[18] P. B. Johnson and R. W Christy. *Optical constants of the noble metals.* Phys. Rev. B **6**(12), 4370-4379 (1972).

[19] M. A. Ordal, R. J. Bell, R. W. Alexander Jr., L. L. Long and M. R. Querry. *Optical properties of fourteen metals in the infrared and far infrared: Al, Co, Cu, Fe, Pb, Mo, Ni, Pd, Pt, Ag, Ti, V and W.* Appl. Opt. **24**(24), 4493-4499 (1985).

[20] M. J. King and J. C. Wiltse. *Surface-wave propagation on coated or uncoated metal wires at millimeter wavelengths.* IRE Trans. Antennas Propag. **10**(3), 246-254 (1962).

[21] K. Wang and D. M. Mittleman. *Dispersion of surface plasmon polaritons on metal wires in the terahertz frequency range.* Phys. Rev. Lett. **96**, 157401 (2006).

[22] P. J. Crepeau and P. R. McIsaac. *Consequences of symmetry in periodic structures.* Proc. IEEE **52**(1), 33-44 (1964).

[23] A. I. Fernández-Domínguez, C. R. Williams, F. J. García-Vidal, L. Martín-Moreno, S. R. Andrews and S. A. Maier. *Terahertz surface plasmon polaritons on a helically grooved wire.* Appl. Phys. Lett. **93**, 141109 (2008).

[24] R. A. Waldron. *A helical coordinate system and its applications in electromagnetic theory.* Quant. J. Mech. Appl. Math. **11**(4), 438-461 (1958).

[25] J. A. Deibel, K. Wang, M. D. Escarra and D. M. Mittleman. *Enhanced coupling of terahertz radiation to cylindrical wire waveguides.* Opt. Express **14**(1), 279-290 (2006).

[26] H. Cao and A. Nahata. *Coupling of terahertz pulses onto a single metal wire waveguide using milled grooves.* Opt. Express **13**(18), 7028-7034 (2005).

[27] A. Agrawal and A. Nahata. *Coupling terahertz radiation onto a metal wire using a subwavelength coaxial aperture.* Opt. Express **15**(14), 9022-9028 (2007).

[28] J. A. Deibel, N. Berndsen, K. Wang, D. M. Mittleman, N. C. J. van der Valk and P. C. M. Planken. *Frequency-dependent radiation patterns emitted by THz plasmons on finite length cylindrical metal wires.* Opt. Express **14**(9), 8772-8778 (2006).

[29] K. Wang, D. M. Mittleman, N. C. J. van der Valk and P. C. M. Planken. *Antenna effects in terahertz apertureless near-field optical microscopy.* Appl. Phys. Lett. **85**, 2715-2717 (2004).

7. Conclusions

In this thesis, a fibre-coupled terahertz time-domain spectroscopy (TTDS) system using hollow-core photonic crystal fibres (HC-PCFs) and photoconducting dipoles was constructed and used to investigate terahertz surface plasmon polariton (SPP) guidance on a range of metamaterial structures. In each case, high confinement waveguiding was achieved by binding SPPs to cavity resonances which spoof the behaviour of intrinsic surface plasmon resonances found at much higher frequencies.

In chapter 3, the construction of the fibre-coupled TTDS system was described. The dynamic range (~$2x10^5$) and bandwidth (up to ~2.2 THz) of our system were found to compare favourably both to the commercial system distributed by Picometrix and other fibre-based systems described to date in the literature. By using HC-PCFs, the optical power available for terahertz generation and detection was significantly increased. In addition to this, by working above the zero dispersion wavelength, the fibre itself can be used to provide negative group velocity dispersion (GVD) and compensate for positive GVD imparted by other optical components in the system. This removes the requirement for external dispersion compensation, making the system more compact and less prone to drift. The extension of the system to include a near-field probing arm for mapping of evanescent fields was also described. In this case, the sub-wavelength spatial resolution of the probe was found to correspond closely to the sum of the effective receiver length and probe-sample separation.

In chapter 4, wavelength-scale confinement of radiation over an octave in frequency was demonstrated on plasmonic metamaterials consisting of copper sheets patterned with two-dimensional arrays of square copper-lined holes. This degree of confinement represents more than a two orders of magnitude increase compared to a flat copper sheet over the same frequency range. For this structure, radiation is bound as a result of diffraction induced bending of the TE_{10} SPP dispersion curve close to the zone boundary. This was confirmed by

measurements on random structures, where the removal of periodicity was found to lead to much poorer field confinement. From simulations, the amplitude attenuation coefficient for these structures was estimated to be 0.11 cm^{-1}, reflecting a tolerable trade-off between loss and confinement. These characteristics are encouraging for potential applications in terahertz waveguiding, as well as in chemical or biochemical sensing.

In chapter 5, dual-band wavelength-scale confinement of radiation was demonstrated using a novel coaxial hole array structure. In this case, in addition to the diffracted TE_{11} mode, the addition of a coaxial pillar introduces a TEM-like mode which is bound to the central pillar and displays a cut-off dependent on the cavity depth. Therefore, for deep enough cavities the TEM-like cut-off represents an effective spoof plasma frequency, which even for air-filled cavities can be engineered to lie within the first Brillouin zone. Such an effect is not possible for bare cavities as high-index dielectrics are required to reduce the TE_{11} spoof plasma frequency below the band edge. The amplitude attenuation on the coaxial structure was measured experimentally using a cut-back method and found to be 0.22 ± 0.06 cm^{-1}, in excellent agreement with simulations which predict losses of 0.20 cm^{-1}. For our structure, simulations suggest that close to the TEM-like cut-off, fields are bound to within $\sim\lambda/9$ of the sample surface. This produces a five-fold field enhancement with respect to the field confinement at the TE_{11} band edge. The dual-frequency confinement of radiation on these samples could be used for quantitative sensing of thin dielectrics, biochemicals and crystalline solids. In the latter case, we anticipate that by matching one or more of the metamaterial resonances to the resonant phonon peaks of the sample it may be possible to achieve a combined resonant enhancement in sensitivity.

Finally, in chapter 6, the first direct observations of terahertz SPPs on helical and discretely grooved cylindrical metamaterials termed metawires were presented. In this case, with the aid of numerical simulations the structures were shown to support multiple azimuthally dependent modes with distinct mode symmetries. In each case, the number of modes below the light-line was shown to be controlled by the cavity depth and metawire diameter. For the discretely grooved metawire, wavelength-scale field confinement was demonstrated close to the band edge,

representing at least a twenty-fold increase in confinement compared to a smooth copper wire of equal diameter at the same frequency. Such structures may prove to be particularly useful for waveguiding and sensing in confined geometries, where the metawire design may be more suitable than planar metamaterials.